Proceedings of the 4th BSME-ASME International Conference on Thermal Engineering
27 -29 December 2008, Dhaka, Bangladesh

WAKE AND SEPARATION CHARACTERISTICS OF A CIRCULAR ARC BLADE WITH BUMP IN TRANSONIC FLOW FIELD

A.B.M. Toufique Hasan[1], Shigeru Matsuo[2], Md. Mamun[3], Toshiaki Setoguchi[2] and Heuy Dong Kim[4]

[1] Graduate School of Science and Engineering, Saga University, 1 Honjo, Saga 840-8502, Japan
[2]Department of Mechanical Engineering, Saga University, 1 Honjo, Saga 840-8502, Japan
[3] Department of Mechanical Engineering, BUET, Dhaka 1000, Bangladesh
(Email: mdmamun@me.buet.ac.bd)
[4] School of Mechanical Engineering, Andong National University, Andong 760-749, Korea

ABSTRACT

In recent years, the effect of bump wall on transonic flow field around an airfoil has been investigated experimentally and as a result, it was shown that the bump wall is effective for the control of shock wave on the airfoil. In the present study, the flow characteristics downstream of a circular arc blade with a bump were investigated numerically. Results showed that the vortex strength, separated flow and wake static pressure fluctuations were reduced in case of blade with bump compared to no bump case.

Key words: *transonic flow, bump, wake, separated flow*

1. INTRODUCTION

Shock and boundary layer control in transonic flow is considered to have a large potential for improving aerodynamic performances in turbomachinery. Thus this control has received great attention in the last decades and still represents a topic of high interest. Flow field unsteadiness, flow separation, buffet, adverse aerodynamic loading are some examples of shock boundary layer interaction. These unsteady phenomena are observed in the internal aeronautical applications such as butterfly valve, fan, diffuser, compressor blades and so on. Many active, passive as well as hybrid control techniques are proposed to reduce the undesirable impacts of shock boundary layer interaction [1-2]. Among them, recently bump wall near the shock position is investigated experimentally and numerically for its quite simple technology as well as significant drag reduction [3-5]. However phenomena downstream of the bump have not attracted the attention of earlier researches.

In the present study, the flow characteristics around a circular arc blade with bump such as vortex generation, wake static pressure fluctuation and separated flow behavior were investigated numerically.

2. NUMERICAL METHOD

The governing equations used are the unsteady compressible Navier-Stokes equations coupled with turbulence kinetic energy and eddy viscosity equations in a two-dimensional coordinate system. The turbulence model used in this simulation is a modified *k-R* model [6-7], which is a two-equation model applicable to both wall bounded and free shear flows. A third-order TVD (Total Variation Diminishing) finite difference scheme with MUSCL [8] is

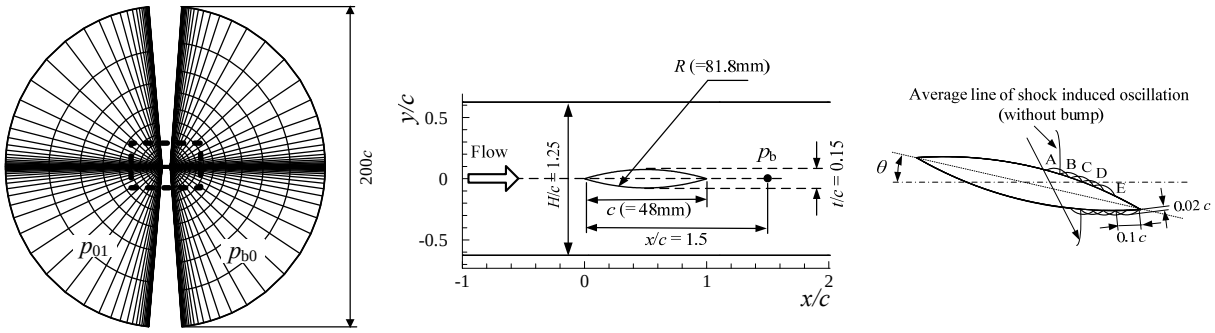

(a) Computational domain (b) Details of test section (c) Bump model on blade

Fig. 1 Computational grids and details of bump model

used to discretize the spatial derivatives and a second order-central difference scheme for the viscous terms, and a second-order fractional step method is employed for time integration.

3. COMPUTATIONAL CONDITIONS

Figures 1(a) and 1(b) show computational domain of the flow field and details of a test section, respectively. The chord length c and thickness of the blade are 48mm and 7.2mm, respectively. The radius of circular arc R is 81.8mm.The number of grids is 351×101. Figure 1(c) shows a circular arc blade with bump. Bump length and thickness are 0.1c and 0.02c, respectively. To find out an effective bump location, a bump is located at several distances from the mean line of shock induced oscillation (without bump). When the crest of the bump coincides with the line of average shock induced oscillation, then the bump was considered as Model A. Models B, C, D and E are 0.05c, 0.10c, 0.15c and 0.20c apart from the shock position. The inlet Mach number upstream of the blade is 0.6 and Reynolds number is 5.4×10^5. The pressure ratio p_{b0}/p_{01} was kept at 0.739. The non slip-wall, ambient and downstream conditions were used as boundary conditions. Also, iso-pressure and no-heat transfer were imposed on the solid wall.

4. RESULTS AND DISCUSSION

Dominant frequencies of shock oscillations measured at x/c = 0.833 on blade upper surface (without bump) obtained from experiments and computations are shown in Table 1 for blade angles of attack, θ = 0° and 3.2°. As seen from the table, the frequencies of the present computations are in good agreement with those of experiments.

Several computations were performed to find out an effective bump position on the blade surface from the view point of reduction of shock strength ($\Delta p/p_1$) and range of oscillation. p_1 is the pressure upstream of the shock. Computed results are presented in Table 2. As seen from this table, the shock strength and range of oscillation are reduced significantly for the case of blade with bump of Model D for all angles of attack (θ = 0°, 3.2°, 8.5°).

Figures 2 (a) and 2(b) show contour maps of Mach number around a circular arc blade without bump during the cycle of flow oscillation for θ = 0° and p_{b0}/p_{01} = 0.739. $T_{S\text{-}nb}$ is the

Table 1 Dominant frequency of shock oscillating (kHz) at x/c = 0.83 on blade upper surface (p_b/p_{01}= 0.650, p_{b0}/p_{01}= 0.739)

	Angle of attack, θ	
	0°	3.2°
Experiment	1.190	1.260
Computation	1.186	1.252

Table 2 Shock strength and oscillating range (p_b/p_{01}= 0.650, p_{b0}/p_{01}= 0.739)

Angle of attack, θ		0°		3.2°		8.5°	
Parameters / Blade		$\Delta p/p_1$	$\Delta x/c$	$\Delta p/p_1$	$\Delta x/c$	$\Delta p/p_1$	$\Delta x/c$
Without bump		1.21	0.90	1.47	0.84	1.99	0.93
With bump	Model A	1.11	0.79	1.47	0.81	1.84	0.86
	Model B	0.99	0.75	1.16	0.78	1.65	0.83
	Model C	0.93	0.47	1.07	0.63	1.60	0.78
	Model D	0.85	0.40	0.82	0.51	1.05	0.63
	Model E	1.05	0.63	1.11	0.70	--	--

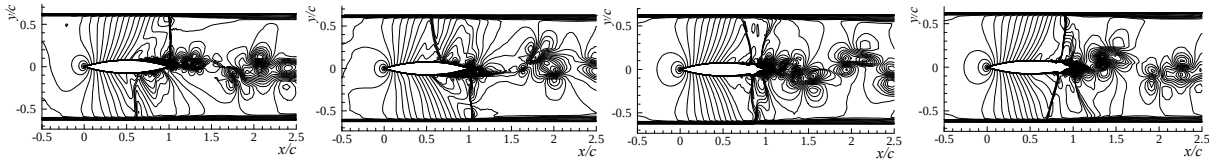

(a) t = 0.0 $T_{S\text{-}nb}$ (b) t = 0.50 $T_{S\text{-}nb}$ (c) t = 0.0 $T_{S\text{-}wb}$ (d) t = 0.50 $T_{S\text{-}wb}$

Fig. 2 Contour maps of Mach number around blade without bump (a,b) and around blade of Model D (c,d) (θ = 0°, p_b/p_{01} = 0.650, p_{b0}/p_{01} = 0.739)

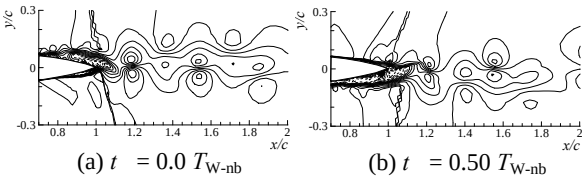

(a) t = 0.0 $T_{W\text{-}nb}$ (b) t = 0.50 $T_{W\text{-}nb}$

Fig. 3 Contour maps of u-velocity component for blade without bump (θ = 0°, p_{b0}/p_{01} = 0.739)

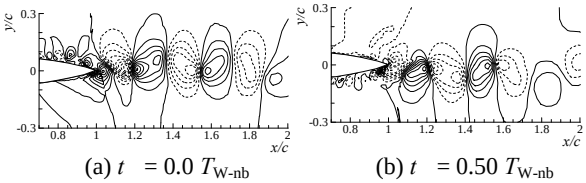

(a) t = 0.0 $T_{W\text{-}nb}$ (b) t = 0.50 $T_{W\text{-}nb}$

Fig. 4 Contour maps of v-velocity component for blade without bump (θ = 0°, p_{b0}/p_{01} = 0.739)

time period of shock oscillation for the case of blade with no bump. These cases correspond to the flow field with shock oscillation in opposite direction each other at the upper and lower passages. Figures 2(c) and 2(d) show contour maps of Mach number around a circular arc blade with bump of Model D corresponding to the previous flow conditions. $T_{S\text{-}wb}$ is the time period of shock oscillation for the case of blade with bump. As seen from Figs. 2(c) and 2(d), the average position of shock oscillation is located close to the leading edge of the bump and the strength of shock wave became weak compared to those of no bump model (Figs. 2(a) and 2(b)).

Figure 3 shows contour maps of u-velocity component downstream of blade without bump during the period of wake oscillation for θ = 0° and p_{b0}/p_{01} = 0.739. $T_{W\text{-}nb}$ is the time period of wake oscillation for blade with no bump. Dashed lines corresponds to negative (-ve) values. The u-velocity component shows an anti-symmetric periodic structure which alternates from upper and lower surface of the blade.

Figure 4 shows contour maps of v-velocity component downstream of blade without bump corresponding to the flow conditions of Fig. 3. As seen from these figures, the cores of positive and negative values develop alternatively downstream of the blade.

Figure 5 shows temporal sequence of the periodic characteristics of vortex downstream of the blade without bump corresponding to the previous flow conditions. IVC is the initial vortex core in the wake. This is the vortex that has minimum static pressure and density with maximum vorticity magnitude at the center of the core compared to those of other cores downstream of IVC. This shows that the separated shear layer generates alternatively from upper and lower blade surfaces. Circulation in the separated shear layer supply energy to develop the vortex. This process continues until the vortex is cut off from the shear layer and

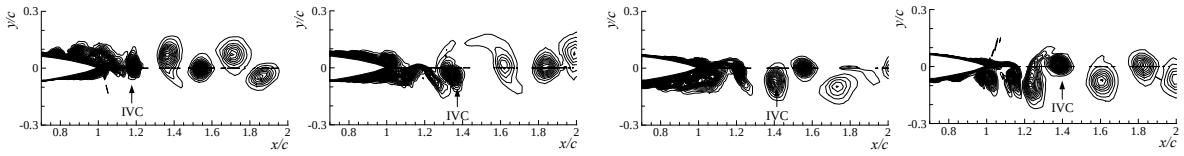

(a) t = 0.0 $T_{W\text{-}nb}$ (b) t = 0.25 $T_{W\text{-}nb}$ (c) t = 0.50 $T_{W\text{-}nb}$ (d) t = 0.75 $T_{W\text{-}nb}$

Fig. 5 Contour maps of vorticity around blade without bump (θ = 0°, p_{b0}/p_{01} = 0.739)

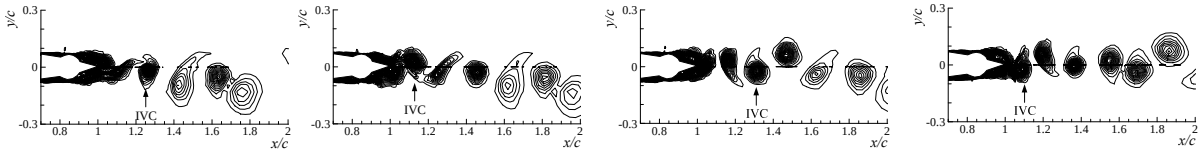

(a) t = 0.0 $T_{W\text{-}wb}$ (b) t = 0.25 $T_{W\text{-}wb}$ (c) t = 0.50 $T_{W\text{-}wb}$ (d) t = 0.75 $T_{W\text{-}wb}$

Fig. 6 Contour maps of vorticity around blade of Model D (θ = 0°, p_{b0}/p_{01} = 0.739)

thus establishes the IVC. IVC appeared at x/c = 1.18, 1.38, 1.42 and 1.40 for t = 0.0$T_{W\text{-}nb}$, 0.25$T_{W\text{-}nb}$, 0.50$T_{W\text{-}nb}$ and 0.75$T_{W\text{-}nb}$, respectively. The blending of two velocity components (Figs. 3 and 4) gives rise to the periodic flow through a series of vortices.

Figure 6 shows contour maps of vorticity around the blade with bump of Model D during the period of wake oscillation (θ = 0°, p_{b0}/p_{01} = 0.739). $T_{W\text{-}wb}$ is the time period of wake oscillation for blade with bump of Model D. In this case, the separated shear layer develops simultaneously from upper and lower blade surfaces and their combined effect generates the initial vortex core (IVC) earlier compared to those of no bump model (Fig.5). IVC appeared at x/c = 1.22, 1.15, 1.30 and 1.10 for t = 0.0$T_{W\text{-}wb}$, 0.25$T_{W\text{-}wb}$, 0.50$T_{W\text{-}wb}$ and 0.75$T_{W\text{-}wb}$, respectively. Thus the vortex starts to shed closer to the trailing edge compared to that of blade with no bump case.

Figure 7 shows distributions of static pressure p/p_{01}, density ρ/ρ_{01} and vorticity ω through the initial vortex core (IVC) in the wake downstream of the blade without bump. It is seen from the figures that at the center of the vortex, there is a sudden decrease of pressure and density followed by a sudden rise in vorticity. Also, movements of vortex centers are observed along the wake centerline during the time period.

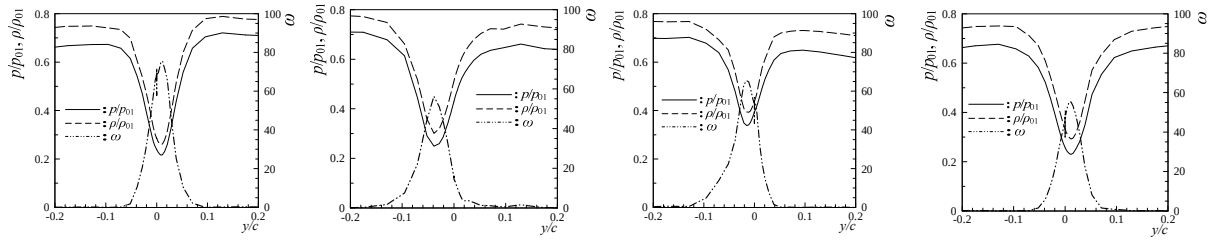

(a) t = 0.0 $T_{W\text{-}nb}$ (b) t = 0.25 $T_{W\text{-}nb}$ (c) t = 0.50 $T_{W\text{-}nb}$ (d) t = 0.75 $T_{W\text{-}nb}$

Fig. 7 Distributions of static pressure, density and vorticity through initial vortex core (IVC) in the wake downstream of the blade without bump (θ = 0°, p_{b0}/p_{01} = 0.739)

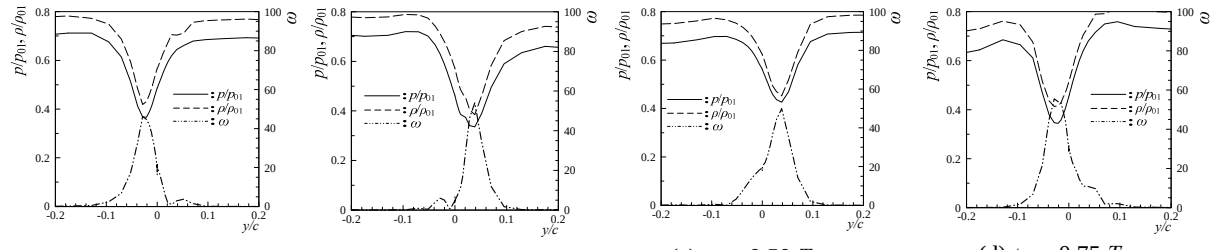

(a) t = 0.0 $T_{W\text{-}wb}$ (b) t = 0.25 $T_{W\text{-}wb}$ (c) t = 0.50 $T_{W\text{-}wb}$ (d) t = 0.75 $T_{W\text{-}wb}$

Fig. 8 Distributions of static pressure, density and vorticity through initial vortex core (IVC) in the wake downstream of the blade of Model D (θ = 0°, p_{b0}/p_{01} = 0.739)

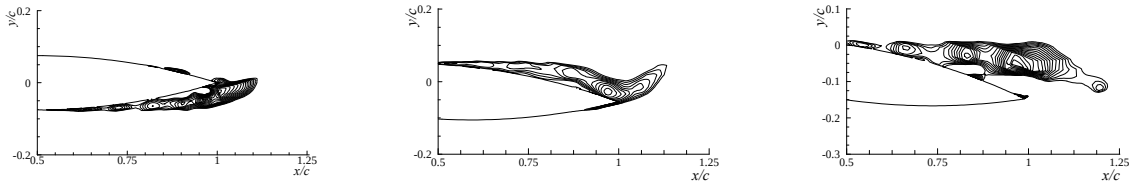

(a) $\theta = 0°$ (b) $\theta = 3.2°$ (c) $\theta = 8.5°$

Fig. 9 Contour maps of $-u$ velocity around blade without bump (p_{b0}/p_{01} = 0.739)

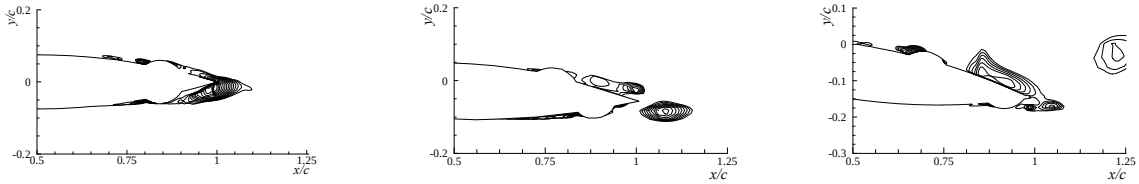

(a) $\theta = 0°$ (b) $\theta = 3.2°$ (c) $\theta = 8.5°$

Fig. 10 Contour maps of $-u$ velocity around blade of Model D (p_{b0}/p_{01} = 0.739)

Distributions of static pressure p/p_{01}, density ρ/ρ_{01} and vorticity ω through the initial vortex core (IVC) in the wake downstream of the blade with bump of Model D are shown in Figure 8. The reduction of pressure and density and rise in vorticity at the vortex center are smaller compared to those in Fig. 7 (no bump). These signify a reduction of vortex strength in case of blade with bump of Model D.

Figure 9 shows contour maps of $-u$ velocity around blade for different blade angles of attack (θ = 0°, 3.2°, 8.5°) at the same time instant. Reverse flow region is increased and it starts from upstream for blade with angle of attack. A significant reduction in reverse flow region is observed by the presence of bump over the blade surfaces as shown in Fig.10.

Figure 11 shows effect of bump on separation point over blade upper and lower surfaces during one period of shock oscillation, T_S for different angles of attack (θ = 0°, 3.2°, 8.5°). For θ = 0°, separation point oscillates alternatively in between upper and lower surface and it ranges from x/c = 0.5~0.95 for blade without bump. But bump of Model D suppresses this oscillation and the separation is starts nearly from x/c = 0.8. For θ = 3.2° and 8.5°, separation points are seen upstream for blade upper surface compared to those of lower surface. Also, for these angles of attack, significant reductions in separation point oscillation as well as the downstream shift of separation points are observed for blade with bump of Model D.

Figure 12 shows time histories of wake static pressure for blade without and with bump model and corresponding power spectrum densities (x/c = 1.5, θ = 0°, p_{b0}/p_{01} = 0.739). Amplitude of pressure fluctuations and peaks of power spectrum density are reduced and frequency is increased in case of blade of Model D to that of no bump model. Similar results were found for θ = 3.2° and 8.5°.

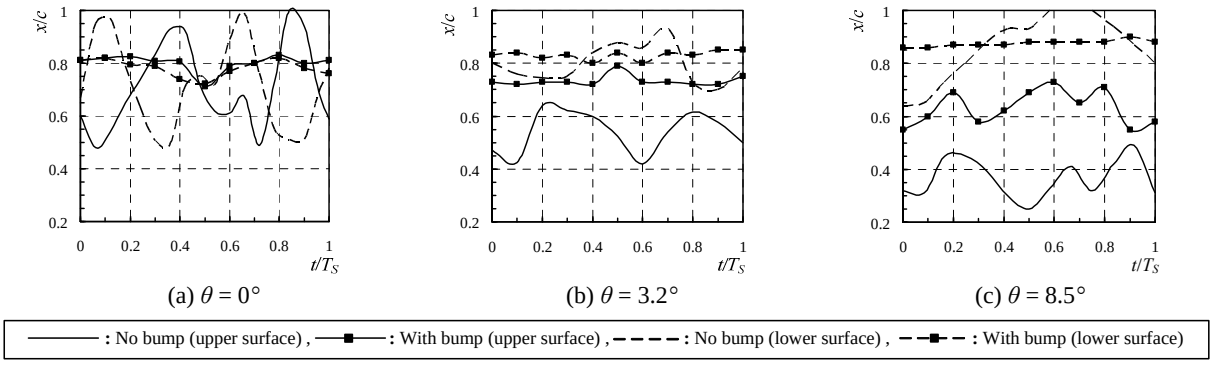

(a) $\theta = 0°$ (b) $\theta = 3.2°$ (c) $\theta = 8.5°$

Fig. 11 Effect of bump on separation points over blade surfaces (p_{b0}/p_{01} = 0.739)

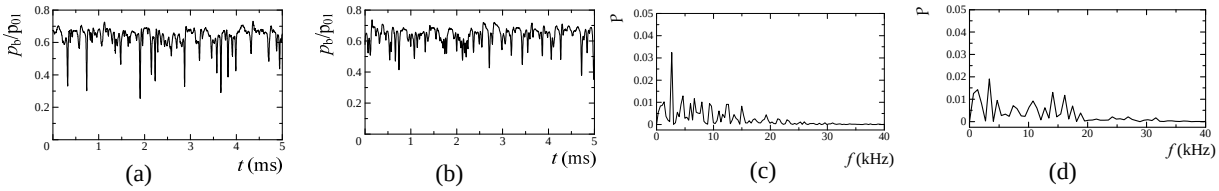

Fig. 12 Wake static pressure time histories for blade without bump(a) and for Model D (b) and corresponding power spectrum densities (c,d) (x/c = 1.5, θ = 0°, p_{b0}/p_{01} = 0.739)

5. CONCLUSIONS

Wake and separation characteristics of a circular arc blade with bump in transonic flow field for three angles of attack was investigated numerically. Results obtained are as follows: vortex starts to shed earlier and vortex strength is reduced in case of blade of Model D to that of blade without bump. This is considered due to the reduction of reverse flow region is presence of a bump. The separation point shifts to the downstream when there is a bump on the blade surface for all angles of attack. Moreover, amplitude of wake pressure fluctuations and peaks of power spectrum density are reduced for blade of Model D compared to those of no bump model.

REFERENCES

[1] Stanewsky, E., Délery, J., Fulker, J., de Matteis, P. (Eds), Drag reduction by shock and boundary layer control: results of the project EUROSHOCK II*, In Notes on Numerical Fluid Mechanics and Multidisciplinary Design*, vol. 80, 2002 (Springer).

[2] Qin, N., Zhu, Y., Ashill, P., Active control of transonic aerodynamics using suction, blowing, bumps and synthetic jets, *Proc. AIAA 18th Applied Aerodynamics Conference, AIAA Paper* 2000-4329, 2000.

[3] Tulita, C., Rangunathan, S., Benard, E., Control of transonic periodic flow on NACA0012 aerofoil by contour bumps, *Proc. IUTAM Symposium Transsonicum IV*, pp.291-296, Göttingen, Germany, September 2002.

[4] Qin, N., Zhu, Y., Shaw, S.T., Numerical study of active shock control for transonic aerodynamics, *Int. J. Numerical Methods for Heat and Fluid Flow*, vol. 14, No.4, pp. 444-466, 2004.

[5] Milholen, W.E., Owens, L.R., On the application of contour bumps for transonic drag reduction, *AIAA paper*-2005-0462, 2005.

[6] Goldberg, U. C., Toward a pointwise turbulence model for wall-bounded and free shear flows, *Trans ASME, J Fluids Eng*, vol.116, pp. 72-76, 1994.

[7] Heiler, M., Instationäre Phänomene in Homogen/Heterogen Kondensierenden Düsen- und Turbinenströmungen, *Dissertation, Fakultät für Maschinenbau,* Universität Karlsruhe (TH), Germany, 1999.

[8] Yee, H. C., A class of high-resolution explicit and implicit shock capturing methods, *NASA TM-89464*, 1989.

Proceedings of the 4th BSME-ASME International Conference on Thermal Engineering
27-29 December, 2008, Dhaka, Bangladesh

OPTIMIZATION OF FLOW SEPARATION OF AN AIRFOIL USING BUMPY SURFACE

Mohammad Mashud, Md. Nizam Uddin, D. M. Asaduzzaman and Akira Umemura*
Department of Mechanical Engineering
Khulna University of Engineering & Technology (KUET)
Khulna-9203, Bangladesh.
*Department of Aerospace Engineering, Nagoya University, Japan.
(E-mail: mdmashud@yahoo.com)

ABSTRACT

This paper presents an investigation on the effect of introducing large-scale roughness through static curvature modifications on the low speed flow over an airfoil. The surfaces of a standard NACA 4415 airfoil have been modified with regular perturbations or "bumps" of the order of 2%c for this purpose. While the actual NACA 4415 airfoil is not a suitable candidate for low Re cases due to extensive prevalence of boundary layer separation, it is expected that the bumps would exercise passive flow control by promoting early transition to turbulence, thereby reducing the extent of separation and improving the performance. From this investigation it has been found that the separation bubbles begin on the upper surface of the bumpy surface model is later than the regular surface model. This implies that the stall appears of bumpy surface model at higher attack angle than the regular surface model. The lift to drag ratio also increases for bumpy surface airfoil and consequently improve the performance of the wing. Experiments are conducted for chord based Re values ranging from 25,000 to 500,000.

Keywords*: Airfoil, Bumpy Surface, Flow Control, Surface Roughness.*

1. INTRODUCTION

The aerodynamic characteristics of low Reynolds number airfoils are fundamentally different from those seen in typical aerospace applications. Subsonic aerodynamics, not a major area of study until the recent past, promises tremendous potential in the development of small, robust and high performance aircraft: Unmanned Aerial Vehicles (UAVs), Remotely Piloted Vehicles (RPVs) and Micro Aerial Vehicles (MAVs). These are particularly useful for defense applications such as surveillance, communication links, ship decoys and detection of biological, chemical or nuclear materials. Another important application of these vehicles has been identified in space or planetary exploration, especially in extreme low density environments such as in Mars. These vehicles present extreme constraints to the airfoil design process in the form of (a) extreme operating conditions (cruise velocity, altitude, density); and (b) very small aspect ratios. The mission profiles tend to incorporate entirely different regimes in terms of their speed, altitude and maneuvering requirements. For example, RPVs need to be operative at both normal and very high altitudes (where the density of air is low). From a fluid dynamist's point of view, the performance of an aircraft is essentially controlled by the development of the boundary layer on its surface and its interaction with the mean flow. This interaction decides the pressure distribution on the airfoil surface and subsequently the aerodynamic loads on the wing. In order to obtain the highest levels of performance efficiencies for mission varying aircraft, it is necessary to either: (a) alter the boundary layer behavior over the airfoil surface—flow control methods of interest here, and/or (b) change the geometry of the airfoil real time for changing free stream conditions—adaptive wing technology. The value of aerodynamic efficiency needs to be maximum i.e. the lift to the drag ratio needs to be maximized. For this case lift should be high and drag should be low. This paper discusses the experimental results of flow control method by changing the airfoil surface geometry to improve the performance of the airfoil as well as aircraft.

2. MODEL CONSTRUCTION

If we desire to examine the aerodynamic characteristics of a large model, a large scale wind tunnel facility is necessary for testing. A small sized model has been selected to examine the aerodynamic characteristics for the experiments due to the limitation of wind tunnel size. The scale downed on the basis of Reynolds number. The thickness and chord length of the model are 38.1 mm and 254 mm, respectively. The span length of the model relative to the chord length is one of the important design parameters. Obviously, it should be made as large as possible so that the weight of the model can be reduced. In the Present experiment the span length was chosen to be 150 mm, a considerably large value, so as to minimize the end effect of the model. To perform the experiments there are two types of model has been constructed (as shown in Fig.1): (i) Bumpy Surface Model and (ii) Regular Surface Model. Both of the models are made using NACA 4415 profile.

(a) Regular Surface (b) Bumpy Surface

Fig.1 Models to be tested

It is considered that bumpy height is variable but the arc length is constant. So, if the height reduced then the length or radius of the segments of the circular perimeter on the surface increased. The arc length should select carefully so that the surface had enough bump or wave. The chord length of the model is 254 mm. The NACA 4415 has a design R_{ec} value of around 2 million, tailored to application in HPVs (Human Powered Vehicles). The baffles inside the wing gave rise to a modified NACA 4415 profile with regular surface perturbations (Fig. 1(b)). The radius of the bumps was of the order of 2%c. While covering the airfoil with a membrane (to mimic the smooth profile) and adding a trailing edge extension were considered, it was decided to leave the airfoil unskinned to keep the flow tripped at all times along the surface. Maximum height, denoted by *h*, of the bumpy surface is 5.02 mm. This is the 3rd bump or wave. The 2nd and 5th bumps are height of 0.9*h* mm and 1st and 6th bumps are height of 0.6*h* mm. Both sides of the model are bumpy. To measure the external surface pressure, pressure probes are out-fitted at the centerline of the span on the surface of the wing.

3. EEXPERIMENTAL SET-UP

The experiments were conducted using 310×300 mm wind tunnel in Fluid dynamics laboratory, Department of Mechanical Engineering, Khulna University of Engineering and Technology, Bangladesh. Fig.2 shows a schematic of the experimental set up. The model was placed in the middle of the test section supported by 5mm diameter iron rod and flat plate threaded through two circular holes of the test section side walls so that it could freely rotated about the flat plate. The orientation of the model (attack angle) was adjusted by pulling two ropes suspending the leading and trailing edge of the model. The surface of the model is drilled through 1.5 mm diameter holes and small sizes pressure tubes are placed inside the drilled holes. The pressure tubes are connected to the digital manometer by vinyl tubes of equal length. There is an angle measuring instruments attached with the flat plate to measure the angle of attack.

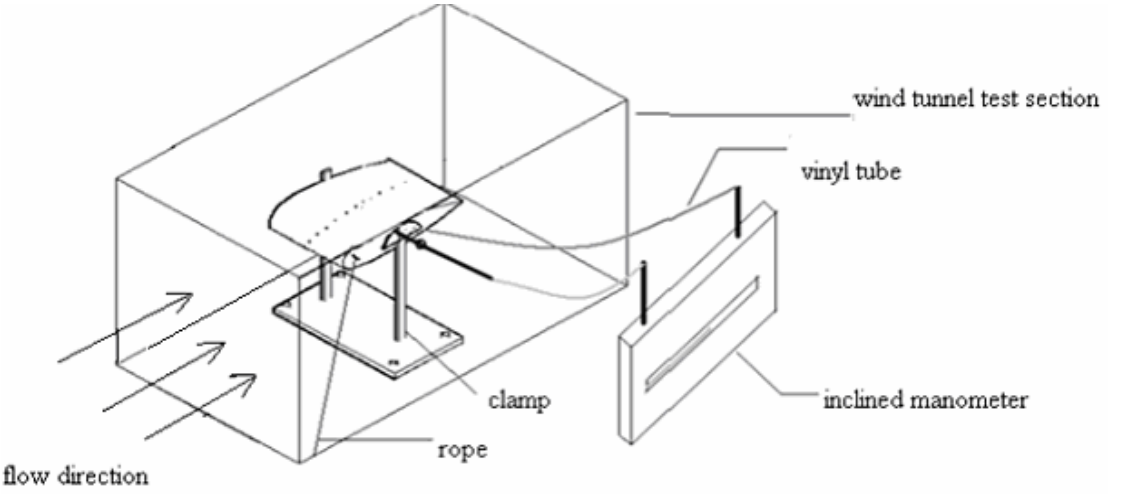

Fig. 2 Schematic diagram of experimental setup

4. RESULTS AND DISCUSSION

4.1. External Surface Pressure distributions

All measurements are conducted during the steady-state conditions. As shown in Fig. 3, the upper and lower surface pressure distributions are presented as a plot of upper surface pressure coefficient C_{pU} and lower surface pressure coefficient C_{pL} fraction of local chord projected to the plane of the leading edge and total chord length (dimensionless distance *x/C*). According to Fig. 3, it is found that the separation bubbles begin at an attack angle 8^0 at a distance *0.9c* from the leading edge towards trailing edge for regular surface model. On the other hand, bumpy surface model's separation bubbles begin at an attack angle 10^0. The length of separation region increases with increasing the attack angle. It has been shown from the experiment that the model using bumpy surface flow separation appears at large attack angle. Flow separation occurs due to boundary layer thickness. The boundary layer thickness is considerably affected by the pressure gradient in the direction of flow. When the pressure gradient imposed on the flow is not too adverse, transition and reattachment may occur after laminar separation, and the resultant turbulent boundary layer is found to be more resistant to flow separation. This provides a reasonable justification for separation control by means of promoting early transition in laminar flows, thereby reducing the otherwise imminent form drag. Experimental observations show that "rough" airfoils perform better than the "smooth" surface airfoils at low *Re* values, as shown in Fig. 3. If the pressure gradient is zero, then the boundary layer continues to grow in thickness. With decreasing the pressure in the direction of flow i.e.; with negative pressure gradient, the boundary layer tends to be reduced in thickness. However, with the pressure increasing in the direction of flow; with positive (adverse) pressure gradient the boundary layer thickens rapidly. The adverse pressure gradient plus the boundary shear decreases the momentum in the boundary layer and if they both act over a sufficient distance they cause the fluid in the boundary layer to come to rest i.e.; the retarded fluid particles cannot, in general penetrate too far into the region of increased pressure owing to their small kinetic energy. Thus, the boundary layer is deflected sideways from the boundary, separates from it and moves into the main stream. In the bumpy surface the flow passed through a wave, the pressure gradient is negative, at highest elevation it becomes zero, and then it becomes positive. During this time the adverse pressure gradient tends to separates from the surface. The flow gets another wave and the flow is attached. In this way the separation is controlled, i.e.; the separation occur at large attack angle.

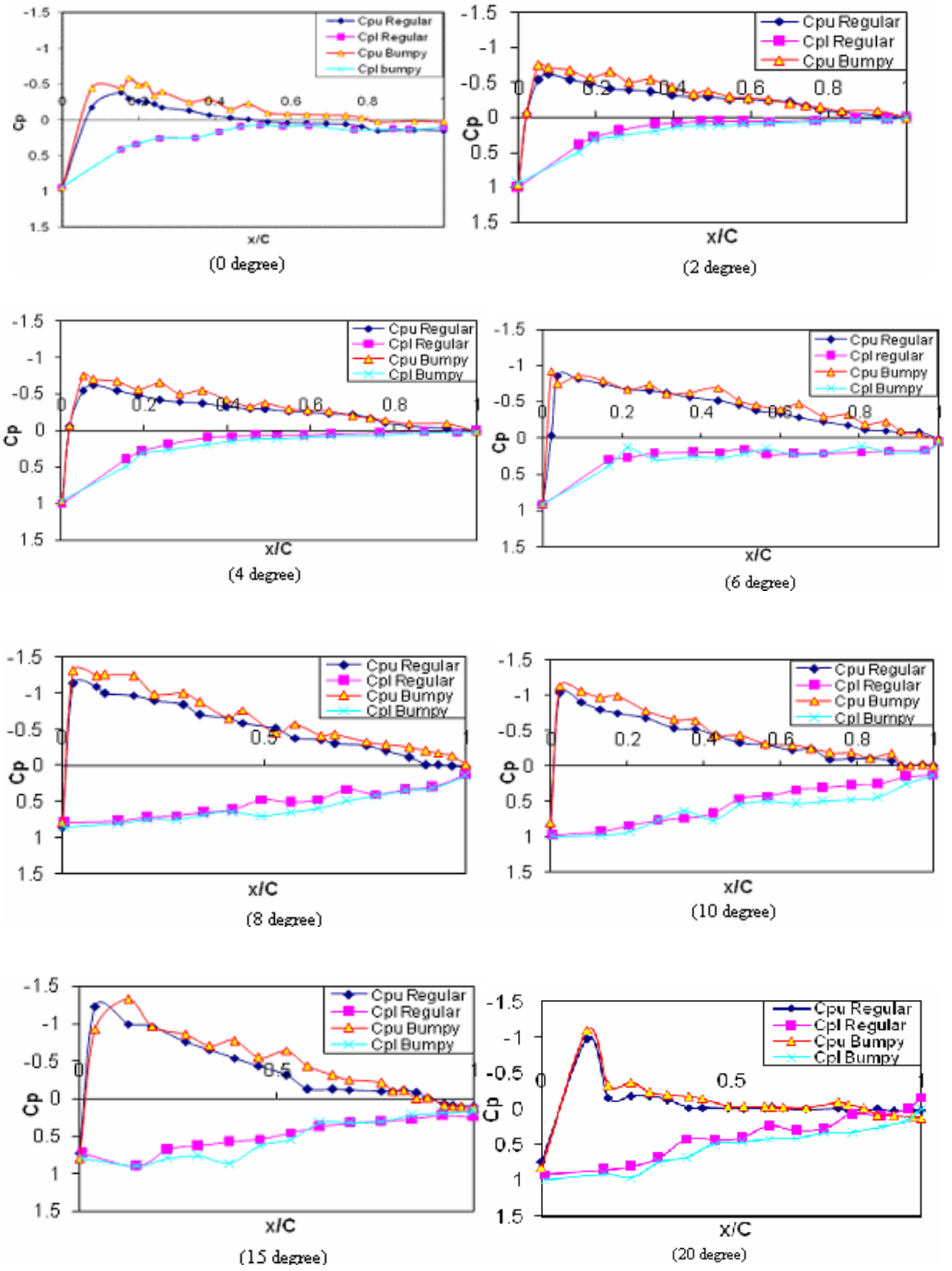

Fig. 3 External surface pressure distributions at the mid-span of the models

4.2. Lift, drag and moment co-efficient

Aerodynamic forces on the body are due entirely to two basic sources; firstly, pressure distribution on the body surface, and secondly shear stress distribution on the body surface. The net effect of the pressure and shear stress distributions integrated over the whole body surface is resultant aerodynamic force. In the present study, it is calculated the lift and drag coefficients only on the basis of the measured pressure distribution over the body surface. In this paper only upper surface pressure coefficients are considered to calculate the lift and drag coefficients.

The following equations are used to calculate the lift and drag coefficients:

Lift co-efficient $C_L = \frac{1}{c}\int_0^c (Cp_l - Cp_u)dx$

Drag co-efficient $C_D = \frac{1}{c}\int_0^c (Cp_l - Cp_u)dy$

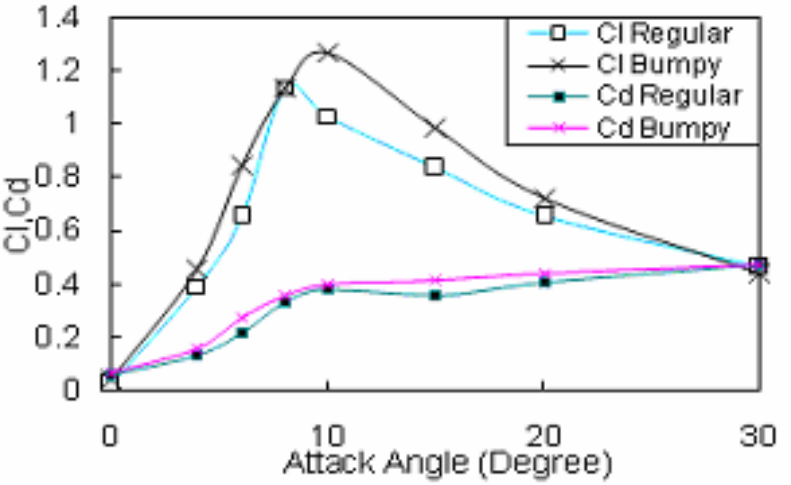

Fig.4 Variation of lift and drag coefficient with attack angle

Figure 4 shows the variation of lift and drag coefficient with attack angle. According to Fig. 4 it is clear to shown that the lift to drag ratio increases for introducing the surface roughness. According to Fig. 5 is has also been found that the bumpy surface wing is more stable than the regular surface wing.

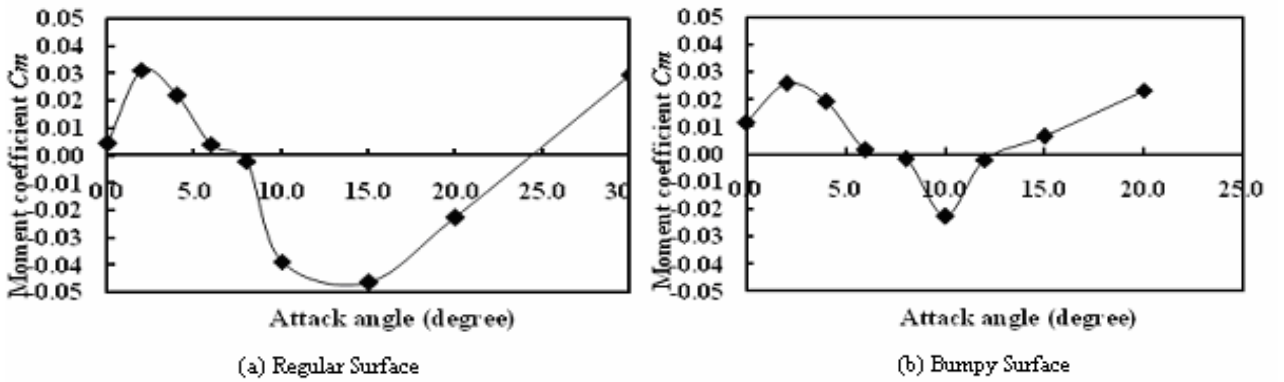

Fig. 5 Variation of moment coefficient with attack angle

5. CONCLUSION

From this experimental investigation it has been observed that the flow separation on the surface of the airfoil can be delayed by the modification with regular perturbations or “bumps”. It was found that the stall angle was delayed by about 20% when compared to the “smooth” baseline case, with increase in lift and decrease in drag. This provides the motivation to examine a potential passive flow control application of “large-scale” roughness in low *Re* flows. The lift of bumps surface airfoil will be greater than the smooth surface. This also implies that the bumpy surface improves the aerodynamic characteristics of the wing for low *Re* flow.

REFERENCES

[1] E. L. Houghton and P. W. Carpenter, “Aerodynamics for Engineering Students”, Fourth Edition, Edward Arnold Publisher.
[2] John D. Anderson, J.R, “Introduction to Flight”, Third Edition, Mc Graw-Hill International Editions, Aerospace Science Series.
[3] Dr. P. N. Modi & Dr. S. M Seth, “Hydraulics and Fluid Mechanics Including Machine” (In SI Unit), new edition 2005-2006, Standard Book House.
[4] William H. Rae, Jr. & Alan pope, “Low Speed Wind Tunnel Testing”, Second Edition, A Wiley – Inter science Publication.
[5] Charles E. Dole, “Flight Theory and Aerodynamics”, A Wiley Interscience Publication.
[6] Bernard Etkin, “Dynamics of Flight- Stability and Control”, Third edition, John Wiley & Sons, INC.
[7] Donald T. Ward, “Introduction to Flight Test Engineering”, Elsevier Science Publishers.

Proceedings of the 4th BSME-ASME International Conference on Thermal Engineering
27-29 December, 2008, Dhaka, Bangladesh

TORSION EFFECT ON FLUID FLOW IN A HELICAL PIPE WITH SQUARE CROSS-SECTION

Prabir Kumar Bhattacharjee* and Md. Mahmud Alam**
Mathematics Discipline, Khulna University, Khulna-9208, Bangladesh
Natural Science Group, National University, Gazipur-1704, Bangladesh*
e-mail: alam_mahmud2000@yahoo.com

ABSTRACT

Numerical study is performed to investigate the fluid flow through a helical pipe under various flow conditions. Spectral method is applied as a main tool for the numerical technique, where the Chebyshev polynomial, the Collocation methods, the Arc-length method and the Newton-Raphson method are also used as secondary tools. Steady flow through a helical pipe with square cross-section is investigated numerically to examine the combined effects of Dean number D_n *and torsion* τ'*. One of the interesting phenomena of the flow is the solution curve and the flow structure. The flow structures in the helical pipe are shown for various Dean Numbers and torsions at aspect ratio 1.0, where other parameters are fixed.*

Key Words: *Helical pipe, Dean number, Curvature, Torsion*

1. INTRODUCTION

The flow through a helical pipe is used extensively in various industrial applications, as in heat transfer equipment, chemical processes, propulsion systems, medical equipments and centrifugal compressors. The most important characteristic feature of flow in helical pipe is the development of the secondary flow which is circulating cross-sectionally. The extensive study of the flow through helical pipes is of importance for the design of industrial apparatus. Dean [1] was the first author who formulated the curved pipe problem in mathematical terms under the fully developed flow conditions. The reviews by Berger et al. [2] and Ito [3] may be referred to for flows in toroidally curved tubes. The curved tube inevitably has non-zero pitch if it has many turns and hence the tube is more or less in a helically coiled shape. The geometry of a helical pipe, as shown in fig.1, is characterized by the curvature and torsion. These non-dimensional curvature and torsion are defined, respectively, as, $\kappa' = \frac{r'}{r'^2 + \alpha'^2}$, $\tau' = \frac{\alpha'}{r'^2 + \alpha'^2}$ where r' is the radius of the helix and $\alpha' = \frac{pitch}{2\pi}$. The secondary flow caused by the centrifugal force due to curvature can be affected by torsion. If the pitch is equals to zero, then the torsion is equals to zero and the helical pipe reduces to the toroidally curved pipe. In a helical pipe the centrifugal force plays an important role in creating a pair of vortices. However, above a critical value of the Dean number, the secondary flow is changed from the appearance of several pair of vortices structure, due to the balance of the acting centrifugal and pressure gradient forces on the flow. The torsion causes the distortion in the symmetry of the flow, enlarging the upper vortex of the secondary flow at the expense of the lower vortex.

Wang [4] was the pioneer author who formulated the helical pipe flow for circular cross-section using non-orthogonal co-ordinates and analyzed the flow for small curvature and torsion by taking series expansions of these parameters. He found that the secondary flow is a single vortex cell. Yamamoto *et al*. [5] investigated numerically the flow through a helical pipe with circular cross-section for a wide range of the Dean number, curvature and torsion. There have been very few studies regarding the torsion effect on the flow in a helical square duct. The effect of small torsion on the helical square ducts has been investigated by Bolinder [6], Chen & Jah [7] and Alam et al.[8]

The main object of the present study is to investigate numerically the incompressible fully developed steady flow through a *left-handed helical pipe* with square cross-section for several values

*On leave: *Secondary and Higher Education Directorate, Bangladesh.*
** Corresponding author

of torsion and Dean number, $D_n = -\dfrac{a^3\sqrt{2\kappa'}}{\mu\nu}\dfrac{\partial p'}{\partial s'}$. Numerical results are obtained by employing spectral method as a main tool.

2. GOVERNING EQUATIONS

Consider a viscous incompressible fully developed steady flow through a helical pipe with square cross-section at a fixed curvature. Let $2a$ and $2b$ be the width and height of the cross-section respectively. We are considering only the case of $a = b$ in the present study. Here s is the coordinate along the centre line of the cross-section of the pipe which is shown in fig. 1. The curvature κ and torsion τ mentioned above are determined by the Serret-Frenet formulae

$$\frac{d\mathbf{T}}{ds} = \kappa\mathbf{N},\ \frac{d\mathbf{N}}{ds} = \tau\mathbf{B} - \kappa\mathbf{T},\ \frac{d\mathbf{B}}{ds} = -\tau\mathbf{N} \tag{1}$$

$\mathbf{T}$, the unit tangent vector along s, $\tilde{\mathbf{N}}$ and $\tilde{\mathbf{B}}$ are the orthogonal unit vectors obtained by a rotation of the physical basis vector $\mathbf{N}$ and $\mathbf{B}$ with the angle $\sigma(s)$ in the $\mathbf{N}-\mathbf{B}$ plane which is shown in Fig.2. Therefore, we have

$$\tilde{\mathbf{N}} = \cos\sigma\,\mathbf{N} - \sin\sigma\,\mathbf{B} \quad \text{and} \quad \tilde{\mathbf{B}} = \sin\sigma\,\mathbf{N} + \cos\sigma\,\mathbf{B} \tag{2}$$

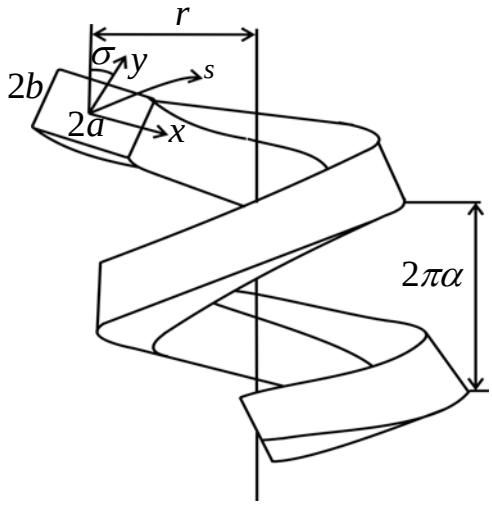

Fig.1 Helical duct with rectangular cross-section.

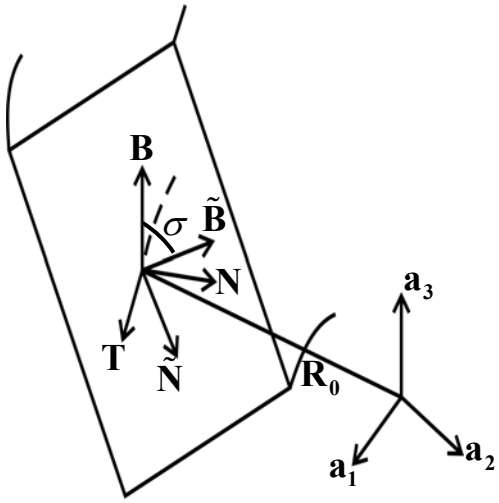

Fig.2 Various vectors related to the centre-line of a duct.

The continuity and Navier-Stokes equations can be put in the following tensor form:

$$\frac{\partial}{\partial\xi^i}\left(\sqrt{g}\ q_j\ \gamma^i_j\right) = 0 \tag{3}$$

$$\frac{\partial q_i}{\partial t} + \gamma^k_j\left(\frac{\partial q_i}{\partial\xi^k} - q_l E_{lik}\right)q_j = -\frac{1}{\rho}\frac{\partial p}{\partial\xi^j}\gamma^j_i - \nu\varepsilon_{ijk}\gamma^l_j\left(\frac{\partial(\nabla\wedge\mathbf{q})_k}{\partial\xi^l} - (\nabla\wedge\mathbf{q})_m E_{mkl}\right), \tag{4}$$

where $(\nabla\wedge\mathbf{q})_i = \varepsilon_{ijk}\ \gamma^l_j\left(\dfrac{\partial q_k}{\partial\xi^l} - q_m E_{mkl}\right)$.

The variables are non-dimensionalised by the characteristic length a (half width) and the kinematic viscosity ν as follows:

$$u = \frac{\nu}{a}u',\ v = \frac{\nu}{a}v',\ w = \frac{\nu}{a}\frac{w'}{\sqrt{2\kappa'}},\ \kappa = \frac{\kappa'}{a}, \tau = \frac{\tau'}{a},\ p = \rho\frac{\nu^2}{a^2}p',\ \ s = s'a,\ \ x = x'a,\ \ y = y'a \tag{5}$$

Here w', u', v' are non-dimensional velocity components in the direction of s', x', y' respectively and p', κ', τ' are the non-dimensional pressure, curvature and torsion respectively. The variables without prime are the dimensional quantities. For the incompressible fully developed flow, the velocity is independent of s'. We further introduce a new variable $y' = \gamma\bar{y}$, where $\gamma\left(=\dfrac{b}{a}\right)$ is the aspect ratio of the

cross-section. Since the flow field is uniform in the axial direction, the stream function $\psi = \psi(x', y')$ is introduced as

$$\frac{\partial \psi}{\partial y'} = Ju'\sqrt{2\kappa'} + \tau' y' w', -\frac{\partial \psi}{\partial x'} = Jv'\sqrt{2\kappa'} - \tau' x' w' \tag{6}$$

where $J = 1 - \kappa' x'$.

The basic equations for w' and ψ are then derived from the Navier-Stokes equations as follows:

$$D_n - \frac{\tau' x'}{J}\left(1 + \frac{\tau'^2\gamma^2\bar{y}^2}{J^2}\right)\psi_{x'x'x'} - \frac{\tau'\bar{y}}{J}\left(1 + \frac{\tau'^2\gamma^2\bar{y}^2}{J^2} - \frac{2\tau'^2x'^2}{J^2}\right)\psi_{x'x'\bar{y}} - \frac{\tau'\bar{y}}{J\gamma^2}\left(\frac{\tau'^2x'^2}{J^2} + 1\right)\psi_{\bar{y}\bar{y}\bar{y}}$$
$$+ \frac{\tau' x'}{J\gamma^2}\left(\frac{2\tau'^2\gamma^2\bar{y}^2}{J^2} - 1 - \frac{\tau'^2x'^2}{J^2}\right)\psi_{x'\bar{y}\bar{y}} - \frac{3\kappa'\tau'\bar{y}}{J^2}\left(1 + \frac{\tau'^2\gamma^2\bar{y}^2}{J^2} - \frac{2\tau'^2x'}{\kappa' J} - \frac{\tau'^2x'^2}{J^2}\right)\psi_{x'\bar{y}} - \frac{\tau'}{J^2}\left(\frac{2\tau'^2\gamma^2\bar{y}^2}{J} + \kappa' x'\right.$$
$$\left. + \frac{3\kappa'\tau'^2x'\gamma^2\bar{y}^2}{J^2} - \frac{\tau'^2x'^2}{J}\right)\psi_{x'x'} + \frac{\tau'}{J\gamma^2}\left(\frac{3\kappa'\tau'^2x'\gamma^2\bar{y}^2}{J^3} - \frac{2\tau'^2x'^2}{J^2} + 2\kappa' x' + \frac{\tau'^2\gamma^2\bar{y}^2}{J^2}\right)\psi_{\bar{y}\bar{y}} - \frac{\tau'\bar{y}}{J^3}\left(\frac{3\kappa'^2\tau'^2\gamma^2\bar{y}^2}{J^2}\right.$$
$$\left. - \frac{4\kappa'\tau'^2x'}{J} - \tau'^2 + 3\kappa'^2\right)\psi_{\bar{y}} - \frac{2\tau'^2x'\bar{y}}{J}\left(\frac{\tau'^2\gamma^2\bar{y}^2}{J^2} + \frac{\tau'^2x'^2}{J^2} + 1\right)w'_{x'\bar{y}} - \frac{\tau'}{J^2}\left(\frac{3\kappa'\tau'^2\gamma^2\bar{y}^2}{J^2} + \frac{\kappa'^2x'}{J} - \frac{\tau'^2x'}{J} + \kappa'\right.$$
$$\left. + \frac{3\kappa'^2\tau'^2x'\gamma^2\bar{y}^2}{J^3} - \frac{\kappa'\tau'^2x'^2}{J^2}\right)\psi_{x'} + \left(\frac{2\tau'^2\gamma^2\bar{y}^2}{J} + \frac{\tau'^4\gamma^4\bar{y}^4}{J^3} + \frac{\tau'^2x'^2}{J} + \frac{\tau'^4x'^2\gamma^2\bar{y}^2}{J^3} + J\right)w'_{x'x'} + \left(\frac{\tau'^2\bar{y}^2}{J} + \frac{\tau'^4x'^2\bar{y}^2}{J^3}\right.$$
$$\left. + \frac{2\tau'^2x'^2}{J\gamma^2} + \frac{J}{\gamma^2} + + \frac{\tau'^4x'^4}{J^2\gamma^2}\right)w'_{\bar{y}\bar{y}} + \left(\frac{3\kappa'\tau'^4\gamma^4\bar{y}^4}{J^4} + \frac{\tau'^2x'}{J} - \frac{\tau'^4x'\gamma^2\bar{y}^2}{J^3} + \frac{2\kappa'\tau'^2\gamma^2\bar{y}^2}{J^2} + \frac{\kappa'\tau'^2x'^2}{J^2} + \frac{3\kappa'\tau'^4x'^2\gamma^2\bar{y}^2}{J^4} - \kappa'\right.$$
$$\left. - \frac{\tau'^4x'^4}{J^3}\right)w'_{x'} + \frac{\tau'^2}{J}\left(-\frac{\kappa'x'\bar{y}}{J} - \frac{\tau'^2x'^2\bar{y}}{J^2} + \bar{y} - \frac{\tau'^2\gamma^2\bar{y}^3}{J^2} - \frac{3\kappa'\tau'^2x'\gamma^2\bar{y}^3}{J^3} - \frac{3\kappa'\tau'^2x'^3\bar{y}}{J^3}\right)w'_{\bar{y}} + \frac{\kappa'}{J}\left(\frac{3\kappa'\tau'^4\gamma^4\bar{y}^4}{J^4} - \kappa'\right.$$
$$\left. - \frac{\tau'^4x'\gamma^2\bar{y}^2}{J^3} - \frac{\kappa'\tau'^2\gamma^2\bar{y}^2}{J^2} + \frac{\tau'^2x'}{J} + \frac{\kappa'\tau'^2x'^2}{J^2} + \frac{3\kappa'\tau'^4x'^2\gamma^2\bar{y}^2}{J^4} - \frac{\tau'^4x'^3}{J^3} + \frac{3\kappa'\tau'^2\gamma^2\bar{y}^2}{J^2}\right)w' - \frac{1}{\gamma\sqrt{2\kappa'}}\left[\left(\frac{\tau'^2x'^2}{J^2}\right.\right.$$
$$\left.\left. + \frac{\tau'^2\gamma^2\bar{y}^2}{J^2} + 1\right)w'_x\psi_{\bar{y}} - \frac{\kappa'\tau'x'}{J^3}\psi_{x'}\psi_{\bar{y}} + \left(\frac{\kappa'\tau'^2x'^2}{J^3} + \frac{\kappa'\tau'^2\gamma^2\bar{y}^2}{J^3} + \frac{2\tau'^2x'}{J^2} - \frac{\kappa'}{J}\right)w'\psi_{\bar{y}} - \left(\frac{\tau'^2\gamma^2\bar{y}^2}{J^2} + 1 + \frac{\tau'^2x'2}{J^2}\right)w'_{\bar{y}}\psi_{x'}\right]$$
$$- \frac{\tau'}{J^2\sqrt{2\kappa'}}\left(\frac{\bar{y}}{\gamma}\psi_{x'}\psi_{\bar{y}\bar{y}} + \frac{x'}{\gamma}\psi_{x'}\psi_{x'\bar{y}} - \frac{\bar{y}}{\gamma}\psi_{\bar{y}}\psi_{x'\bar{y}} - 2\tau'\gamma\,\bar{y}\,w'\psi_{x'} - \frac{x'}{\gamma}\psi_{\bar{y}}\psi_{x'x'}\right) + \frac{\kappa'\tau'\bar{y}}{J^3\gamma\sqrt{2\kappa'}}\psi_{\bar{y}}^2 = 0. \tag{7}$$

$$\frac{1}{J\sqrt{2\kappa'}}\left[\left(1 + \frac{\tau'^2\gamma^2\bar{y}^2}{J^2}\right)\psi_{x'x'x'x'} + \left(1 + \frac{\tau'^2x'^2}{J^2}\right)\frac{1}{\gamma^4}\psi_{\bar{y}\bar{y}\bar{y}\bar{y}}\right] - \frac{2\tau'^2\,x'\,\bar{y}}{J^3\gamma^2\sqrt{2\kappa'}}\psi_{x'\bar{y}\bar{y}\bar{y}} - \frac{2\tau'^2x'\,\bar{y}}{J^3\sqrt{2\kappa'}}\psi_{x'x'x'\bar{y}} + \frac{1}{J\sqrt{2\kappa'}}\left(2 + \frac{\tau'^2x'^2}{J^2}\right.$$
$$\left. + \frac{\tau'^2\gamma^2\,\bar{y}^2}{J^2}\right)\frac{1}{\gamma^2}\psi_{x'x'\bar{y}\bar{y}} + \frac{1}{J^2\sqrt{2\kappa'}}\left(2\kappa' + \frac{6\kappa'\tau'^2\gamma^2\bar{y}^2}{J^2} - \frac{\tau'^2x'}{J}\right)\psi_{x'x'x'} + \frac{1}{J^2\sqrt{2\kappa'}}\left(\frac{3\kappa'\tau'^2x'^2}{J^2}\right.$$
$$\left. + \frac{3\kappa'\tau'^2\gamma^2\bar{y}^2}{J^2} + 2\kappa' - \frac{\tau'^2x'}{J}\right)\frac{1}{\gamma^2}\psi_{x'\bar{y}\bar{y}} - \frac{\tau'^2\,\bar{y}}{J^3\sqrt{2\kappa'}}\left(\frac{9\kappa'x'}{J} + 1\right)\psi_{x'x'\bar{y}} - \frac{\tau'^2\bar{y}}{J^3\gamma^2\sqrt{2\kappa'}}\left(\frac{3\kappa'x'}{J} + 1\right)\psi_{\bar{y}\bar{y}\bar{y}}$$
$$+ \frac{\kappa'}{J^3\sqrt{2\kappa'}}\left(3\kappa' + \frac{15\kappa'\tau'^2\gamma^2\bar{y}^2}{J^2} - \frac{4\tau'^2x'}{J}\right)\psi_{x'x'} + \frac{\kappa'\tau'^2}{J^4\gamma^2\sqrt{2\kappa'}}\left(2x' + \frac{3\kappa'\gamma^2\,\bar{y}^2}{J}\right)\psi_{\bar{y}\bar{y}} - \frac{6\kappa'\tau'^2\bar{y}}{J^4\sqrt{2\kappa'}}\left(\frac{2\kappa'x'}{J} + 1\right)\psi_{x'\bar{y}}$$
$$+ \frac{\kappa'}{J^4\sqrt{2\kappa'}}\left(3\kappa'^2 + \frac{15\kappa'^2\tau'^2\gamma^2\,\bar{y}^2}{J^2} - \frac{4\kappa'\tau'^2x'}{J} - \tau'^2\right)\psi_{x'} - \frac{6\kappa'^2\tau'^2\bar{y}}{J^5\sqrt{2\kappa'}}\psi_{\bar{y}} - \frac{\kappa'\tau'}{J^3\sqrt{2\kappa'}}\left(4\kappa' + \frac{3\kappa'^2x'}{J} + \frac{15\kappa'^2\tau'^2x'\gamma^2\,\bar{y}^2}{J^3}\right.$$
$$\left. - \frac{4\kappa'\tau'^2x'^2}{J^2} + \frac{12\kappa'\tau'^2\gamma^2\bar{y}^2}{J^2} - \frac{3\tau'^2x'}{J}\right)w' - \frac{\tau'}{J^2\sqrt{2\kappa'}}\left(4\kappa' + \frac{3\kappa'^2x'}{J} + \frac{15\kappa'^2\tau'^2x'\gamma^2\,\bar{y}^2}{J^3} - \frac{4\kappa'\tau'^2x'^2}{J^2} - \frac{3\tau'^2x'}{J}\right.$$
$$\left. + \frac{12\tau'^2\kappa'\gamma^2\,\bar{y}^2}{J^2}\right)w'_{x'} + \frac{\tau'\,\bar{y}}{J^3\sqrt{2\kappa'}}\left(\frac{12\kappa'^2\tau'^2x'^2}{J^2} + \frac{16\kappa'\tau'^2x'}{J} + 3\tau'^2 - \frac{3\kappa'^2\tau'^2\gamma^2\,\bar{y}^2}{J^2} + \kappa'^2\right)w'_{\bar{y}} + \frac{\tau'\bar{y}}{J^2\sqrt{2\kappa'}}\left(\frac{9\kappa'\tau'^2x'^2}{J^2}\right.$$
$$\left. + \frac{10\tau'^2x'}{J} - \frac{3\kappa'\tau'^2\gamma^2\bar{y}^2}{J^2} + \kappa'\right)w'_{x'\bar{y}} - \frac{\tau'}{J^2\sqrt{2\kappa'}}\left(\frac{6\kappa'\tau'^2x'\gamma^2\bar{y}^2}{J^2} + 2\kappa'x' + 4J + \frac{4\tau'^2\gamma^2\,\bar{y}^2}{J} - \frac{\tau'^2x'^2}{J}\right)w'_{x'x'}$$

$$-\frac{\tau'}{J\sqrt{2\kappa'}}\left(\frac{3\kappa' x'}{J\gamma^2}+\frac{4}{\gamma^2}+\frac{4\tau'^2x'^2}{\gamma^2J^2}+\frac{3\kappa'\tau'^2x'^2}{\gamma^2J^3}-\frac{\tau'^2\,\bar{y}^2}{J^2}-\frac{3\tau'^2\kappa' x'\,\bar{y}^2}{J^3}\right)w'_{\bar{y}\bar{y}}+\frac{\tau' x'}{J\sqrt{2\kappa'}}\left(\frac{2\tau'^2\,\bar{y}^2}{J^2}-\frac{1}{\gamma^2}-\frac{\tau'^2x'^2}{J^2\gamma^2}\right)w'_{x'\bar{y}\bar{y}}$$
$$-\frac{\tau' x'}{J\sqrt{2\kappa'}}\left(1+\frac{\tau'^2\gamma^2\bar{y}^2}{J^2}\right)w'_{x'x'x'}+\frac{\tau'\bar{y}}{J\sqrt{2\kappa'}}\left(\frac{2\tau'^2x'^2}{J^2}-1-\frac{\tau'^2\gamma^2\,\bar{y}^2}{J^2}\right)w'_{x'x'\bar{y}}-\frac{\tau'\bar{y}}{J\gamma^2\sqrt{2\kappa'}}\left(1+\frac{\tau'^2x'^2}{J^2}\right)w'_{\bar{y}\,\bar{y}\bar{y}}-\frac{\tau'^2\,\gamma\,\bar{y}}{J^3}w'^2$$
$$-\frac{1}{\gamma^3J^3}\psi_{\bar{y}}\,\psi_{\bar{y}\bar{y}}-\frac{3}{2\gamma J^3}\psi_{\bar{y}}\psi_{x'x'}+\frac{\tau'}{\gamma J^2}\left(\frac{2}{\kappa'}+\frac{3x'}{2J}\right)w_{x'}\psi_{\bar{y}}-\frac{3\kappa'}{2\gamma J^4}\psi_{x'}\psi_{\bar{y}}-\frac{1}{2\kappa'\gamma^3J^2}\psi_{x'\bar{y}\bar{y}}\psi_{\bar{y}}+\frac{1}{2\kappa'\gamma^3J^2}\psi_{x'}\,\psi_{\bar{y}\bar{y}\bar{y}}$$
$$-\frac{1}{2\kappa'\gamma J^2}\psi_{\bar{y}}\,\psi_{x'x'x'}-\frac{\tau'}{\gamma J^2}\left(\frac{2}{\kappa'}+\frac{x'}{J}\right)w'_{\bar{y}}\psi_{x'}+\frac{1}{2\gamma J^3}\psi_{x'}\psi_{x'\bar{y}}+\frac{1}{2\kappa'\gamma J^2}\psi_{x'}\,\psi_{x'x'\bar{y}}+\frac{3\tau'}{\gamma J^3}\left(1+\frac{\kappa' x'}{2J}\right)w'\psi_{\bar{y}}$$
$$+\frac{\tau'\bar{y}}{2\kappa'\gamma J^2}w'_{x'\bar{y}}\,\psi_{\bar{y}}+\frac{\tau' x'}{2\gamma J^3}w'\psi_{x'\bar{y}}+\frac{\tau' x'}{2\kappa'\gamma J^2}w'_{x'}\psi_{x'\bar{y}}-\frac{\tau'\,\bar{y}}{2\kappa'\gamma J^2}w'_{\bar{y}}\,\psi_{x'\bar{y}}-\frac{1}{\gamma J}\left(1-\frac{\tau'^2x'}{\kappa' J}\right)w'w'_{\bar{y}}-\frac{\tau' x'}{2\kappa'\gamma J^2}w'_{\bar{y}}\,\psi_{x'x'}$$
$$-\frac{\tau'^2\gamma\bar{y}}{\kappa' J^2}w'w'_{x'}+\frac{\tau'\,\bar{y}}{2\gamma J^3}w'\psi_{\bar{y}\bar{y}}+\frac{\tau'\,\bar{y}}{2\kappa'\gamma J^2}w'_{x'}\,\psi_{\bar{y}\bar{y}}+\frac{\tau'\bar{y}}{2\gamma J^3}w'_{\bar{y}}\psi_{\bar{y}}-\frac{\tau'\,\bar{y}}{2\kappa'\gamma J^2}w'_{\bar{y}\bar{y}}\psi_{x'}+\frac{\tau' x'}{2\kappa'\gamma J^2}w'_{x'x'}\psi_{\bar{y}}-\frac{\tau' x'}{2\kappa'\gamma J^2}w'_{x'\bar{y}}\psi_{x'}$$
$$=0 \qquad (8)$$

3. CALCULATION TECHNIQUE

The present work is mainly based on numerical methods. For this purpose the method adopted in the present numerical calculation is the spectral method, in which variables are expanded in series of functions consisting of Chebyshev polynomials. That is, the expansion functions $\Phi_n(x')$ and $\Psi_n(x')$ are expressed as

$$\Phi_n(x')=(1-x'^2)C_n(x'),\ \Psi_n(x')=(1-x'^2)^2C_n(x') \qquad (9)$$

where $C_n(x')=\cos(n\cos^{-1}(x'))$ is the n-th order Chebyshev polynomial. The functions $w'(x',y')$ and $\Psi(x',y')$ are expanded in terms of the functions $\Phi_n(x')$ and $\Psi_n(x')$ as

$$w'(x',y')=\sum_{m=0}^{M}\sum_{n=0}^{N}w_{mn}\Phi_m(x')\,\Phi_n(y') \ \text{ and } \ \Psi(x',y')=\sum_{m=0}^{M}\sum_{n=0}^{N}\psi_{mn}\Psi_m(x')\,\Psi_n(y') \qquad (10)$$

where M and N are the truncation numbers of the polynomial series in the x' and y' directions respectively and w_{mn} and ψ_{mn} are the coefficients of expansion. In order to obtain the solutions for expansion coefficients w_{mn} and ψ_{mn}, the expansion series (10) are then substituted into the basic equations (7) and (8) and the collocation method (Gottlieb and Orszag [9]) is applied in x' and y' directions yield a set of non-linear differential equations for w_{mn} and ψ_{mn} .The collocation points $\left(x_i', y_J'\right)$ are taken as $x_i'=\cos\left[\pi\left(1-\frac{i}{M+2}\right)\right], y_i'=\cos\left[\pi\left(1-\frac{j}{N+2}\right)\right]$, where $i=1,2,\cdots,M+1$ and $j=1,2,\cdots,N+1$. The steady solutions are obtained by the Newton-Raphson iteration method and the convergence is assured by taking $\in_{\bar{p}}<10^{-8}$, where subscript $\bar{p}$ denotes the iteration number and $\in_{\bar{p}}$ is defined as, $\in_{\bar{p}}=\sum_{m=0}^{M}\sum_{n=0}^{N}\left[\left(w_{mn}^{(\bar{p}+1)}-w_{mn}^{(\bar{p})}\right)^2+\left(\Psi_{mn}^{(\bar{p}+1)}-\Psi_{mn}^{(\bar{p})}\right)^2\right]$ (11)

In the present numerical calculations, $M=20$ and $N=20$ have been used to give sufficient accuracy of the solutions.

4. FLUX THROUGH THE HELICAL PIPE

The dimensional total flux, Q' through the $x'-y'$ plane is obtained as:

$$Q'=\int_{-b}^{b}\int_{-a}^{a}w_n'dx'dy'=\nu aQ$$

where, w_n' is the component of the velocity normal to $x'-y'$ plane and

$Q=\int_{-\gamma}^{\gamma}\int_{-1}^{1}\frac{1-\kappa' x'}{\sqrt{\left(1-\kappa' x'\right)^2+\alpha'^2\kappa'^2}}w'dx'dy'$ is the dimensionless total flux and resistance coefficient $\left(R_c\right)$ is calculated by flux .

5. RESULTS AND DISCUSSION

We take helical pipe having aspect ratio (γ) to investigate the flow characteristics for fixed curvature $(\kappa' = 0.1)$, a wide range of Dean numbers (D_n) and different torsions $(\tau' = 0.0, 0.1)$. For the above mentioned purpose the following two cases have been considered.

Case I

($\gamma = 1, \kappa' = 0.1, \tau' = 0$):

Figure 3 shows that the resistance coefficient through the pipe versus Dean number and this is called solution curve. In this solution curve, we have obtained three bifurcation areas which are the important characteristics of the flow in curved as well as helical pipe. Here, resistance coefficient decreases as Dean number increases along the curves S_{11}, S_{13}, S_{21}, S_{23}, S_{25}, S_{31}, S_{33}, S_{35} and the resistance coefficient increases as Dean number decreases along the curves S_{12}, S_{22}, S_{24}, S_{32} and S_{34} in the bifurcation areas. In fig. 4, the steady solution consists of 2-vortex, 4-vortex with two week vortex and strong four vortex secondary flow patterns for the same Dean number 680. In fig. 5 the steady solution consists of 10-vortex secondary flow patterns along the curves S_{21}, S_{22}, S_{23}, S_{24} and S_{25} for the Dean number 7250. In fig. 6, 12-vortex secondary flow patterns are found along the curves S_{31}, S_{32}, S_{33}, S_{34} and S_{35}, which are gradually becoming strong for Dean number 10001. The above three figures show that the axial flow is shifted more quickly towards the outer wall of the cross-section. In these figures the inner wall is to the right side and the outer wall is to the left side of the cross-section.

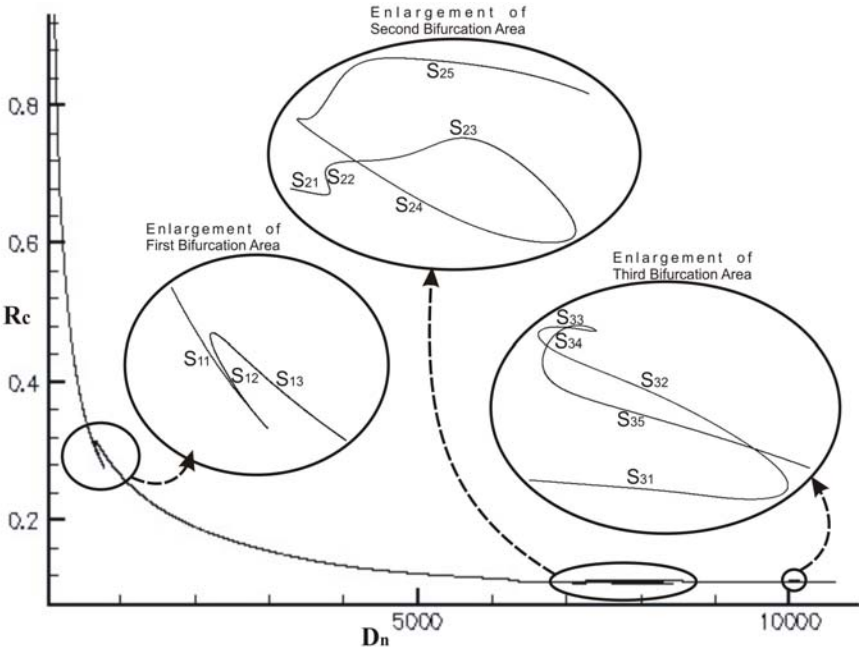

Fig.3 State diagram for the resistance coefficient R_C versus the Dean number D_n for $\tau' = 0.0$.

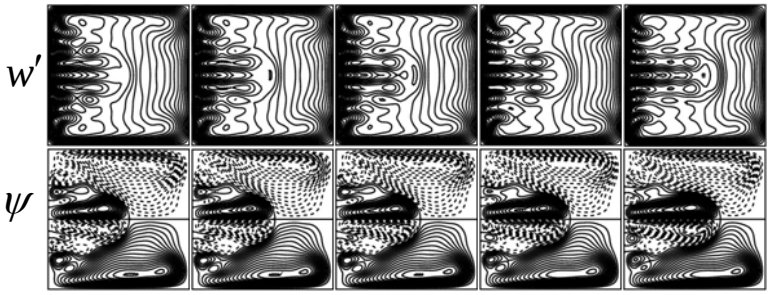

Fig.5 Contour plots of axial flow and streamlines of the secondary flow on the second bifurcation area for D_n=7250 and κ' =0.1

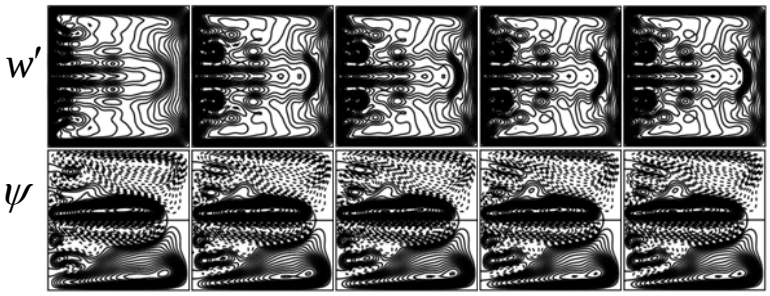

Fig.6 Contour plots of axial flow and streamlines of the secondary flow on the third bifurcation area for D_n=10001 and κ' =0.1

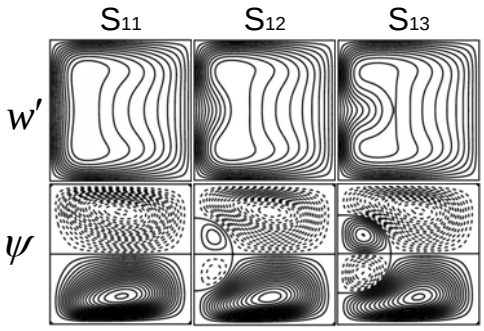

Fig.4 Contour plots of axial flow and streamlines of the secondary flow on the first bifurcation area for D_n=680 and κ' =0.1

Case II ($\gamma = 1, \kappa' = 0.1, \tau' = 0.1$): The flux through the pipe for various Dean numbers is shown in fig.7. Here, a single bifurcation area is found. The curves S_1 and S_2 indicate the flux increases as Dean

number increases. The bifurcation area includes the Dean number 691 and 692. At these two points both 2-vortex and 4-vortex secondary flow patterns are found and the maximum axial flow is shifted towards the outer wall of the cross-section which is shown in fig 8.

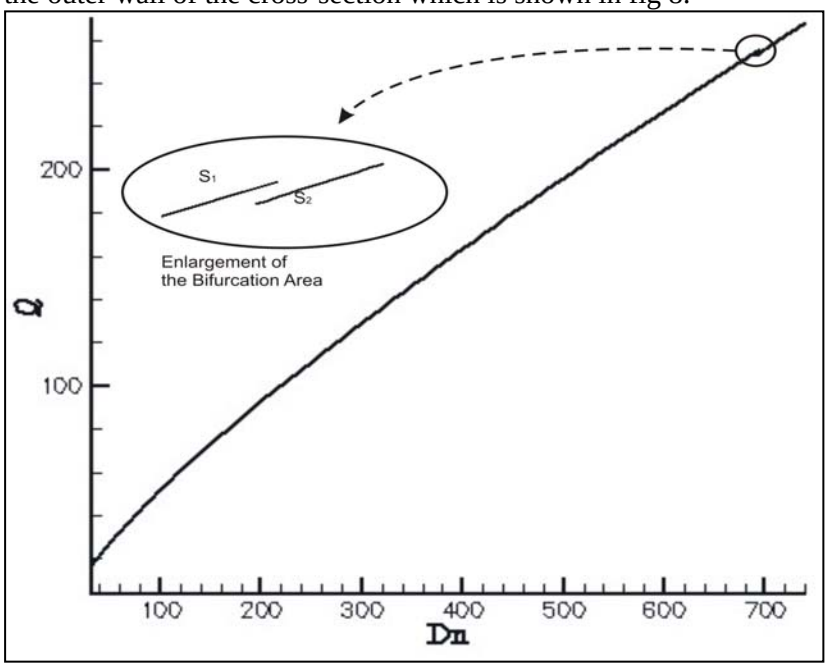

Fig. 7 State diagram for the dimensionless flux *Q* versus the Dean number Dn for $\tau' = 0.1$ and $\kappa' = 0.1$.

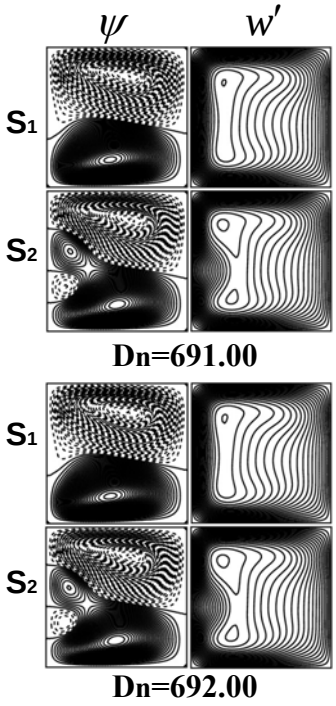

Fig. 8 Streamlines of the Secondary flow and Contour Plots of Axial Flow on the Bifurcation Area for $\tau' = 0.1$ and $\kappa' = 0.1$

6. CONCLUSIONS

Multiple pair of vortices has been found in the bifurcation areas due to centrifugal and torsional forces. The results indicate that for very small values of torsion the effects of centrifugal force are significant which bring about many bifurcation areas.

7. REFERENCES

[1] Dean, W. R., Note on the Motion of Fluid in a Curved Pipe, *Philosophical Magazine and Journal of Science*, 4 (1927), 20, pp. 208-223.

[2] Berger, S. A., Talbot, L., Yao, L. S., Flow in curved pipes, *Annual Review of Fluid Mechanics*, 15 (1983), pp. 461-512.

[3] Ito, H., Flow in curved pipes, *JSME International Journal*, 30 (1987), pp. 543-552.

[4] Wang, C. Y., On the low-Reynolds number flow in a helical pipe, *Journal of Fluid Mechanics*, 108 (1981), pp. 185-194.

[5] Yamamoto, K., Yanase, S., Yoshida, T., Torsion effects on the flow in a helical pipe, *Fluid Dynamics Research*, 14 (1994), pp. 259-273.

[6] Bolinder, C. J., The effect of Torsion on the Bifurcation structure of laminar flow in a Helical Square Duct, *ASME Journal of Fluids Engineering*, 117 (1995), pp. 242-248.

[7] Chen, W.H., Jan, R., The Torsion Effect on fully developed Flow in Helical Square Ducts, *Journal of Fluid Mechanics*, 115 (1993), pp. 292-301.

[8] Alam, M. M., Ota, M., Ferdows, M., Islam, M. N., Wahiduzzaman, M., Yamamoto, K., Flow through a rotating helical pipe with a wide range of the Dean number, *Archives of Mechanics, Warszawa*, 59 (2007), 6, pp. 501-517.

[9] Gottlieb, D. and Orszag, S. A., Numerical Analysis of Spectral Methods, Society for Industrial and Applied Mathematics, Philadelphia, 1977.

Proceedings of the 4th BSME-ASME International Conference on Thermal Engineering
27 -29 December 2008, Dhaka, Bangladesh

EFFECT OF MACH NUMBER AND SUB-CAVITY ON THE CONTROL OF CAVITY-INDUCED PRESSURE OSCILLATIONS

Md. Mahbubul Alam[1], Toshiaki Setoguchi[2], Shigeru Matsuo[2] and Heuy Dong Kim[3]

[1]Dept. of Mech. Eng., Chittagong University of Engineering and Technology, Chittagong-4349, Bangladesh.
[2]Department of Mechanical Engineering, Saga University, 1 Honjo-machi, Saga 840-8502, Japan.
[3]School of Mechanical Engineering, Andong National University, Andong 760-749, Korea
(Email: malam@cuet.ac.bd)

ABSTRACT

Numerical investigations have been conducted to determine the effect of inlet Mach number and sub-cavity on the control of cavity-induced pressure oscillations in two-dimensional supersonic flow. A passive control method with a sub-cavity on the front wall of a square cavity covered by a flat plate at Mach number 1.50, 1.83 and 2.50 was studied for the purpose. The results showed that sub-cavity is effective in reducing the oscillations at different inlet Mach numbers. The results also showed that the resultant amount of attenuation of pressure oscillations was dependent on the inlet Mach number, length of the flat plate, and also on the depth of the sub-cavity used as an oscillation suppressor.

Key words: *Compressible flow, Supersonic cavity, Pressure oscillations, Passive control*

1. INTRODUCTION

Supersonic cavity flows can generate intense pressure oscillations that become a practical problem in many engineering applications. Although the study and control of cavity-induced oscillations has been the subject of numerous research investigations [1-7], the practical means of effective control in a wide range of flow conditions are still to be investigated. Heller and Bliss [4] among the earliest researchers suggested that oscillations could be controlled by slanting the trailing edge of a cavity. Shaw et al. [5] conducted wind tunnel tests with cavities installed on a model of an aircraft to assess the leading-edge sawtooth suppressors and the slanted trailing edges. He found that the slanted trailing edge was effective in attenuating cavity tones but the leading-edge spoilers were not fully successful. Sarno and Franke [6] studied static and oscillating fences and found that the static fences were effective in suppressing cavity pressure levels. Alam et al. [7] studied sub-cavity at Mach number 1.83 and showed that a sub-cavity was very effective in reducing the oscillations. Although most of the methods mentioned here have been shown success in reducing the oscillations, their effectiveness should be investigated in a changing flow environment.

2. CFD ANALYSIS

The governing equations are the unsteady compressible Navier-Stokes equations coupled with turbulence kinetic energy and eddy viscosity equations for modeling the turbulence [8-10]. A third-order TVD finite difference scheme with MUSCL [11] was used to discretize the spatial derivatives and a second order-central difference scheme for the viscous terms, and a second-order fractional step was employed for time integration.

Figure 1 shows the grids and computational domain of the cavity. The height of the main flow section above the cavity is 24 mm. The depth D and the length L of the cavity are the same and equal to 12 mm. The ratios of the length l of the flat plate to the depth of the cavity D are l/D = 0, -0.125, -0.1875 and -0.25, and the ratio of the lip thickness t to the depth of the baseline cavity D is t/D = 0.05. The ratios of the depth of sub-cavity d to the depth of the baseline cavity D are d/D = 0.25, 0.30, 0.35, 0.45, 0.65, 0.70 and 0.75 in the simulations. S1 in Fig.1(b) denotes the measuring position of static pressure. The number of grids is 200×80 in the region of the nozzle and 50×60 in the cavity.

In the present study, dry air is used as a working gas and assumed to be thermally and calorically perfect. Pressure p_0 in the reservoir is 101.3 kPa. The inlet Mach number M_{inlet} at the entrance of the cavity is 1.50, 1.83 and 2.50. The Reynolds number is 2.1×10^5. On the solid walls, the no-slip and no heat transfers were applied as the boundary conditions. Fixed conditions were set for the inflow. Zero order extrapolation was used at the outflow.

3. RESULTS AND DISCUSSION

3.1 Baseline Case

Figure 2 shows contour maps of density during one period of flow oscillation for the cavity without control at Mach number 1.83. Here, f represents the dominant frequency, which is equal to 17.5 kHz (see Fig.5(b)). It was observed that a compression wave (CW) from the trailing edge of the cavity moves upstream as time proceeds. The upstream compression waves impinge on the cavity leading edge (Fig.2(d)) and disturb the shear layer. This disturbance regenerates instability waves in the shear layer. While the shear layer reattaches at the rear wall of the cavity, generation of compression waves (CW) occurs due to the impingement of instability waves on the wall as shown in Fig.2 (b) and thus completing the formation of feedback loop which is widely believe to be the reason of intense pressure oscillations. Contour maps of density in case of inlet Mach number 1.50 and 2.50 also showed similar wave interactions.

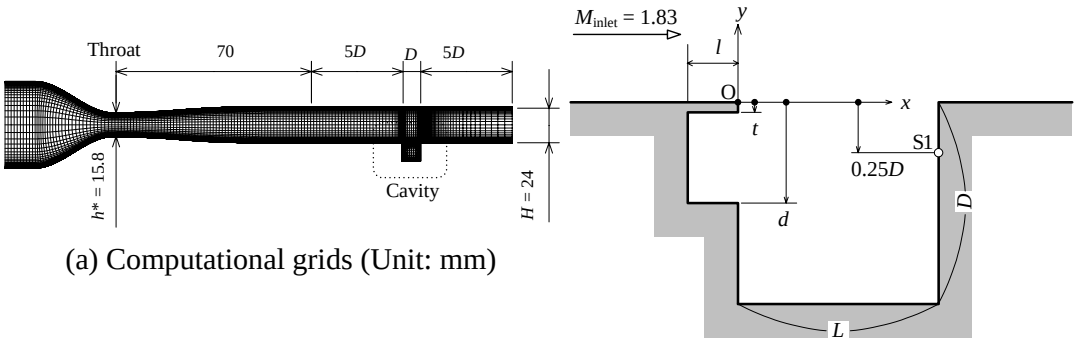

(a) Computational grids (Unit: mm)

(b) Details of cavity configuration

Fig.1 Computational domain

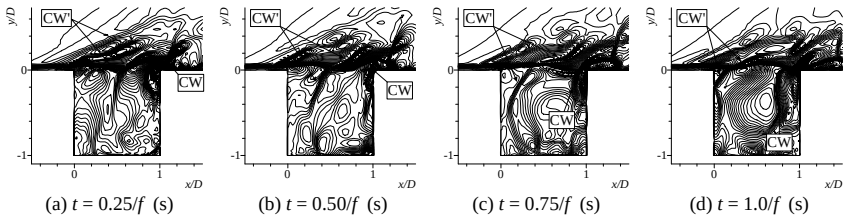

(a) $t = 0.25/f$ (s) (b) $t = 0.50/f$ (s) (c) $t = 0.75/f$ (s) (d) $t = 1.0/f$ (s)

Fig.2 Contour maps of density without control at Mach 1.83

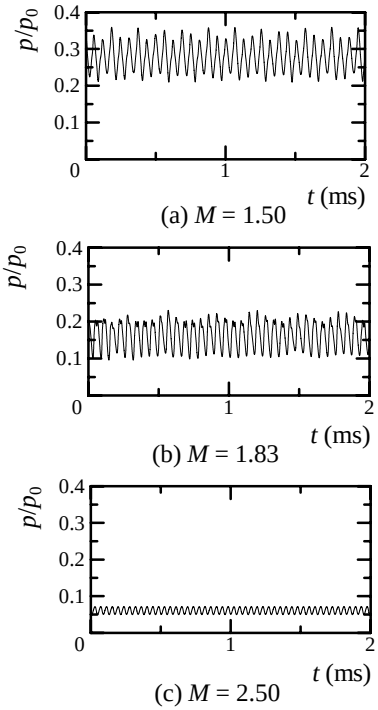

Fig.3 Time histories of static pressure without control

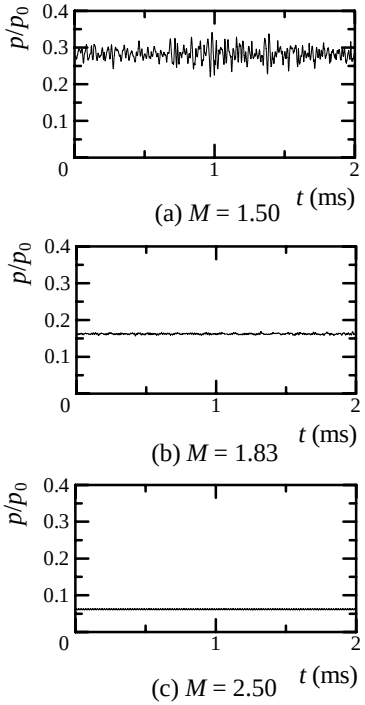

Fig.4 Time histories of static pressure with control

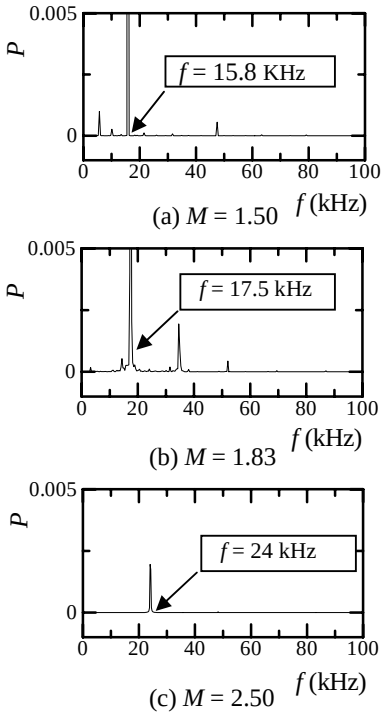

Fig.5 Distributions of power spectrum density without control

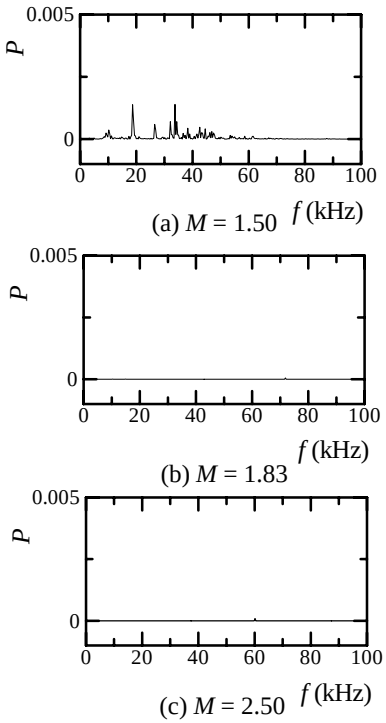

Fig.6 Distributions of power spectrum density with control

3.2 Effect of Leading Edge Plate on the Cavity Flowfield

Figures 3, 4 show the time histories of static pressure at the position S1 inside the cavity

with and without control at inlet Mach number 1.50, 1.83 and 2.50 at the cavity entrance. There exist large amplitudes of oscillations at this position of without control as shown in Fig.3. On the other hand, a substantial reduction of the amplitudes are obtained at different inlet Mach number when a flat plate is introduced in the cavity (when l/D = -0.25, t/D = 0.05 and d/D = 0.75) as in Fig.4. Distributions of power spectrum density at different inlet Mach number at the same position are shown in Fig.5. There are dominant frequencies at 15.8 kH, 17.5 kHz and 24 kH in case of cavity without control at Mach 1.50, 1.83 and 2.50, respectively (Fig.5), where as there are almost no peak frequencies for cases with control at Mach number 1.83 and 2.50 as shown in Fig.6(b) and Fig.6(c) (when l/D = -0.25, t/D = 0.05 and d/D = 0.75). In case of Mach number 1.50 at the cavity entrance there is a weak peak frequency for case with control (see Fig.6(a). The formation of feedback loops and consequently the occurrence of resonance are considered to be the reason of intense pressure oscillations observed in the cavity without control as shown in Figs.3, 5. The significant reductions of oscillations (Figs.4, 6) are due to the fact that the upstream compression waves that impinge on the front wall and below the flat plate cannot disturb the shear layer immediately after the reflection. The reflected waves which are now below the flat plate and traveling downstream become weaker gradually as they travel and will be dissipated.

3.3 Effect of Length of the Plate

To determine the effect of length of the leading edge plate on the cavity-induced pressure oscillations, observations were also made on the cavity with l/D = 0, -0.125, -0.1875 and -0.25. The most reduction of oscillations was obtained with l/D = -0.25 [7].

3.4 Sub-Cavity as an Oscillation Suppressor

Figure 7 shows the time histories of static pressure at the position S1 on the trailing edge of the cavity of l/D = -0.25, t/D = 0.05 with the variation of the depth d of sub-cavity at the front wall at inlet Mach number 1.83. As seen from Figs. 7(a)~7(e), amplitudes of oscillations are larger than those in Figs.7(f) and 7(g). Distributions of power spectrum density also showed that there was no peak frequency at a relatively higher depth of sub-cavity and there were some peak frequencies at a relatively smaller depth of sub-cavity. A sub-cavity acts as an additional cavity with L/d>2 for the case shown in Figs.7(a)~7(e). In addition to the reflections of upcoming compression waves on the front wall, reflections will also be occurred at the bottom face of the upper cavity. Those secondary reflections will reach the shear layer to excite it. However, increasing the depth of sub-cavity will reduce the aspect ratio of the upper cavity and the possibility of disturbances of shear layer by the secondary reflections will be reduced [12].

Figure 8 shows typical density contours for the cavity without control at Mach 1.83. There exist no upstream compression waves or the reflected waves as shown in Figs. 8(a) through 8(d). Consequently, there exists a stable shear layer in the cavity with control.

Figure 9 shows the streamlines of flowfield with control (l/D = -0.25, t/D = 0.05, d/D = 0.75 and M = 1.83). Figure 9 shows that in the sub-cavity there is developing another large vortex which is obstructed by the leading edge plate. Therefore, shedding of small vortices is discouraged here in the cavity with control and there exists a stable shear layer.

3.5 Effect of Mach Number

Figure 3 shows the time histories of static pressure at the position S1 on the trailing edge of the cavity without control at inlet Mach number 1.50, 1.83 and 2.50 at the cavity entrance.

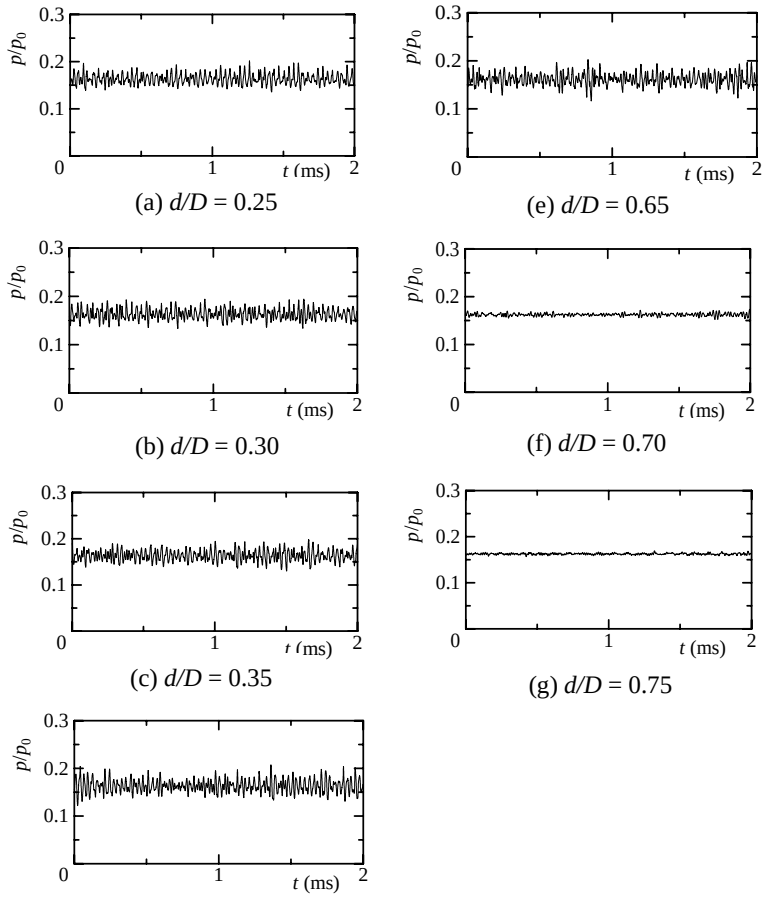

Fig.7 Time histories of static pressure at S1 (*l*/*D* = -0.25, *t*/*D* = 0.05, *M* = 1.83)

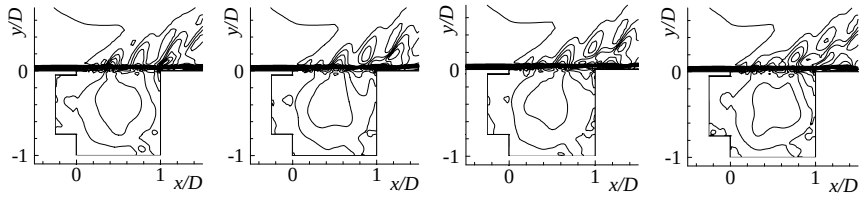

Fig.8 Contour maps of density with control at Mach 1.83

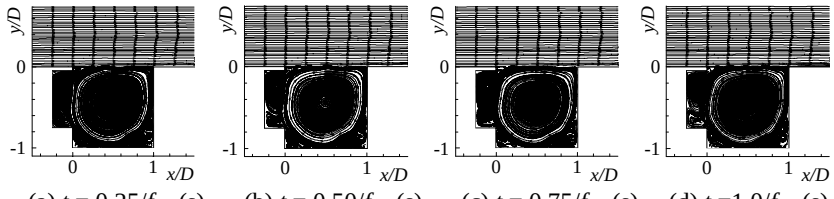

Fig.9 Streamlines with control at Mach 1.83

Amplitudes of oscillations of static pressure variation are high in all the cases of different inlet Mach number without control and the magnitudes of mean static pressure vary with the variation of inlet Mach number. On the other hand, amplitudes of oscillations are reduced

with the application of control device (Sub-Cavity) in all the cases of different inlet Mach number as shown in Fig. 4.

Figure 5 shows the distributions of power spectrum density without control at Mach number 1.50, 1.83 and 2.50 at the cavity entrance. There are dominant peak frequencies in all the cases of different inlet Mach number as shown in Figs.5(a) though 5(c). It also shows that oscillation frequency varies with the variation of inlet Mach number. There is no peak frequency for cases with control at Mach number 1.83 and 2.50 as shown in Figs.6(b), 6(c). However, there is small peak at Mach number 1.5 as shown in Fig. 6(a).

4. CONCLUSION

In order to investigate the effectiveness of controlling the cavity-induced pressure oscillations in two-dimensional flow, a computational study has been carried out for supersonic cavities with a sub-cavity at Mach number 1.50, 1.83 and 2.50 at the cavity entrance. The results showed that the sub-cavity attached near the front wall of a square cavity was very effective at a wide range of inlet Mach number in reducing cavity-induced pressure oscillations. Furthermore, the reduction of pressure oscillations was dependent on the inlet Mach number, length and depth of the sub-cavity used as oscillation suppressors. Therefore, the proposed control device could be a suitable tool in reducing cavity-induced pressure oscillations in a changing flow conditions.

REFERENCES

[1] Krishnamurty, K., Acoustic Radiation from two Dimensional Rectangular Cutouts in Aerodynamic Surfaces, NACA TN-3487, August 1955.

[2] Roshko, A., Some Measurements of Flow in a Rectangular Cutout, NACA TN-3488, 1955.

[3] Rossiter, J. E., Wind-tunnel Experiments on the Flow over Rectangular Cavities at Subsonic and Transonic Speeds, Aeronautical Research Council RM-3438, 1964.

[4] Heller, H. H., Bliss, D. B., The Physical Mechanism of Flow-Induced Pressure Fluctuations in Cavities and Concepts for their Suppression, AIAA Paper 75-491, 1975.

[5] Shaw, L., Clark, R., Talmadge, D., F-111 Generic Weapons Bay Acoustic Environment, *Journal of Aircraft*, 25 (1988), 2, pp. 147-153.

[6] Sarno, R., Franke, M., Suppression of Flow-induced Pressure Oscillations in Cavities, *Journal of Aircraft*, 31 (1994), 1, pp. 90-96.

[7] Alam, M. M., Matsuo, S., Teramoto, K., Setoguchi, T. and Kim, H. D., A New Method of Controlling Cavity-Induced Pressure Oscillations Using Sub-Cavity, Proceedings, 5th Asian-Pacific Conference on Aerospace Technology and Science, Guilin, China, 2006, CD-ROM.

[8] Goldberg, U. C., Toward a Pointwise Turbulence Model for Wall-bounded and Free Shear Flows, *Trans ASME, Journal of Fluids Engineering*, 116 (1994), pp. 72-76.

[9] Goldberg, U. C., Exploring a Three-equation *R-k-*ε Turbulence Model, *Trans ASME, Journal of Fluids Engineering*, 118 (1996), pp. 795-799.

[10] Heiler, M., Instationäre Phänomene in Homogen/heterogen Kondensierenden Düsen- und Turbinenströmungen, Dissertation, Fakultät für Maschinenbau, Universität Karlsruhe, Germany, 1999.

[11] Yee, H. C., A Class of High-resolution Explicit and Implicit Shock Capturing Methods, NASA TM-89464, 1989.

[12] Tam, C.K.W., Block, P.J.W., On the Tones and Pressure Oscillations Induced by Flow over Rectangular Cavities, *Journal of Fluid Mechanics*, 89 (1978).

Proceedings of the 4th BSME-ASME International Conference on Thermal Engineering
27 -29 December 2008, Dhaka, Bangladesh

EFFECT OF MOISTURE ON SUPERSONIC IMPINGING JET FLOWS

Miah Md. Ashraful Alam[1], Shigeru Matsuo[2], Md. Mamun[3], Toshiaki Setoguchi[2] and Heuy Dong Kim[4]

[1]Graduate School of Science and Engineering, Saga University, 1 Honjo, Saga 840-8502, Japan.
[2]Department of Mechanical Engineering, Saga University, 1 Honjo, Saga 840-8502, Japan.
[3]Department of Mech. Engineering, Bangladesh University of Engineering & Technology, Dhaka-1000, Bangladesh.
(Email: mamun@me.buet.ac.bd)
[4] School of Mechanical Engineering, Andong National University, Andong 760-749, Korea

ABSTRACT

Supersonic impinging jets produce a highly unsteady flowfield leading to a very noisy environment with very high dynamic pressure loads on nearby surfaces. Such undesirable phenomena are occurring in many aerodynamic applications, like in the space launch vehicle systems, multi-stage rocket separation, jet-engine exhaust impingement, terrestrial rocket launch, and in short take off and vertical landing (STOL) aircraft. Previous studies suggest that the highly unsteady behavior of the impinging jets is due to a feedback loop between the fluid and acoustic fields leads to these adverse effects. In actual supersonic jet flow, usually the working gas may be condensable gas such as steam or moist air. In these cases, the non-equilibrium condensation may occur in the region between nozzle exit and an object. The jet flow with non-equilibrium condensation may be quite different from that without condensation. In the present study, characteristics of under-expanded axisymmetric supersonic impinging moist air jets on a vertical flat plate were investigated numerically.

Keywords: *compressible flow, impinging, non-equilibrium condensation, oscillation*

1. INTRODUCTION

The impingement of supersonic jets, on solid boundaries, generally results in an extremely unsteady flowfield accompanied by a host of undesirable aeroacoustic properties. These include, but are not limited to, very high ambient noise levels dominated by discrete frequency tones – referred to as impingement tones – and the high speed and temperature leads to a severe mechanical and thermal loading on the impinging plate. These impingement tones may cause sonic fatigue of the structures and also may damage various instruments and equipments.

Unfortunately, supersonic impinging jets are ubiquitously present in a wide variety of situations, such as in space launch vehicle systems, supersonic short take-off and landing (STOL) aircraft [1], multi-stage rocket separation, jet-engine exhaust impingement, terrestrial rocket launch, and so on. Despite the simple geometry, the flow structure of supersonic impinging jet onto a flat plate is rather complex; it contains mixed supersonic and subsonic regions, involves interaction of shock and expansion waves with jet shear layers [2], [3], and becomes oscillatory under certain operating conditions after the initial transient impinging behavior. The unsteady oscillatory nature is caused by the feedback loop of the downstream travelling vortical structures and the upstream propagating acoustic waves [4]-[6]. This unsteady oscillation can make thermal and mechanical loading more severe.

In the above mentioned applications, usually the working gas is steam or moist air which have not yet received the same level of attention in supersonic jet technologies as single-phase gases. In these cases, non-equilibrium condensation [7], [8] may occur in the region between nozzle exit and an object, and the surrounding gas will be heated by the release of latent heat of condensation. The wave structure of supersonic impinging moist air jets may be quite different from that of dry air. Therefore, it requires performing more investigation on the oscillatory behavior and wave structure of supersonic impinging moist air jets.

In this paper, we focus on the surface pressure oscillations and the structural changes of oscillatory flow to the dynamic characteristic of supersonic impinging jets issuing from a converging nozzle at moderate nozzle pressure ratio numerically and these results are compared with experimental ones. Furthermore, the effect of non-equilibrium condensation of moist air on the jet flow structure and acoustic waves is investigated for three kinds of nozzle-to-plate distances.

2. NUMERICAL APPROACHES

Assumptions using in the present calculation of the two phase supersonic jet flow are as follows; Both velocity slip and temperature difference do not exist between condensate particles and gas mixture, and the effect of the condensate particles on pressure is neglected. The governing equations i.e., the unsteady compressible Navier-Stokes equations coupled with turbulence kinetic energy, eddy viscosity equations and droplet growth equation [9] are non-dimensionalized with reference values at the inlet conditions upstream of the nozzle can be written in an axisymmetric coordinate system. To close the governing equations, Goldberg's modified two-equation *k-R* turbulence model [10]-[12] is employed in computations. A third-order TVD (Total Variation Diminishing) finite difference scheme with MUSCL approach [13] was used to discretize the spatial derivatives, a second order-central difference scheme for the viscous terms, and a second-order fractional step was employed for time integration.

3. COMPUTATIONAL CONDITIONS

Figure 1 shows computational domain and boundary conditions. The sonic nozzle [14] with a circular arc of R=12.7 mm has a diameter of ϕD=12.7 mm (characteristic length) at the exit. The distances from the nozzle exit to impinging plate L are 25.4 mm (L/D=2.0), 38.1 mm (L/D=3.0) and 50.8 mm (L/D=4.0). The number of grids (Δx=0.005D, Δy=0.00035D) is 70×60 in the nozzle region and 165×131 in the jet plume and impingement region. In the present study, the nozzle pressure ratio which means the ratio of the reservoir pressure p_0 (atmospheric pressure) to back pressure p_b (= p_0/p_b) is fixed at 3.0. Values of the initial degree of supersaturation, S_0 are 0 (dry air), 0.4 (moist air) and 0.8 (moist air). Total temperature T_0 and total pressure p_0 in the reservoir are 298.15 K and 101.3 kPa, respectively.

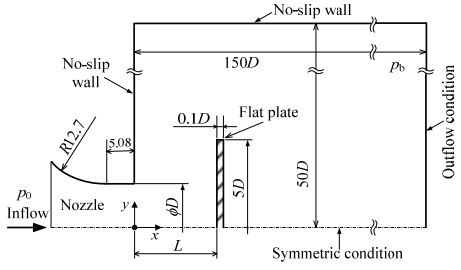

Fig.1 Computational domain and boundary conditions

Table 1 Dominant frequency of the pressure oscillations (kHz)

	Nozzle to plate distance ratio (L/D)		
	2.0	2.5	3.0
Numerical	12.5	17.61	15.06
Experimental	11.41	17.21	14.61

At the inflow boundary upstream of the nozzle, all variables were fixed at the initial values and all variables are extrapolated at the outflow boundary downstream of nozzle. The non-slip wall condition was used on the solid surface. The Axisymmetric condition was used at the boundary of the nozzle centre line. Iso-pressure and no heat transfer were constrained on the solid wall. Condensate mass fraction was set at $g = 0$ on the wall.

4. RESULTS AND DISCUSSION

4.1 Comparison with experimental results

Experiments were conducted to validate the present computational work. Dominant frequency of the pressure oscillations obtained from computations and experiments at the plate center (y/D=0) is shown in Table 1 for three kinds of nozzle-to-plate distance ratios (L/D). As seen from the table, the frequencies of the surface pressure oscillation in the present computation are in a good agreement with the impinging tones of the present experimental measurements.

4.2 Simulation of jet structure

To characterize the oscillatory behavior of the flow, power spectra of the static pressures have been calculated. Figure 2 shows time histories of static pressure and distributions of power spectrum density at the center of the plate for L/D=2.0 and 4.0 (S_0=0). As is evident from Figs.2(b) and 2(d), peak values are observed in each case.

Figures 3(a) and 4(a) show variations of static pressure distributions along the jet centerline during one period of flowfield oscillations for cases of L/D=2.0 and 4.0, respectively (S_0=0). It is found from these figures that the pressure distribution of the expansion region in the first cell from the nozzle, characterized by a monotonic decrease, does not vary with time for these cases. However, the pressure distribution over the compression region in and after the first cell changes with time. In Fig.3(a), t=0.25T (T : periodic time of

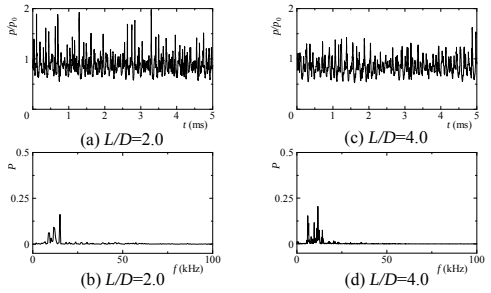

Fig.2 Time history of static pressure (a,c), and distributions of power spectrum density(b,d) (y/D=0, S_0=0)

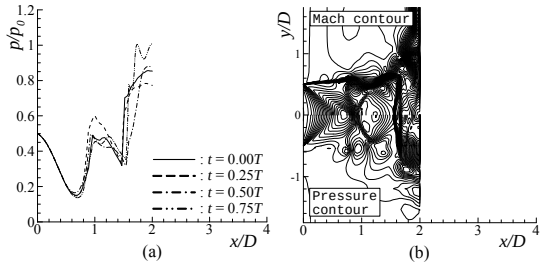

Fig.3 Variations of pressure distributions along the jet axis (a), and Instantaneous flowfields at t =0.75T(s) (b) (L/D=2.0, S_0=0)

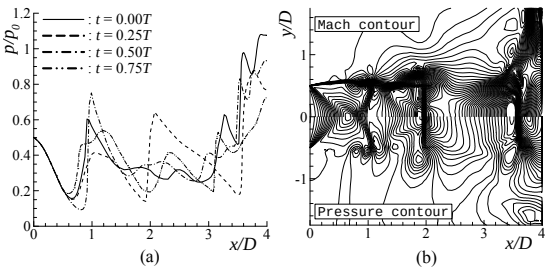

Fig.4 Variations of pressure distribution along the jet axis (a), and Instantaneous flowfields at t =0.25T(s) (b) (L/D=4.0, S_0=0)

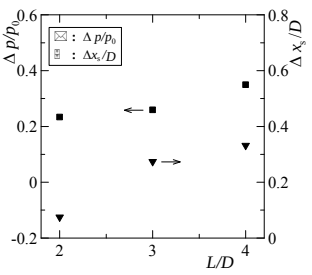

Fig.5 Amplitudes of the surface pressure and the plate shock oscillations (p_0/p_b=3.0, S_0=0)

oscillation) refers to the instant when the pressure behind the first compression shock (near x/D=1.0) becomes the largest, and at instant t=0.75T behind the first compression region, the pressure distribution becomes the smallest. This suggests that the shock cell structures change continuously during the cycle of oscillation.

Figures 3(b) and 4(b) illustrate instantaneous flowfields (Mach number and pressure contours) corresponding to t=0.75T and t=0.25T, respectively. When L/D is small, the plate shock is located behind the second expansion region. A 'double shock' structure is seen during the oscillation as shown in Fig.3(a). As L/D increases beyond 3.0, the third and sometimes fourth expansion regions appear. The compression in these cases may involve two normal shocks as seen in Fig. 4(b).

Figure 5 shows amplitudes of the surface pressure Δp and variations of the plate shock position Δx_s for L/D=2.0, 3.0 & 4.0. The amplitude denotes the difference between the maximum and the minimum pressure during one cycle of flowfield oscillation at the center (y/D=0) of impinging plate. The plate shock position x_s is measured from the impinging plate to the plate shock. Furthermore, as seen from Figs. 3(b) and 4(b), the flow field between an oscillatory plate shock wave and the vertical plate has very complicated structure. The interaction between a jet boundary with high vorticity fluid and an oblique shock wave seems to have strong effects on the flow field.

4.3 Effect of non-equilibrium condensation

Figures 6 and 7 show time histories of static pressure and distributions of power spectrum density at the center (y/D=0) of impinging plate for the cases of L/D=2.0 and 4.0, respectively (S_0=0.4 and 0.8). For both cases of L/D=2.0 and 4.0, amplitudes of static pressure for S_0=0.4 and 0.8 (Figs.6(a,c) and 7(a,c)) become small compared with those of S_0=0 and peaks of the power spectrum density are reduced in case with non-equilibrium condensation (in Figs.6(b,d) and 7(b,d)). Furthermore, in both cases (L/D=2.0 and 4.0), the amplitude of static pressure and peaks of the power spectrum density for S_0=0.8 are reduced more compared with the case of S_0=0.4. This means that energy of turbulent fluctuations is reduced due to relaxation processes of evaporation and condensation of vapor molecules on small droplet surface [15]. Therefore, this shows that the occurrence of non-equilibrium condensation is enable one to reduce the noise level of supersonic impinging jets.

In case of L/D=3.0, the amplitude of pressure oscillations and the peak of power spectrum was also reduced in cases with non-equilibrium condensation (S_0=0.4 and 0.8).

Figures 8 and 10 show variations of distribution of static pressure p, condensate mass fraction g and nucleation rate I on the jet axis during one period of oscillation for L/D=2.0 (S_0=0.4) and L/D=4.0 (S_0=0.8), respectively. As seen from Figs.8(a) and 10(a), the amplitudes of static pressure oscillations become smaller compared to that of without the non-equilibrium condensation (Figs. 3(a) and 4(a)). From Figs.8(c) and 10(c), the nucleation rate begins to

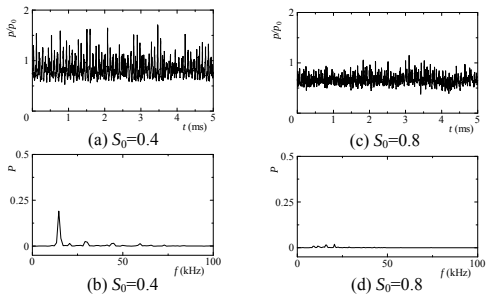

Fig.6 Time history of static pressure (a,c), and distribution of power spectrum density (b,d) (L/D=2.0, y/D=0)

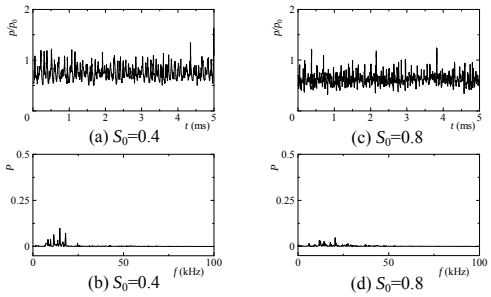

Fig.7 Time history of static pressure (a,c), and distribution of power spectrum density (b,d) (L/D=4.0, y/D=0)

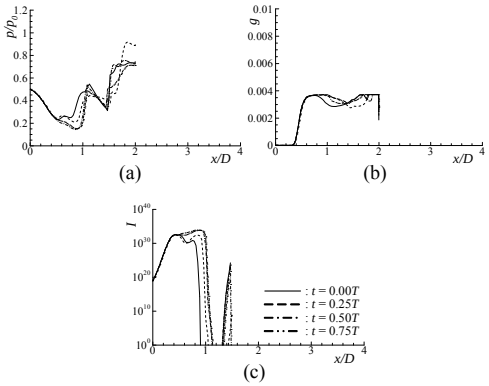

Fig.8 Variations of distribution of static pressure (a), condensate mass fraction (b), and nucleation rate (c) along the jet axis (*L/D*=2.0, S_0=0.4)

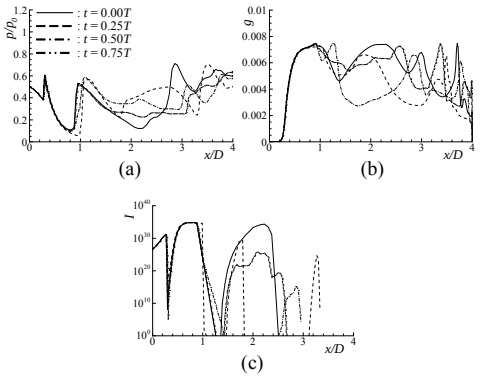

Fig.10 Variations of distribution of static pressure (a), condensate mass fraction (b), and nucleation rate (c) along the jet axis (*L/D*=4.0, S_0=0.8)

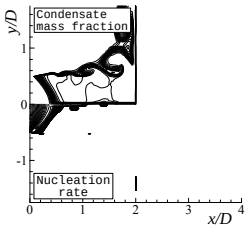

Fig.9 Instantaneous flowfields corresponds to instant *t*=0.75*T*(s) (*L/D*=2.0, S_0=0.4)

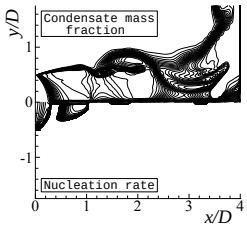

Fig.11 Instantaneous flowfields corresponds to instant *t*=0.25*T*(s) (*L/D*=4.0, S_0=0.8)

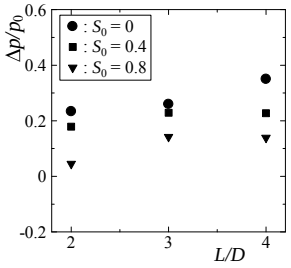

Fig.12 Effect of condensation on the amplitude of the surface pressure, p_0/p_b=3.0

increase from upstream of the nozzle exit and reaches the maximum at onset of condensation. Moreover, the condensate mass fraction begins to increase at the onset of condensation as shown in Figs.8(b) and 10(b). For cases of *L/D*=2.0, S_0=0.8 and *L/D*=4.0, S_0=0.4, the variation of static pressure, condensate mass fraction and nucleation rate were almost similar to those in case of *L/D*=2.0, S_0=0.4 (Fig.8) and *L/D*=4.0, S_0=0.8 (Fig.10). In both cases of *L/D*=2.0 and 4.0, the amplitude of static pressure oscillation for S_0=0.8 are reduced compared to that of case for S_0=0.4.

Figures 9 and 11 show instantaneous contour maps of nucleation rate and condensate mass fraction in cases of *L/D*=2.0 (S_0=0.4) and *L/D*=4.0 (S_0=0.8), respectively. Condensate nuclei begin to generate from the region upstream of the nozzle exit. The condensate mass fraction begins to increase rapidly in expansion fan and jet boundary. In the flow field of *L/D*=3.0, S_0=0.4 and 0.8, variations of distribution of static pressure, condensate mass fraction and nucleation rate during one cycle of flow field oscillation have almost similar tendency to those for *L/D*= 2.0.

Figure 12 shows the effect of non-equilibrium condensation on the amplitude of surface pressure oscillation. The amplitude denotes the difference between the maximum and the minimum pressure during one cycle of flowfield oscillation at the center (*y/D*=0) of impinging plate. From this figure, in all cases of *L/D*=2.0, 3.0 & 4.0, the occurrence of non-equilibrium condensation reduces the amplitude of surface pressure oscillations in cases of S_0=0.4 and S_0=0.8.

5. CONCLUSION

In the present study, the axisymmetric unsteady Navier-Stokes system was used to investigate the oscillatory features of surface pressure and the structural change of the supersonic under-expanded moist air jet impinging on a flat plate with three kinds of the nozzle-to-plate distance ratio. Furthermore, the numerical results were compared with experimental results. The results obtained are summarized as follows: in the case with non-equilibrium condensation, the amplitude of surface pressure oscillation become small compared with those of dry air, and peaks of the power spectrum density are reduced in case with non-equilibrium condensation.

REFERENCES

[1] Petrie, A.M., An experimental investigation of jet screech by air jet impingement on solid boundaries, *Applied Scientific Research*, Vol.36, pp.93-108, (1980).

[2] Lamont, P.J., Hunt, B.L., The impingement of underexpanded, Axisymmetric jets on perpendicular and inclined flat plates, *Journal of Fluid Mechanics*, Vol.100, part 3, pp. 471-511,(1980).

[3] Kim, S.I., Park, S.O., Oscillatory behavior of supersonic impinging jet flows, *Shock Waves*, Vol.14, part 4, pp.259–272, (2005).

[4] Krothapalli, A., Discrete tones generated by an impinging underexpanded rectangular jet, *AIAA Journal*, Vol.23, pp.1910-1915, (1985).

[5] Powell, A., The sound-producing oscillations of round underexpanded jets impinging on normal plates, *J. Acoust. Soc. Am.*, Vol.83, pp.515-533, (1988).

[6] Tam, C.K.W., Ahuja, K.K., Theoretical model of discrete tone generation by impinging jets, *J. Fluid Mechanics*, Vol.214, pp.67-87, (1990).

[7] Wegener, P. P., Mack, L. M., Condensation in supersonic hypersonic wind tunnels, *Adv. In Appl. Mech.*, 5, Academic Press, (1958).

[8] Matsuo, K., Kawagoe, S., Sonoda, K., Sakao, K., Studies of Condensation Shock Waves (part 1, Mechanism of their Formation), *Bulletin of JSME*, Vol.28, pp.2577-2582, (1985).

[9] Sislian, J. P., Condensation of Water Vapor with or without a Carrier Gas in a Shock Tube, UTIAS Report, No. 201, (1975).

[10] Goldberg, U. C., Toward a Pointwise Turbulence Model for Wall-Bounded and Free Shear Flows, *Transactions of the ASME*, Vol.116, pp.72-76, (1994).

[11] Goldberg, U. C., Exploring a Three-Equation R-k-ε Turbulence Model, *J. Fluids Engg.*, Vol.118, pp.795-799, (1996).

[12] Heiler, M., Instationäre Phänomene in Homogen/Heterogen Kondensierenden Düsen- und Turbinenströmungen, Dissertation, Fakultät für Maschinenbau, Universität Karlsruhe (TH), Germany, (1999).

[13] Yee, H. C., A class of high-resolution explicit and implicit shock capturing methods, NASA TM-89464, (1989).

[14] Addy, A.L., Effects of Axisymmetric Sonic Nozzle Geometry on Mach Disk Characteristics, *AIAA Journal*, Vol.19, No.1, pp.121-122, (1981).

[15] Hiller, W.J., Jaeschke, M., Meier, G.E.A., The influence of Air Humidity on Pressure and Density Fluctuations in Transonic Jets, *J. Sound Vib.*, Vol.17, No.3, pp.423-428, (1971).

Proceedings of the 4th BSME-ASME International Conference on Thermal Engineering
27-29 December, 2008, Dhaka, Bangladesh

EFFECT OF PRESSURE AND COLD FRACTION ON THE PERFORMANCE OF VORTEX TUBE

Jaykumar D.Golhar[1], A.N.Pawar[2], R.B.Tirpude[3]

[1] Department of Mechanical Engineering, Government Polytechnic Sakoli , Dist. Bhandara , Maharashtra-441802 , India.

e-mail jaykumar_golhar@rediffmail.com

[2] Department of Mechanical Engineering, Government Polytechnic Yavatmal , Maharashtra-445001 , India

[3] Department of Mechanical Engineering, Government Polytechnic Ahmadnagar , Maharashtra, India

ABSRACT

This paper focuses on the experimental study on the effect of pressure and cold fraction on the performance of vortex tube. The vortex tube is a simple mechanical device without moving parts operating as a refrigerating machine. Compressed air supplied to the vortex tube is separated into low pressure hot and cold air from its two ends. The exact mechanism of this separation of air into hot and cold stream is not known today. Most of the investigators have studied the various operating characteristics of vortex tube based on the cold air fraction. Vortex tubes of different geometrical configurations give optimum performance at different cold fractions. The present paper explains the effect of inlet air pressure and cold fraction with the help of performance characteristics for vortex tubes of fixed geometrical configurations. This can help to optimize the vortex tube.

KEYWORDS: *Cold fraction, Energy separation, geometrical configurations.*

1. INTRODUCTION

A vortex refrigerator is a device with no moving parts (specifically, a tube or pipe) that will convert an incoming compressed fluid stream (such as air) of homogeneous temperature into two streams of different temperature, one warmer than the inlet and one cooler. Figure 1 shows the line diagram of a vortex tube. By injecting compressed air at room temperature circumferentially into a tube at high velocity, a vortex tube can produce cold air and hot air streams. The resulting vortex spins annularly along the tube inner walls as it moves axially down the tube. Part of the air is adiabatically expanded inward to the centre. The decrease in pressure during expansion causes a decrease in temperature, which provides a cooler centre column of air. The cold air typically is directed out one end (the cold end) of the tube, and the warm air at the periphery is exhausted out of the other end (the warm end). Temperature and airflow rates are controllable by adjusting valve on hot end of the tube. The inlet air is injected circumferentially at one end of the tube and part of the air is removed at the opposite end. As the flow moves toward the warm end, some of the air expands to the central core and exits at the cold end.

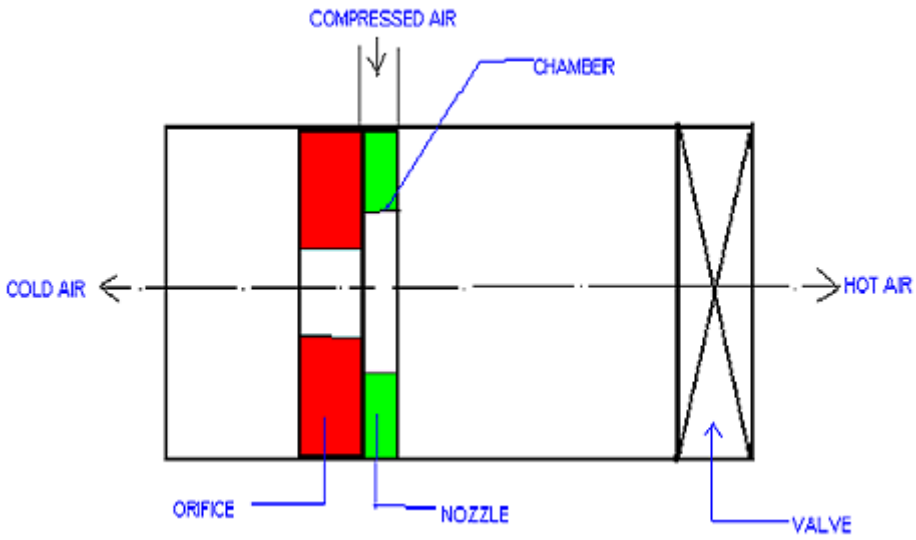

Fig. 1 Line Diagram of Vortex Tube

Vortex tubes are used commonly for industrial purposes to cool machinery during operation (e.g. mould tools, sewing needles, and soldering), to cool workers, to test thermostats, etc. They are popular for their reliability (no moving parts), lack of maintenance, and simple and inexpensive construction.

The stream of air leaving through the hot end and cold end of the vortex tube are at higher and lower total temperatures respectively than that of the air entering the nozzle. This separation of the flow into the regions of high and low total temperatures is referred to as temperature or energy separation effect.

This phenomenon of energy separation was first discovered by Ranque, a metallurgist, in 1931, when he was studying process in a dust separation cyclone. Later, Hilsch [1], a German physicist performed the detailed examination of the vortex effect and improved the design of vortex tube. Intensive experimental and analytical studies of vortex tube began since then and continue even today.

Many investigators like Hilsch [1], Fulton C.D. [2}, Deemter J.J. [3] have explained the basic analysis of vortex tube. Gulyave A.I. [4], Borisenko et al [5], Raiski et al [6], Takahama et al [7], Parulekar B.B. [8}, Lay J.E. [9], Webster D.S.[10], Y.Soni & W.J. Thomson [11] have done experimental studies on the vortex tube. Alhborn et al [12-14] has postulated a theory of temperature separation based on heat pump mechanism enabled by secondary circulation flow in vortex tube. M.H. Saidi and M.S.Valipour [15] performed experimental modeling of the vortex tube considering geometrical and thermo-physical parameters. Singh P.K and et al [16] states that the effect of nozzle design is more important than the cold orifice design in getting higher temperature drops.

However till today no exact theory has come up to explain the phenomenon satisfactorily. Thus much of the design and the development of vortex tube have been based on the empirical correlations leaving much scope for optimization of critical parameters.

Most of the investigators have considered cold fraction as a variable during their experimentation. Vortex tube of different geometrical configurations gives optimum performance at different cold fractions. Although cold fraction can be controlled by controlling the throttle valve opening, it is not the only parameter that affects cold fraction. It gets changed with the variation of inlet temperature (T_i) inlet pressure (P_i), orifice diameter

(D_o), Nozzle area (A), Tube diameter (D), Tube length (L) etc. It is very difficult to conduct experimentation at desired cold fraction because it is to be calculated from the data obtained during experimentation.

The present paper explains the effect of inlet air pressure (P_i) and cold fraction (μ) on cold temperature drop $(\Delta T)_c$ for vortex tube of fixed geometrical configuration.

2. EXPERIMENTAL SET-UP

The schematic representation of vortex tube setup used is shown in figure 2.

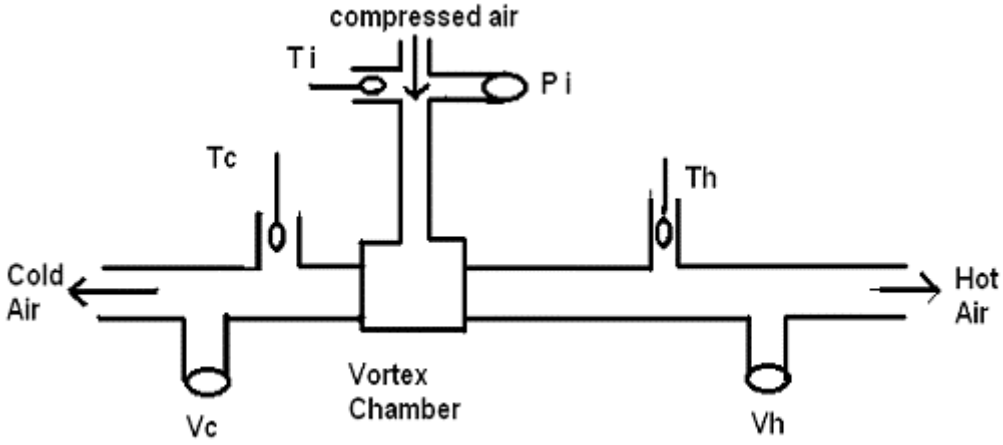

Fig. 2 Schematic Representation of Vortex Tube Setup

The pressure of the compressed inlet air is measured by pressure gauge attached to the inlet pipe very close to the nozzle. The inlet air temperature (T_i) , hot air temperature (T_h), cold air temperature (T_c) are measured by digital thermometers. Digital anemometers are used for measurement of cold air velocity (V_c) and hot air velocity (V_h). These velocities are in turn used for calculation of cold air mass flow rate (m_c) and hot air mass flow rate (m_h) respectively.

To investigate the effect of inlet air pressure and cold fraction on the operating characteristics of vortex tubes, vortex tube of following geometrical parameters was used.

Orifice diameter, D_o =4.76 mm

Nozzle diameter, D_n = 5.56 mm

Tube Diameter, D= 16.28 mm

Number of Nozzles, N= 4

3. EXPERIMENTAL RESULTS AND DISCUSSION

The effect of inlet pressure and cold fraction on the cold air temperature drop was investigated as shown in figure 3. It is observed that the cold temperature drop increases with increase of inlet pressure at lower range and decreases at higher inlet pressure. But for getting maximum temperature drop; cold fraction also increases with increase of pressure. Empirical

relation between maximum temperature drop $(\Delta Tc)_{max}$ and optimum cold fraction $(\mu)_{opt}$ is given by following expression:

$$(\Delta Tc)_{max} = 37.235 \ln (\mu)_{opt} + 52.751 \quad (1)$$

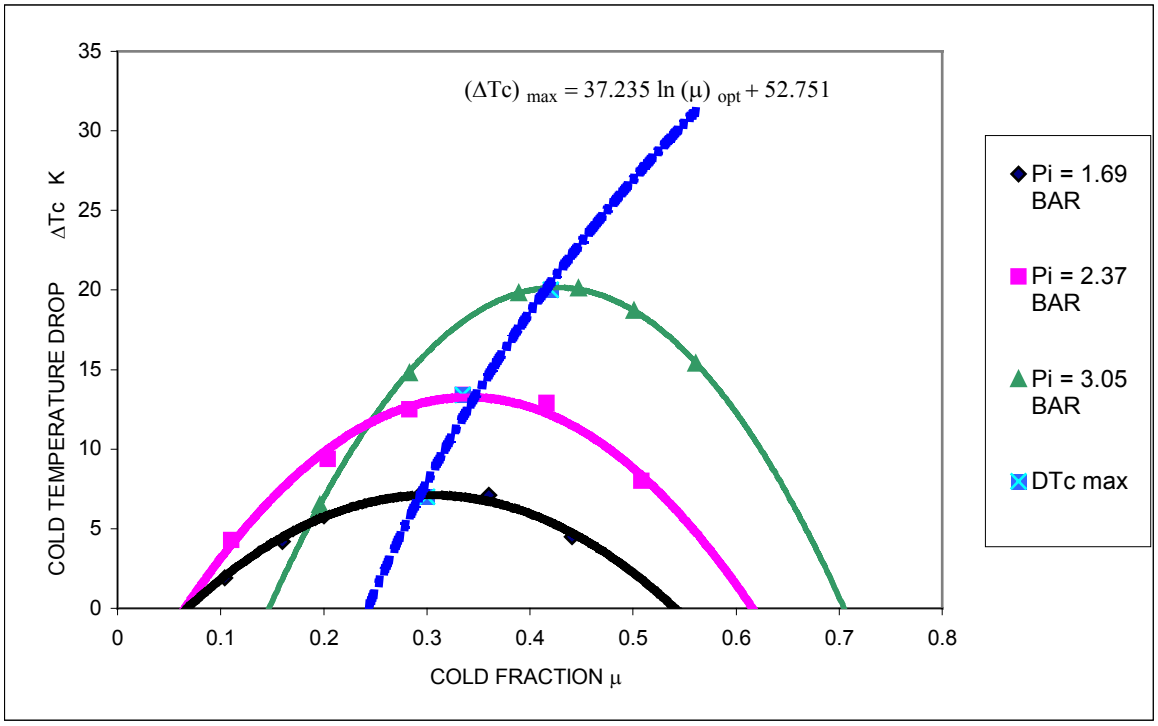

Figure 3(a)

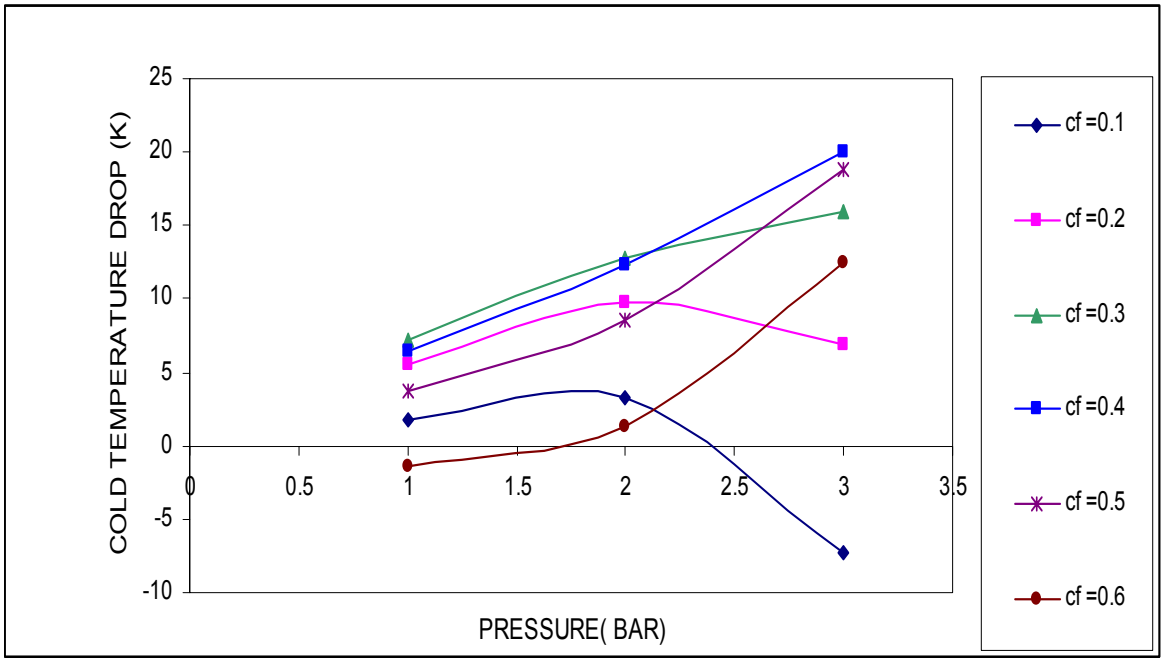

Figure 3 (b)

Fig. 3 Performance of Vortex Tube

Small cold fractions give cold temperature at moderate pressures only. At low and high values of inlet pressures, small cold fractions have possibility of reversing of temperature i.e. hot air is obtained at both ends of the vortex tube.

Large cold fractions give cold temperature at higher inlet pressures, but reversing of temperature may take place at lower inlet pressures.

Moderate cold fractions (0.3 to 0.4) give cold temperature drop for all ranges of pressures.

During this process two air streams move in counter flow direction. Air at the center transfers its energy to peripheral air. Due to this core air temperature normally decreases and peripheral air temperature normally increases. For this temperature change to occur mass flow rates of two air streams and time available for energy transfer plays important role.

At low pressure air velocity is less, hence more time is available for transfer of energy. Under very small cold fraction condition mass flow rate of core air is very small. Therefore at low pressure and small cold fraction energy transfer takes place from peripheral air to core air i.e. core air temperature also increases.

At high pressure air velocity is more, hence small time is available for transfer of energy. Therefore more core air is required for large energy transfer. Thus large cold fraction is required to achieve cold temperature at higher inlet pressures.

But under too large cold fraction conditions energy transferred to small quantity of peripheral air reduces. Hence cold temperature drop decreases after peak value of cold fraction. Thus moderate cold fractions give better performance for vortex tubes.

4. CONCLUSION

In this paper effect of inlet pressure on the performance characteristics of vortex tube are investigated at various cold fractions by experimental modeling of vortex tube. Vortex tube gives better performance for cold fraction around 0.3 to 0.4. Maximum cold temperature drop occurs at higher pressure and moderate cold fraction. At lower cold fraction hot air is obtained at both ends of the vortex tube.

5. REFERENCES

[1] R. Hilsch. ‘The use of the Expansion of air in a Centrifugal field as a cooling process.’ The Review of Scientific Instruments, vol 13, February 1947, pp 108-113.

[2] C.D. Fulton. ‘Ranque’s Tube.’ Journal Of ASRE, Refrigeration Engineering. Vol 59, May 1950, pp 473-479.

[3] J.J.Van Deemter : On the Theory of the RH Cooling Effect : Appl Sci Res Section A, Vol 3, pp 174-196

[4] A.I.Gulyaev. ‘Investigation of Conical vortex tubes.’ Journal of Engineering physics, vol 10, no 3, 1966, pp 326-336

[5] A.I. Borisenko, V.A. Safonov, and A.I. Yakovlev. 'The Effect of Geometrical Parameters on the Characteristic of a conical vortex cooling unit.' Journal of Engineering physics, vol 15, no 6, December 1968, pp 988-993.

[6] Y.D.Raiskii and L. E. Tunkel. 'Influence Of Vortex Tube Configuration And Length On The Process Of Energetic Air Separation.' Journal of Engineering physics, vol 27, no 6, December 1974, pp 1578-1581.

[7] H. Taakahama AND H. Yokosawa. 'Energy separation in vortex with a divergent chamber.' Transactions of ASME: Journal of Heat Transfer. vol 103, May 1981, pp 196-203

[8] B.B. Parulekar. 'The short vortex tube.' Journal of refrigeration Vol 4 ,July-August 1961, pp 74-80

[9] J.E.Lay - An experimental and analytical study of vortex flow temperature separation by superposition of spiral and axial flows part 1 & part 2. Transactions of ASME:Journal Of Heat Transfer. vol 81, no 3, August 1959, pp 202-222

[10] D.S. Webster. 'An Analysis of the Hilsch Vortex Tube' Journal Of ASRE, Refrigeration Engineering. Vol 58, February 1950, pp 163-171.

[11] Y.Soni & W.J. Thomson – Optimal design of Ranque-Hilsch tube. Transactions of ASME: Journal Of Heat Transfer.vol 94, no 2, May 1975. pp 316-317

[12] B.K. Ahlborn & J.M. Gordon : The Vortex Tube As a Classic Thermodynamic Refrigeration Cycle : Journal of Applied Physics, Vol 88 No. 6 Sept. 2000, pp 3645-3653

[13] B. Ahlborn,J. Camire & J.U. Keller : Low Pressure VT : Journal Physics D: Appl.Phys. 29 (1996) 1469-1472

[14] B.K. Ahlborn, J.U. Keller & E. Rebhan : The Heat Pump in a VT : J. Non Equilib. Thermodyn; 1998.Vol.23No.2.pp 159-165

[15] M.H. Saidi and M.S.Valipour: Experimental Modeling of the Vortex Tube Refrigerator: Applied Thermal Engineering 23(2003)1971-1980.

[16] Singh P.K, Tathgir R.G., Gangacharyulu D., Grewal G.S., Jan 2004, 'An Experimental Performance Evaluation of Vortex Tube' IE (I) Journal Vol. 84, p. 149-153

Proceedings of the 4th BSME-ASME International Conference on Thermal Engineering
27 -29 December 2008, Dhaka, Bangladesh

PASSIVE CONTROL OF PRESSURE LOADS IN SUPERSONIC CAVITIES AT VARIABLE MACH NUMBER

Md. Mahbubul Alam[1], Toshiaki Setoguchi[2], Shigeru Matsuo[2] and Heuy Dong Kim[3]

[1] Dept. of Mech. Eng., Chittagong University of Engineering and Technology, Chittagong-4349, Bangladesh.
[2]Department of Mechanical Engineering, Saga University, 1 Honjo-machi, Saga 840-8502, Japan.
[3]School of Mechanical Engineering, Andong National University, Andong 760-749, Korea
(Email: malam@cuet.ac.bd)

ABSTRACT

A computational study has been conducted to evaluate a porous wall on the control of pressure loads induced from supersonic cavities at Mach number 1.50, 1.83 and 2.50 at the cavity entrance. The introduction of these control devices helped to alter the behavior of oscillating shear layer in a favorable way so that high pressure loads induced from supersonic cavity were reduced remarkably. The results showed that the resultant amount of attenuation of pressure oscillations was dependent on the inlet Mach number, size of the perforations of the porous surface and also on the length of plate.

Key words: *Compressible flow, Supersonic cavity, Pressure oscillations, Passive control*

1. INTRODUCTION

The flows of air over an open cavity can generate intense pressure oscillations that represent an important issue to be solved because of its harmful effects in many aerodynamic applications [1-7]. A number of passive and active control devices have been investigated during the last three decades [4-7] to suppress the cavity-induced pressure oscillations. Heller and Bliss [4] studied several oscillations suppression devices such as slanting the trailing edge and reported that some of those devices were able to suppress the oscillations. Shaw et al. [5] conducted wind tunnel tests to assess the leading-edge sawtooth suppressors and the slanted trailing edges. He found that the slanted trailing edge was effective in attenuating cavity tones but the leading-edge spoilers were not fully successful. Jeng and Payne [6] conducted numerical experiments to study a passive control technique and found that the controlling was most effective when the rear wall of the cavity was replaced with a porous wall. Setoguchi et al. [7] studied a passive suppression technique at Mach number 1.83 and showed that a porous wall near the front wall of a cavity was very effective in reducing the oscillations. Although most of the methods mentioned here have been shown success in reducing the oscillations, their effectiveness should be investigated in an environment where the flow condition varies.

2. NUMERICAL METHOD

The governing equations are the unsteady compressible Navier-Stokes equations coupled with turbulence kinetic energy and eddy viscosity equations for modeling the turbulence [8-10]. A third-order TVD finite difference scheme with MUSCL [11] was used to discretize the spatial derivatives and a second order-central difference scheme for the viscous terms, and a second-order fractional step was employed for time integration.

3. NUMERICAL CONDITIONS

Figure 1 shows computational grids of a supersonic flow field with a cavity. The height of the main flow section at the entrance of the cavity H is 24 mm. The cavity depth D_1 is 12 mm and the length D_2 is 12 mm. S1 in this figure denotes the measuring position of static pressure. Control devices consist of a flat plate and a porous wall attached in the cavity as shown in the Fig. 1(b). Here porosity P is defined as the ratio of summation of the lengths of perforations (holes) in the porous wall to the total length of the wall. Porosity P is 0.5 in all the cases shown in Table 1. L denotes the length of the plate. T_1 and T_2 indicate the size of perforation and length between two consecutive perforations of the porous plate, respectively. The parameters of cavity configuration are summarized in Table 1. All simulations were tested for grid-spacing independence of the simulation result. Grid independence has been reached when the number of grids is 300×80 in the region of the nozzle and 50×60 in the cavity.

The origin in x-y coordinate is located at the cavity leading edge. Dry air is used as a working gas and assumed to be thermally and calorically perfect. Pressure p_0 in the reservoir is 101.3 kPa. The inlet Mach number M at the entrance of the cavity are 1.50, 1.83 and 2.50. On the solid walls, the no-slip conditions and no heat transfers were applied as the boundary conditions. Fixed conditions were set for the inflow boundary. Zero order extrapolation was used at the outflow boundary.

4. RESULTS AND DISCUSSION

4.1 **Effect of porous wall**

Figures 2, 3 show contour maps of density during one period of flow oscillation for the cavity without control at inlet Mach number 1.50 and 1.83 at the cavity entrance, respectively.

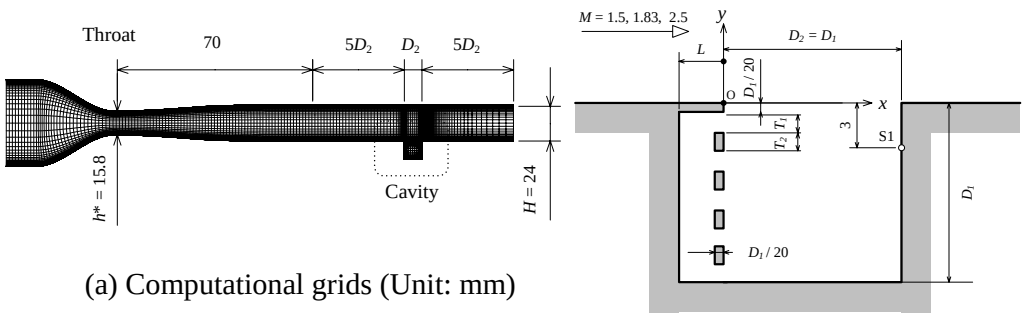

(a) Computational grids (Unit: mm)

(b) Details of cavity configuration

Fig.1 Computational domain

Table1 Parameters of cavity configuration

Parameters	T_1/D_1	T_2/D_1	L/D_1	P
Without control	0	1	0	0
Case 1	0.10	0.10	0.25	0.5
Case 2	0.10	0.10	0.15	0.5
Case 3	0.10	0.10	0.05	0.5
Case 4	0.05	0.05	0.25	0.5
Case 5	0.15	0.15	0.25	0.5

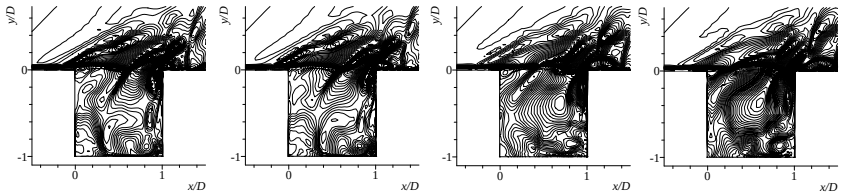

(a) $t = 0.25/f$ (s) (b) $t = 0.50/f$ (s) (c) $t = 0.75/f$ (s) (d) $t = 1.0/f$ (s)

Fig.2 Contour maps of density without control at Mach 1.50

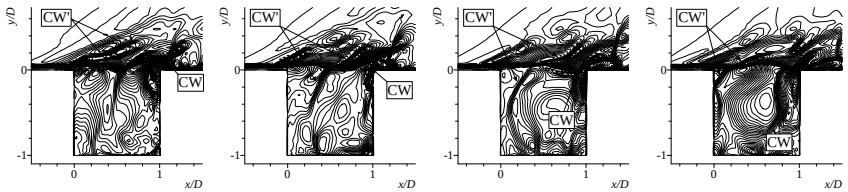

(a) $t = 0.25/f$ (s) (b) $t = 0.50/f$ (s) (c) $t = 0.75/f$ (s) (d) $t = 1.0/f$ (s)

Fig.3 Contour maps of density without control at Mach 1.83

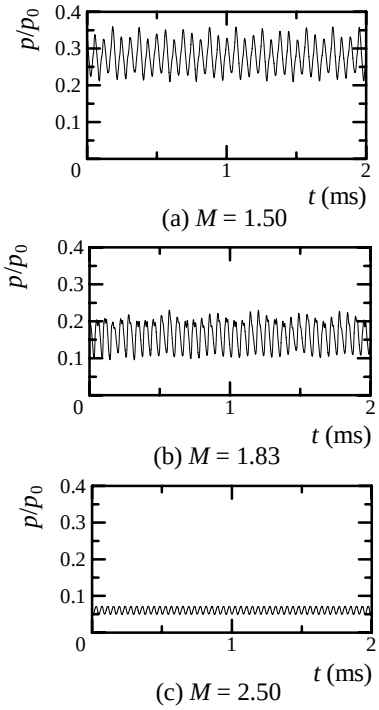

(a) $M = 1.50$ (b) $M = 1.83$ (c) $M = 2.50$

Fig.4 Time histories of static pressure without control

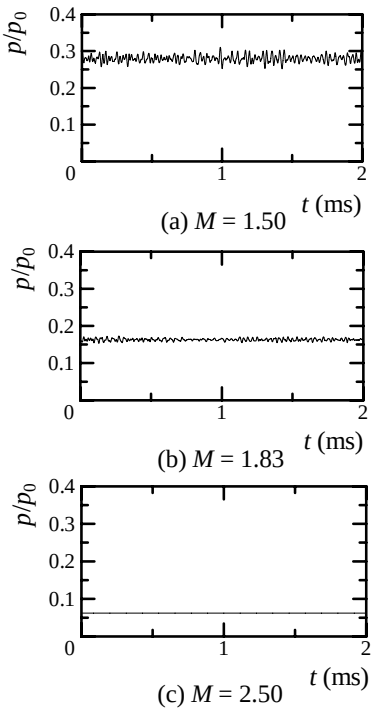

(a) $M = 1.50$ (b) $M = 1.83$ (c) $M = 2.50$

Fig.5 Time histories of static pressure with control

Here, f represents the dominant frequency, which is equal to 15.8 kHz, 17.5 kHz and 24 kHz (see Fig.6) for the inlet Mach number 1.50 and 1.83 and 2.50, respectively. It was observed that a compression wave (CW) from the trailing edge of the cavity moves upstream as time proceeds. The upstream compression waves impinge on the cavity leading edge (Fig.3(d)) and disturb the shear layer. This disturbance regenerates instability in the shear layer. While the shear layer reattaches at the rear wall of the cavity, generation of compression waves (CW) occurs due to the impingement of instability waves on the rear wall as shown in Fig.3(b) and thus completing the formation of feedback loop which is widely believed to be reason of cavity resonance.

There exist large amplitudes of oscillations at S1 as shown in Fig.4. Distributions of PSD (power spectrum density) at the same position obtained from the static pressure histories are

shown in Fig.6. There are dominant frequencies at 15.8 kHz, 17.5 kHz and 24 kHz in case of cavity without control at different inlet Mach number.

Figure 5 shows time histories of the static pressure at different inlet Mach number for Case 1 with control. Significant amount of reductions of the amplitudes of oscillations were obtained in the Case 1 as shown in Fig.5. Distributions of power spectrum density are shown in Fig.7. No peak frequency is found at inlet Mach number 1.50, 1.83 and 2.50.

The mechanism of controlling cavity pressure oscillations by these control devices can be explained in the following way. The upstream traveling compression waves inside the cavity will impinge on the porous wall and the reflection of compression waves will be occurred on the wall. However, the whole compression waves will not be reflected from the wall because of the porous wall. Some parts of the upstream compression waves that impinge on the solid portion of the porous wall will be reflected and will go downstream direction and some parts of the upstream compression waves will go further upstream direction through the perforated wall. This phenomenon of splitting the impinging compression waves and their traversing in the opposite directions obviously make the resulting reflected compression waves weaker.

Figure 8 shows the compression waves become weaker when the flow is controlled by a porous wall and a flat plate fitted at the leading edge of the cavity (see Fig. 1(a)) at Mach number 1.83 at the cavity entrance. These weaker compression waves will not be able to disturb the shear layer strongly enough to regenerate the instability waves in the shear layer. Therefore, a reduction of oscillations and a more stable shear layer was found for a cavity with control as shown in Figs.5 and 8, respectively. It is considered that some portion of the compression waves that goes through the holes of the porous wall will not return to the cavity and will be absorbed by the media between the upstream side and the porous wall.

Figures 9 and 10 also show a stable shear layer with a large, single and stable vortex inside the cavity with control at Mach number 1.50 and 1.83, respectively (Case 1).

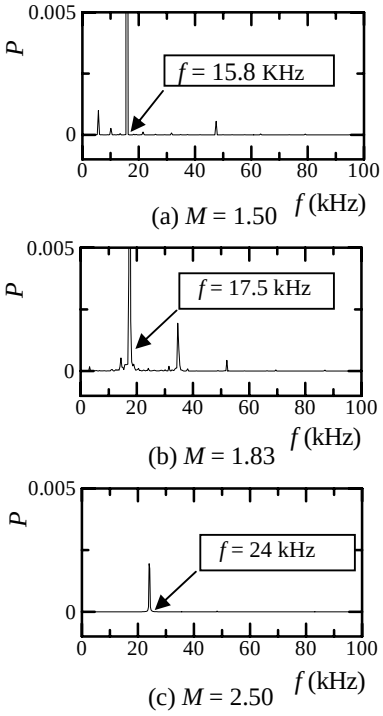

Fig.6 Distributions of power spectrum density without control

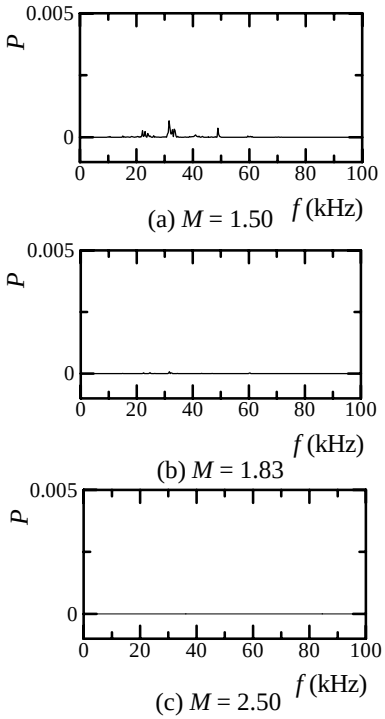

Fig.7 Distributions of power spectrum density with control

4.2 Effect of length of plate

In Cases of 1, 2 and 3 shown in Table 1, the porosity and the size of perforations T_2 were 0.5 and 1.2 mm, respectively. The simulation results showed a considerable amount of attenuation of the amplitudes of oscillation in case with a finite length of the flat plate where as increased amplitudes of oscillations and a very strong peak frequency in Case of 3 without a flat plate make it an unsatisfactory device to use as a cavity oscillations suppressor [7].

4.3 Effect of the size of perforation

It was observed that the size of perforation had some effects in controlling cavity-induced pressure oscillations. A slight increase in the amplitudes of oscillations was observed for the Cases of 5 and 6 compared with that of Case 1. PSD diagrams also showed some very small peaks for Cases of 4 and 5 [7].

4.4 Effect of inlet Mach Number

Figure 4 shows the time histories of static pressure without control at inlet Mach number 1.50, 1.83 and 2.50. Amplitudes of oscillations of static pressure variation are high in all the cases of different inlet Mach number without control and the magnitudes of mean static pressure vary with the variation of inlet Mach number as shown in Fig. 4. Although Mach number varies, amplitudes of oscillations reduce with the application of control device (porous wall) in all the cases of different inlet Mach number as shown in Fig. 5.

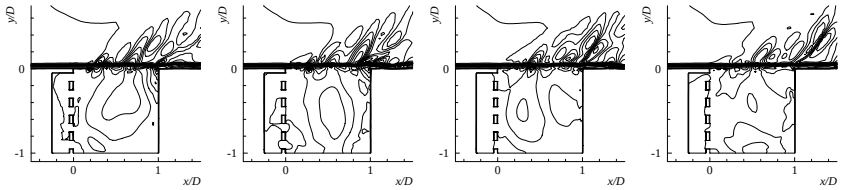

(a) $t = 0.25/f$ (s) (b) $t = 0.50/f$ (s) (c) $t = 0.75/f$ (s) (d) $t = 1.0/f$ (s)

Fig.8 Contour maps of density with control at Mach 1.83

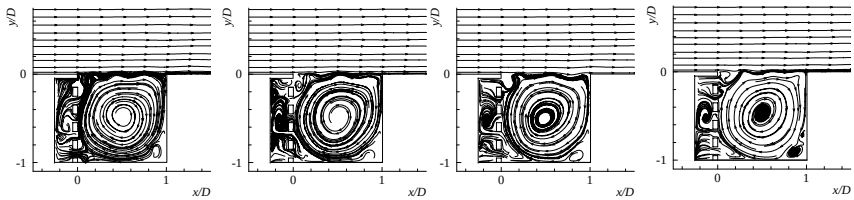

(a) $t = 0.25/f$ (s) (b) $t = 0.50/f$ (s) (c) $t = 0.75/f$ (s) (d) $t = 1.0/f$ (s)

Fig.9 Streamlines with control at Mach 1.50

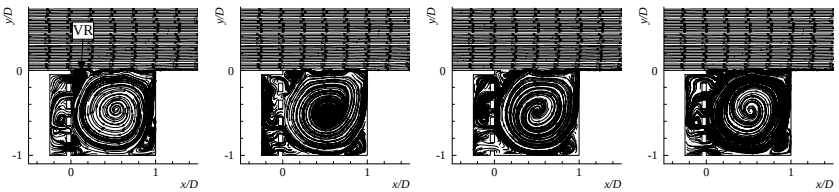

(a) $t = 0.25/f$ (s) (b) $t = 0.50/f$ (s) (c) $t = 0.75/f$ (s) (d) $t = 1.0/f$ (s)

Fig.10 Streamlines with control at Mach 1.83

Figure 6 shows the distributions of power spectrum density without control at Mach number 1.50, 1.83 and 2.50 at the cavity entrance. There are dominant peak frequencies in all the cases of different inlet Mach number as shown in Figs.6(a) though 6(c). It also shows that oscillation frequency varies with the variation of inlet Mach number. There is no peak frequency for cases with control at Mach number 1.83 and 2.50 as shown in Figs.7(b), 7(c). However, there is a very small peak frequency at Mach number 1.50 as shown in Fig. 7(a).

5. CONCLUSION

A computational study has been carried out for a supersonic two-dimensional flow over open, square cavities at Mach number 1.50, 1.83 and 2.5 at the cavity entrance. A porous wall near the front wall of the cavity covered by a flat plate had been investigated for the effectiveness of controlling the cavity-induced pressure oscillations. The results showed that the length of the flat plate and the size of perforation of the porous wall had an influence in controlling the cavity-induced pressure oscillations. Furthermore, a porous wall has shown its effectiveness in controlling the oscillation at Mach number 1.50, 1.83 and 2.5 at the cavity entrance. Therefore, effective attenuation of cavity pressure oscillations is possible for a square cavity with L/D_1=0.25, P = 0.5 and T_1/D_1=0.10 with a wide range of inlet Mach condition.

REFERENCES

[1] Krishnamurty, K., Acoustic Radiation from two Dimensional Rectangular Cutouts in Aerodynamic Surfaces, NACA TN-3487, August 1955.

[2] Roshko, A., Some Measurements of Flow in a Rectangular Cutout, NACA TN-3488, 1955.

[3] Rossiter, J. E., Wind-tunnel Experiments on the Flow over Rectangular Cavities at Subsonic and Transonic Speeds, Aeronautical Research Council RM-3438, October 1964.

[4] Heller, H. H., Bliss, D. B., The Physical Mechanism of Flow-Induced Pressure Fluctuations in Cavities and Concepts for their Suppression, AIAA Paper 75-491, 1975.

[5] Shaw, L., Clark, R., Talmadge, D., F-111 Generic Weapons Bay Acoustic Environment, *Journal of Aircraft*, 25 (1988), 2, pp. 147-153.

[6] Jeng, Y. N., Payne, U. J., Numerical Study of a Supersonic Open Cavity Flow and Pressure Oscillation Control, *Journal of Aircraft*, 32 (1995), 2.

[7] Setoguchi, T., Alam, M. M., Matsuo, S., Teramoto, K., and Yu, S., A Numerical Study on Passive Control of Cavity- induced Pressure Fluctuations in Two-dimensional Supersonic Flow, *International Journal of Turbo and Jet Engines*, 23 (2006), 3, pp. 155-164.

[8] Goldberg, U. C., Toward a Pointwise Turbulence Model for Wall-bounded and Free Shear Flows, *Trans ASME, Journal of Fluids Engineering*, 116 (1994), pp. 72-76.

[9] Goldberg, U. C., Exploring a Three-equation *R-k-*ε Turbulence Model, *Trans ASME, Journal of Fluids Engineering*, 118 (1996), pp. 795-799.

[10] Heiler, M., Instationäre Phänomene in Homogen/Heterogen Kondensierenden Düsen- und Turbinenströmungen, Dissertation, Fakultät für Maschinenbau, Universität Karlsruhe, Germany, 1999.

[11] Yee, H. C., A Class of High-resolution Explicit and Implicit Shock Capturing Methods, NASA TM-89464, 1989.

Proceedings of the 4th BSME-ASME International Conference on Thermal Engineering
27-29 December, 2008, Dhaka, Bangladesh

The Study of Spectral Properties of a Separation Bubble on a Circular Cylinder under the effects of free stream turbulence

N.A.Ahmed

Associate Professor, Aerospace Engineering,
School of Mechanical and Manufacturing Engineering,
University of New South Wales, Australia, NSW 2052
e-mail: n.ahmed@unsw.edu.au

ABSTRACT

An important area in fluid mechanics of fundamental significance is the occurrence of separation bubble on a body. The free stream effects on the spectral properties of a separation bubble on a circular cylinder are examined in this paper using a fluctuating pressure measurement technique. The tests were conducted in an open circuit, closed circuit wind tunnel at the aerodynamics laboratory of the University of New South Wales on the flow over a circular cylinder at a Reynolds number of 6.8 x 10^4 under turbulence intensities varying from 0.2% to 0.7%. The results are very promising and suggest that spectral properties may be used with good effect to indicate the occurrence, location and characterisation of separation bubble.

KEYWORDS : *Free stream, Spectral properties, Flow separation, bubble, fluctuating pressure, turbulence*

1. INTRODUCTION

Study of separation bubble formed on a body is an area of significant fundamental and applied research. In such studies, a lot can be learnt by the studying the flow over a circular cylinder which provides researchers to produce complex flows that are made of flows that can be isolated into regimes that are dominated by pressure forces and others that are dominated by viscous forces. It is therefore, not surprising that the area has attracted enormous interest in the past that dates back to well over a century. The effect of free stream turbulence on the flow over circular cylinder is an aspect that has also been widely studied [1-3].

In this paper the spectral trends in the fluctuating surface pressure distribution over a circular cylinder under different free stream turbulence conditions are explored with a

view of elucidating information about bubble formation and flow separation. The range of turbulence intensities studied was from 0.2% to 7% with corresponding non-dimensional integral [3] length scales (based on cylinder diameter, d=40±0.2) from 0.3-0.75.

The results show that, with increasing free stream turbulence a separation-reattachment bubble is formed that shortens in length. Characterisation of this bubble is performed by using power spectral density analysis of the fluctuating pressure plot topology. This is shown to be a more effective way of separation bubble detection than considering the Cp_{rms} distribution solely.

The studies were performed using a technique involving plastic tubing, a remote pressure transducer and a signal processing unit. The technique has been developed at the University of New South Wales to measure the mean and fluctuating pressure on the surface of a body exposed to flow [4]. The present study demonstrates further the application of the technique to more complex flow field is by providing the spectral properties of a separation bubble on a circular cylinder.

2. EXPERIMENTAL SETUP AND PROCEDURE

The tests were conducted in an open circuit, closed test section, low turbulence (0.2% to 40 m/s) wind tunnel [5]. The results were obtained at one Reynolds number of 6.8 x 10^4. To simulate the turbulent flow fields, three different, square mesh, biplanar turbulence-generating grids were placed between the contraction and the entrance to the test section. The grids were placed between the contraction and the entrance to the test section. The grids were circular cross-section bars of 2.5mm, 8 mm and 16 mm diameter with mesh widths of 25mm, 25mm and 40mm respectively. The circular cylinder was 520mm downstream of turbulence generating grids. The longitudinal turbulence intensities and integral length scales for these three flow configurations used were measured using a hot-wire anemometer at 2%, 4%, 7% and 14mm, 29mm and 34 mm respectively. At a minimum of 13 mesh lengths downstream of the largest meshed grid, the model was assumed to be in isotropic turbulence [6].

The smooth [7] circular cylinder spanned the test section (457mm x 457mm). Measurements of the fluctuating pressures were obtained from a 700mm length of calibrated plastic polystyrene pneumatic tubing with inner diameter 1.1.mm and wall thickness 0.5mm. One end of the tubing was connected to the model and its single tapping hole (0.75mm) and the other end connected to a pressure transducer (Scanivalve Corporation PDCR24D-1PSID). The recorded surface pressure signals were corrected for the signal magnitude distortion caused by the small diameter tubing. The overall accuracy of the system was within ±0.2 in 0.45 of Cp_{rms}.

End plates as specified by Stansby [8] were offset 35 mm off each of the test section walls to minimise three-dimensional effects from tunnel wall boundary layers. The test section blockage ratio and aspect ratio were 10% and 10 respectively. With this blockage, increases in free stream velocity of 8% and 11% were predicted by the blockage correction technique of Allen and Vincenti [9] and Maskell [10]

respectively. All the results are, however, presented uncorrected for blockage due to the suspect validity of present blockage correction techniques [11].

Results obtained from measurements taken over both sides of the cylinder were found to lie within a variation of ±0.2 in Cp_{rms}.

3. RESULTS AND DISCUSSION

The co-efficient of fluctuating pressure distribution over the circular cylinder obtained in the present investigation was first compared with published data [2-3] under similar flow conditions.

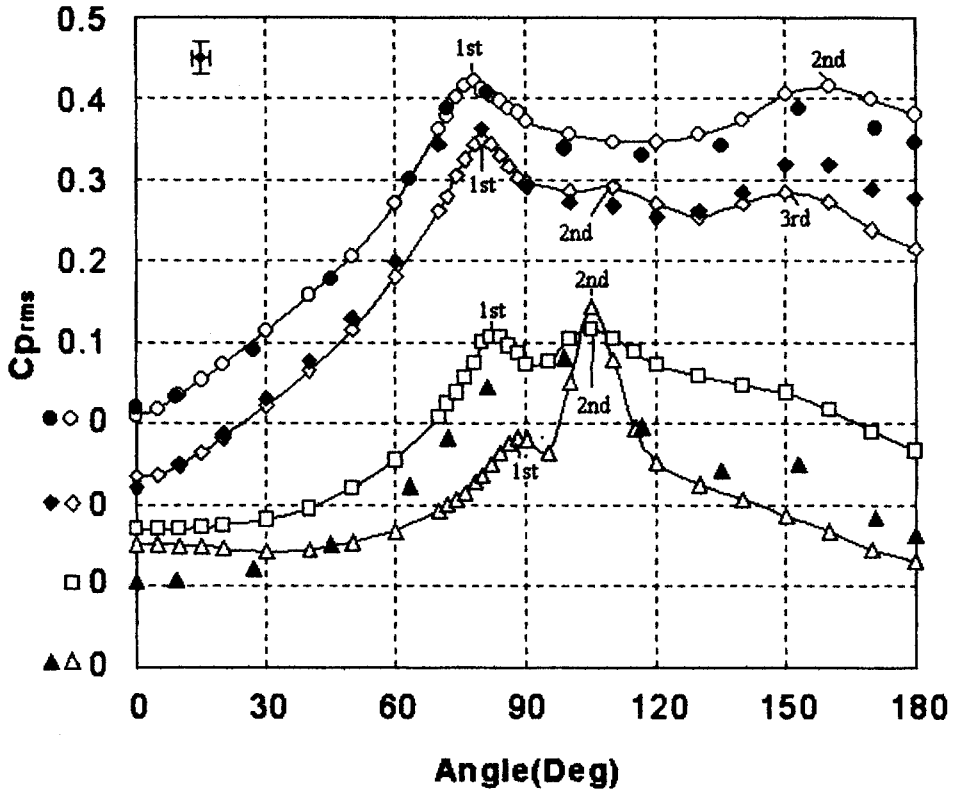

Figure 1. Fluctuating Pressure Distributions: Present Data, $Re_n = 6.8\times10^4$, AR=10, B=10%; Tu = 0.2% -o-, Tu = 2% -◇-, Tu = 4% -□-, Tu = 7% -△-: West&Apelt(1993), $Re_n = 9.5\times10^4$, AR>10, B=9.5%; Tu = 0.2% ●, Tu=5.5% ▲ : Norberg&Sunden(1987), $Re_n = 7.3\times10^4$, AR=9, B=11.8%; Tu=1.4% ◆.

As can be seen from Figure 1, there is good agreement between the published data and that obtained in the present work under similar turbulence intensities. From the data the PSD plots were obtained and are plotted against Strouhal number (fd/V) and angular position.

Figure 2 shows the PSD plot for the low free stream turbulence condition of 0.2% over the surface of the cylinder. The dominant vortex shedding peak is located at a non-dimensional frequency of 0.19. This peak, however, begins to disappear at $\theta=160^0$, where the roll up of the two alternatively shed shear layers close to the cylinder surface shifts the primary peak to double its primary frequency [1].

In the attached boundary layer up until separation the flow is laminar with the main spectral contributions concentrated around the main shedding peak of 0.19 [1]. After separation ($\theta=78^0$), the shear layer undergoes transition to turbulence increasing the spectral magnitude at non-dimensional frequencies above the shedding frequency. At the highest non-dimensional frequency the spectral magnitude at $\theta=180^0$ is 13 times the magnitude at $\theta=80^0$.

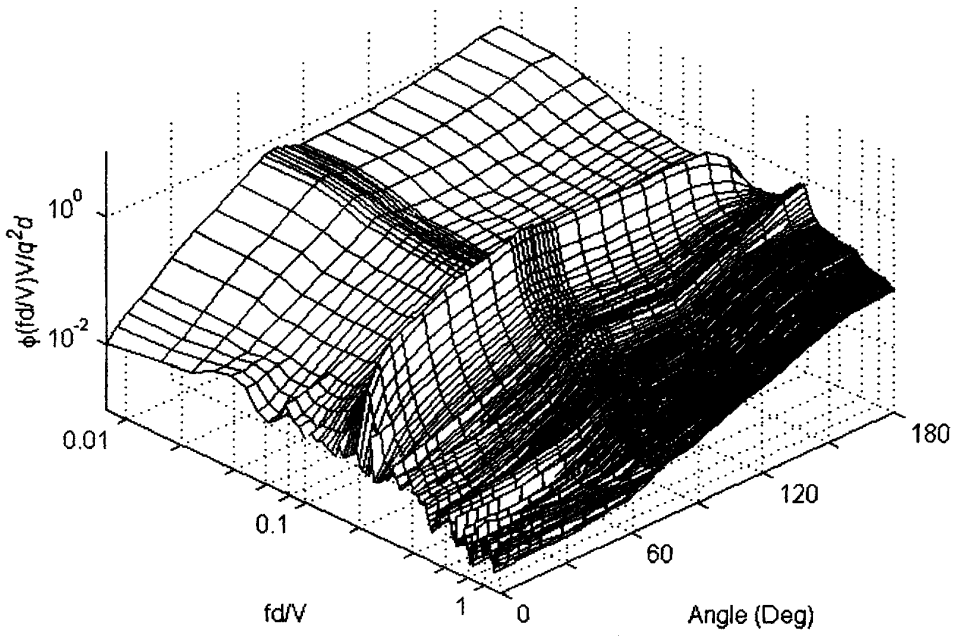

Figure 2: Power Spectral density plot of the fluctuating surface pressure
($Re_n = 6.8x\ 10^4$, Tu=0.2%)

With the increase in the free stream turbulence to 2%, figure 3 shows an increase in the spectral magnitude in two regions, around the stagnation region from $0<\theta<30^0$ and in a region extending from $78^0<\theta<130^0$. In the first region, the spectral magnitude increases by 6 to 8 times over the entire non-dimensional frequency range. This increase is due to the increase in free stream turbulence.

In the second region, extending the from $70^0<\theta<130^0$, the spectral magnitude has increased significantly. Above the non-dimensional frequencies of 0.2 and at $\theta=120^0$, a 4 fold increase occurs. For this flow condition, the 2nd maximum in the Cp_{rms} lies within the error band of measurement casting doubt on the existence of the

separation-reattachment bubble. Only by considering the PSD topology is the separation bubble clearly evident.

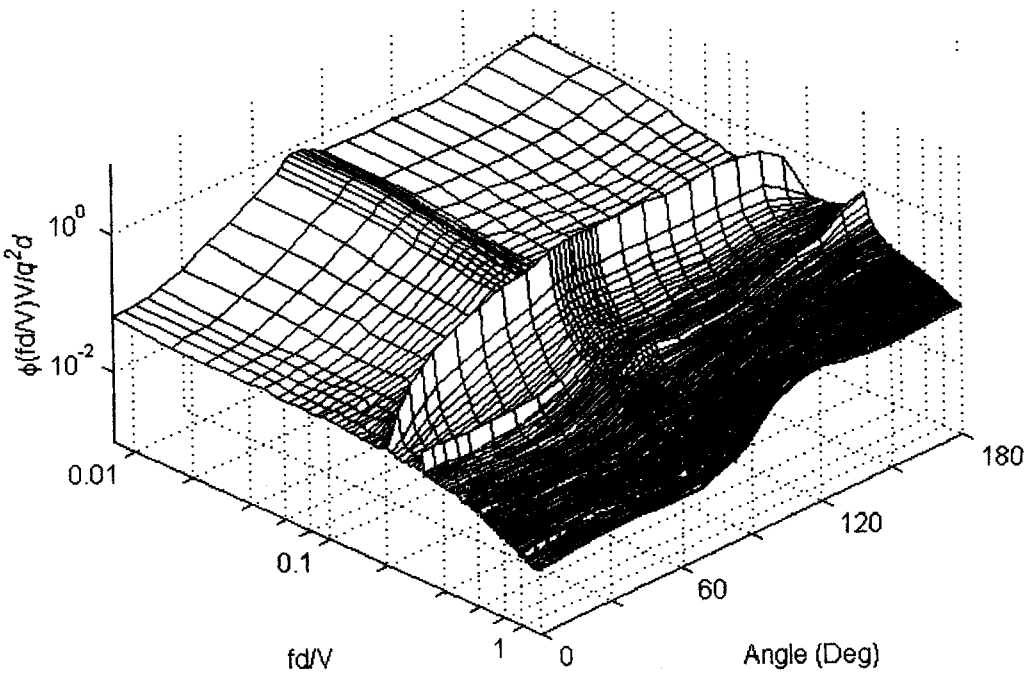

Figure 3: Power Spectral density plot of the fluctuating surface pressure ($Re_n = 6.8 \times 10^4$, Tu=2%)

When considering Figure 1, a separation-reattachment bubble is indicated by the first two peaks in the Cp_{rms} for the turbulence intensities of 2%, 4% and 7%. The first maximum, occurring in the range $\theta=82^0$-90^0 signifies the approximate position of the separation and the second, in the range $\theta=105^0$-115^0 indicative of flow re-attachment [1].

At higher non-dimensional frequencies (above fd/V=0.2) the maximum in the spectral magnitude of the PSD at these high non-dimensional frequencies is, therefore, considered an indication of the re-attachment position of the separated shear layer.

The trend shown in Figure 3 is also evident in figures 4 and 5. The angular position of the maxima in the spectral magnitude above fd/V=0.2 within the angular range $o78^0<\theta<130^0$ has reduced in angular position from that of figure 3 (at $\theta=115^0$) , signifying that a reduction in the bubble length has ensued with increase in free stream turbulence. The maxima were found to be at $\theta=110^0$and at $\theta=105^0$ respectively for 4% and 7% free stream turbulence. The corresponding maximum increase in magnitude over the low turbulence condition was 6 and 8 respectively.
For the three highest turbulent flows, the increase in the spectral magnitude in the range from at $\theta=80^0$ to $\theta=130^0$ is caused by the shear layer undergoing transition to turbulence. The initially shed smaller structures (fd/V >>1) coalesce into larger structures [12] with lower frequencies and are carried over the bubble [13], eventually

re-attaching to the surface. The frequencies of these structures are suggested to be of the order of $fd/V \approx 1$ [12] which is in agreement with current findings.

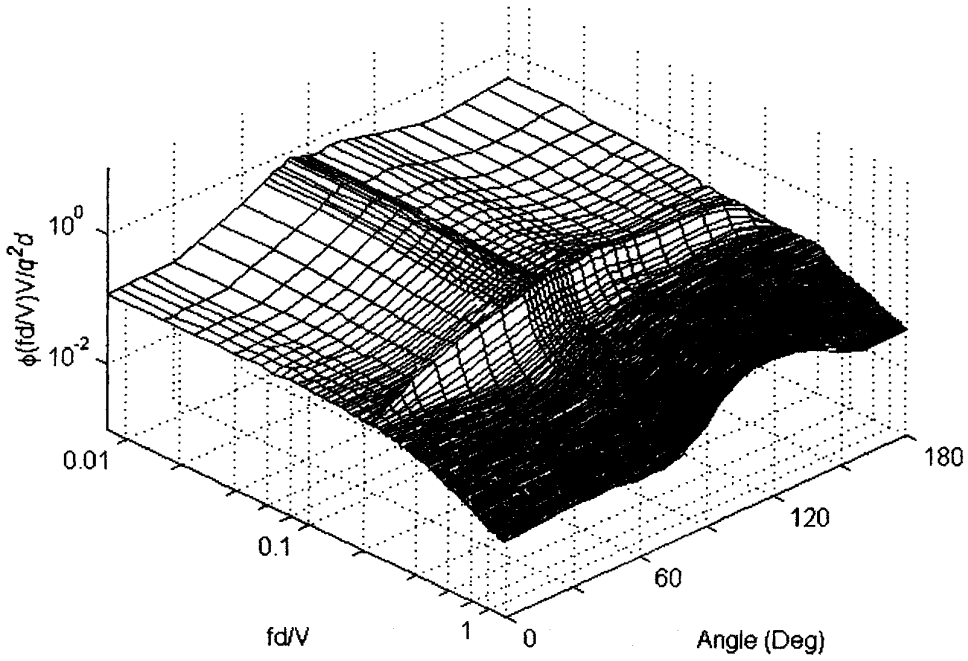

Figure 4: Power Spectral density plot of the fluctuating surface pressure ($Re_n = 6.8 \times 10^4$, Tu=4)

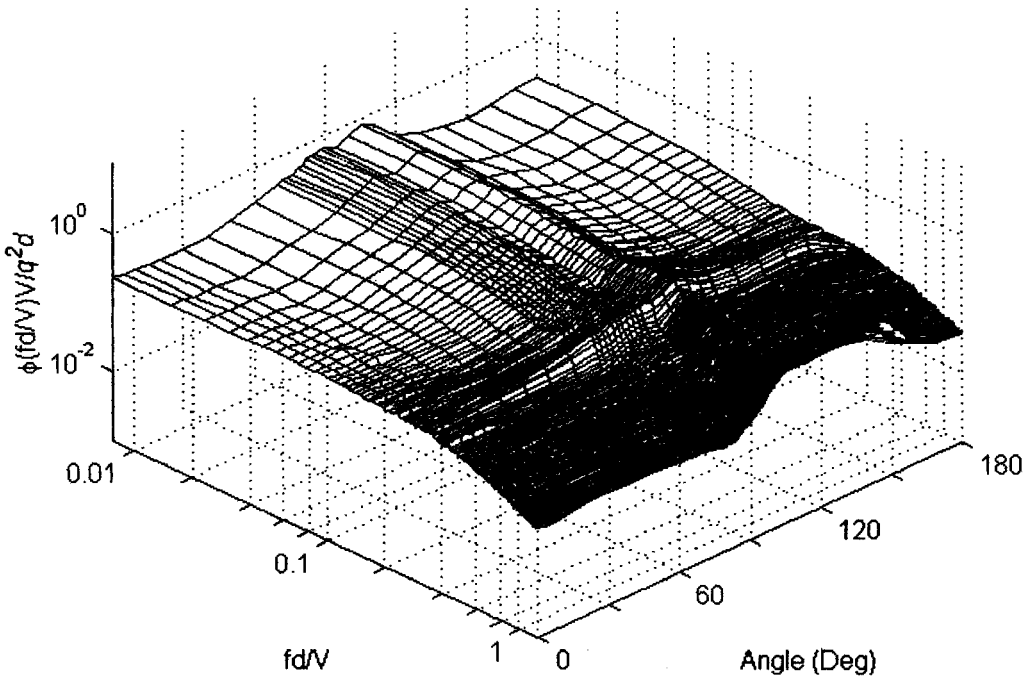

Figure 5: Power Spectral density plot of the fluctuating surface pressure ($Re_n = 6.8 \times 10^4$, Tu=7)

4. CONCLUSIONS

The effects of free stream turbulence on the spectral properties of a separation bubble over a circular cylinder are investigated. It was found that the increase in spectral magnitude at non-dimensional frequencies higher than 0.2 and in the angular range from $\theta=80^0$-130^0, was a good indication of the existence of a separation bubble.. The effect of free stream turbulence was found to reduce the length of the bubble with the Reynolds number fixed. The increase in the spectral magnitude above non-dimensional frequencies of 0.2 is due to separated structures coalescing into higher frequency larger structures increasing the ability of the separated shear layer to re-attach back to the surface.

5. NOMENCLATURE

Cp_{rms}	co-efficient of fluctuating pressure
d	outer diameter of cylinder
f	frequency
PSD	power spectral density
Re_n	Reynolds number based on cylinder diameter
Tu	turbulence intensity
V	free stream velocity
B	blocakge ratio
AR	Aspect ratio
θ	angular position measured from stagnation position
q	free stream dynamic pressure

6. REFERENCES

[1] Norberg, C. And Sunden, B., "Turbulence and Reynolds number effects on the flow and fluid forces on a single cylinder in cross flow", *Journal of Fluids and Structures*, vol.1, 1987, pp 337-357.

[2] West, G.S. and Apelt, C.J., "Measurement of fluctuating pressure and forces on a circular cylinder in the Reynolds number range from $10^4 < Re_n < 2 \times 10^5$", *Journal of Fluids and Structures*, vol.7, 1993, pp 221-244.

[3] Bearman, P., and Morel, T., "Effect of free stream turbulence on the flow around bluff bodies", *Progress in Aerospace Sciences*, vol.20, 1983, pp 97-123.

[4] Hinze, J.O., "Turbulence", McGraw Hill, 1959.

[5] Gatto, A, Ahmed, N.A.,Byrne, K.P. and Archer, R.D., 'Pressure Measurements over a Cylinder in Crossflow using Plastic Tubing', *Experiments in Fluids Journal*, vol 30, Issue 1, pp 43-46, 2001

[6] Ahmed, N.A and Wagner,D.J., "Vortex shedding and transition frequencies associated with flow around a circular cylinder", *AIAA Journal*, vol. 41, no.3, March, 2003, pp 542-544

[7] Achenbach, E., and Heinecke, E.,"On vortex shedding from smooth and rough cylinders in the range of Reynolds numbers 6×10^3 to 5×10^6 ", *Journal of Fluid Mechanics*, vol. 109, 1981, pp239-251.

[8] Stansby, P.K., “the effects of end plates on the base pressure co-efficient of a cicular cylinder’, *Aeronautical Journal*, vol.78, 1974, pp 36-37.
[9] Allen, H.J., and Vincenti, G.I., “Wall interference in a 2D wind tunnel, with consideration of the effect of compressibility”, *NACA Report* No.782, 1944.
[10] Maskel, E.C., “A theory of the blockage effects of bluff bodies and Stalled wings in a closed wind tunnel”, *Aeronautical Research Council Memorandum* 3400, 1963.
[11] West, G.S. and Apelt., “The effects of tunnel blockage and aspect ratio of the flow past a circular cylinder in the range 10^4 to 10^5”, *Journal of Fluid Mechanics*, vol.114, pp 361-377.
[12] Kiya, M., “Separation bubbles”, *Theoretical and Applied Mechanics*, P.Germain et al, eds, Elsevier Science Publishers (North-Holland), 1989, pp 173-191.
[13] Chong, M.S., Soria, J., Perry,A.E., Chacin, J., Cantwell, B.J., and Na Y., “Turbulence structures of wall bounded shear flows using DNS data”, *Journal of Fluid Mechanics*, vol. 357, 1998, pp 225-247.

Proceedings of the 4th BSME-ASME International Conference on Thermal Engineering
27-29 December, 2008, Dhaka, Bangladesh

DOMINATING SINGULARITY BEHAVIOR OF THE FLOW IN A POROUS PIPE WITH DECELERATING WALL

Rifat Ara ROUF, Md. Abdul Hakim KHAN

School of Engineering and Computer science, Independent University, Bangladesh.
Department of Mathematics, Bangladesh University of Engineering and Technology
Dhaka-1000, Bangladesh
e-mail: rifatar@secs.iub.edu.bd

ABSTRACT

In many physical problems, solutions are dominated by their singularities. The flow in a porous pipe with decelerating wall is important in that respect. Practically it is found that there is a range of Reynolds numbers for which there is no real solution to the steady similarity equation. In this paper various generalizations of approximation methods are exploited in order to study the dominating singularity behavior of the flow in a porous pipe with decelerating wall. The series related to the Reynolds number R is developed by using algebraic programming language MAPLE. It is observed that the convergence of the series is limited by the dominating singularity located at $R_1 \approx 3.0724980042$ and surprisingly there is another turning point at $R_2 \approx 8.813114939$. The result concluded that there is a reversal flow at the wall.

Key words: *Approximation method, High-order differential approximant, Singularity.*

1. INTRODUCTION

The mathematical models of physical phenomena are often nonlinear differential equations. Usually these type of problems cannot be solved exactly. Bender and Orszag [1] discussed the local behaviour of a number of nonlinear problems without solving the equation. They analyzed the series coefficients and justified their result with numerical integration. But when the exact closed form solution of a problem is too complicated or only a few numbers of terms of the series can be calculated then one should try to ascertain the approximate nature of the solution. Over the last quarter century, highly specialized techniques have been used to extract the series coefficients and at the same time variety of methods [1] have been devised for extracting the required information of the singularities from a finite number of series coefficients. Most of the methods are ratio like, such as Domb-Sykes plot [2], Neville-Aitken extrapolation [2], Hunter and Guerrieri method [3] etc. On the other hand Hermite-Pade′ class introduced seminumerical approximation methods, such as Pade′ approximants [1,4, 5], algebraic and differential approximants [4] etc. More recently Drazin and Tourigny [6] made some improvement to the algebraic approximant (D-T approximant) where they extended the theory for large number of series coefficients N. Parallely Khan [7] introduced High-order differential approximant (HODA) which is an extension of differential approximant. The purpose of this paper is to study numerically the comparative performance of the High-order differential approximant (HODA) to

determine the dominating singularity behavior of the solution to the problem with Pade′ approximant and Drazin-Tourigny approximant.

The first theoretical analysis of flow in a pipe with accelerating or decelerating wall was carried out by Berman [8] and subsequently Brady [9], Zaturska and Banks [10] have considered various aspects of the flow, both steady and unsteady. Brady and Acrivos [11] analyzed the flow in a pipe with accelerating wall. The steady axisymmetric flow of a viscous incompressible fluid driven along a porous pipe with decelerating wall is considered here. Like many authors, for example, Terrill and Thomas [12], Zaturska and Banks [10], Makinde [13] have investigated the problem. Makinde [14] studied the dominating singularity behaviour of the flow by using algebraic approximant Our approach is very parallel to Makinde by using differential approximant.

The structure of this paper is as follows: in Section 2 we derive a recurrence relation to get the Taylor series coefficients of the solution. We use approximate methods to analyze the dominant singularity behaviour of the solution in Section 3. Finally, conclusion of the paper is in section 4.

2. FORMULATION OF THE PROBLEM

Steady axisymmetric flow of a viscous incompressible fluid driven along a porous pipe with decelerating wall is considered. Let E be a parameter such that the axial velocity of the wall is Ez. It is assumed that $aE/V = O(1)$ and $V \neq 0$ ($V > 0$ represents suction velocity and $V < 0$ represents the injection velocity).

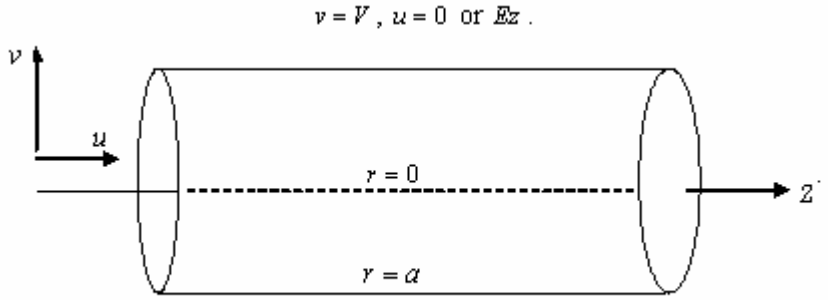

Fig. 1 Schematic diagram of the problem.

By assuming a similarity form for the solution of the Navier-Stokes equation it is found, after non-dimensionalization, that the velocity components (u, v) increasing in the directions of (z, r), respectively, and vorticity ω of the flow may be expressed as (Makinde [15])

$$u = \frac{z}{r}\frac{dF}{dr}, \quad v = -\frac{1}{r}F \text{ and } \omega = -zG.$$

And, hence, according to Makinde[14], the corresponding Navier-Stokes equations can be written as

$$\frac{d}{dr}\left[\frac{1}{r}\frac{d}{dr}(rG)\right] = R\left[\frac{G}{r}\frac{dF}{dr} - F\frac{d}{dr}\left(\frac{G}{r}\right)\right], \qquad G = \frac{d}{dr}\left(\frac{1}{r}\frac{dF}{dr}\right), \tag{1}$$

with the boundary conditions

$$F = 0, \ \frac{d}{dr}\left(\frac{1}{r}\frac{dF}{dr}\right) = 0, \text{ on } r = 0,$$

$$F = -1, \frac{dF}{dr} = -1, \text{ on } r = 1. \tag{2}$$

Here $R = Ea^2/\upsilon$ is the Reynolds number with a characteristic length and υ kinematic viscosity of the flow. Equations (1) with the boundary conditions (2) govern the motion of an incompressible fluid through the porous pipe with decelerating wall. An exact solution to this complicated nonlinear system of equations for $R \neq 0$ is not available, so we resort to series analysis by approximation methods. When $R = 0$, equations (1) can be solved exactly. The solution is a parabolic Poiseulli flow. It is therefore natural to seek a power series in ascending powers series of R (for small R):

$$F(r) = F_0(r) + F_1(r)R + F_2(r)R^2 + F_3(r)R^3 + \Lambda \,. \tag{3}$$

By substituting (3) into (1) and using the usual tricks, we obtain recurrence relations for the unknown coefficients of this series

$$\left[\frac{1}{r}(rG_n)'\right]' = R\sum_{i=0}^{n-1}\left[G_i\left(\frac{F'_{n-i-1}}{r}\right) - F_i\left(\frac{G_{n-i-1}}{r}\right)'\right], G_n = \left(\frac{1}{r}F_n{}'\right)', \tag{4}$$

with

$$F_n = 0, \left(\frac{1}{r}F'_n\right)' = 0 \text{ on } r = 0,$$

$$F_0 = -1, F_{n+1} = 0, F'_0 = -1, F'_{n+1} = 0, \text{ on } r = 1, n = 0,1,2,...$$

Where the prime denotes differentiation with respect to r. In order to compute the series coefficients, let

$$F_i(r) = \sum_{j=1}^{2i+2} a_{0,2j} r^{2j} \,,$$

and hence

$$F(r,R) = \sum_{i=0}^{\infty}\left(\sum_{j=1}^{2i+2} a_{0,2j} r^{2j}\right)R^i \,. \tag{5}$$

By substituting (5) to the equation (4), the recurrence relation for *F(r)* becomes

$$16j(j+1)^2(j+2)a_{2j+4}r^{2j-1} = \sum_{j=1}^{k} 8\frac{(j+1)!}{(j-1)!}(k-j+1)a_{2j+2}a_{2k-2j-2}r^{2k-1}$$

$$-\sum_{j=1}^{k} 8\frac{(k-j+3)!}{(k-j)!}a_{2j}a_{2k-2j+6}r^{2k+1}$$

We expand $F(r,R)$, $\beta = \left(\frac{F'}{r}\right)'$ at $r = 1$ and $F''(0)$ (that is, stream function, skin friction and centerline axial velocity parameter) in powers of Reynolds number to obtain

$$F(r) = -\frac{1}{2}r^2(3-r^2) - \frac{1}{144}r^2(7-r^2)(1-r^2)^2 R + \ldots,$$

$$\beta = 4 - \frac{1}{3}R - \frac{2}{27}R^2 - \frac{17}{1008}R^3 - .... \tag{6}$$

and

$$F''(0) = -3 - \frac{7}{72}R - \frac{103}{4800}R^2 - \frac{760589}{152409600}R^3 - \ldots \qquad \text{as } R \to 0 \,. \tag{7}$$

These expansions yield a single solution of the equation (1). Using a symbolic algebraic language MAPLE, first 54 coefficients of the solution is obtained (Rouf [18]). It was observed that the sign of the coefficients are same and monotonically decreasing in magnitude.

3. RESULT AND DISCUSSION

The convergence of the series may be limited by a singularity on the positive real axis (Van Dyke [16]). The graphical form of the D'Alembert's ratio test (Domb and Sykes [17]) together with Neville's extrapolation at $\frac{1}{n}=0$ (that is, $n\to\infty$) reveal the radius of convergence $R=3.07249$ (Makinde [14]). Following the High-order Differential approximation technique, the first and second turning points R_1 and R_2 are computed as $R_1\approx 3.0724980042$, $R_2\approx 8.813114939$ as shown in Table 1 and 2.

Tab. 1: Estimates of the critical Reynolds number $R_{1,N}^{(d)}$, $R_{2,N}^{(d)}$ and the critical exponent α_N for the centerline axial velocity function $F''(0)$ by using High-order Differential Approximant. The last row shows the estimates obtained by using the Drazin-Tourigny approximant [6].

d	N	$R_{1,N}^{(d)}$	$\alpha_{1,N}$	$R_{2,N}^{(d)}$	$\alpha_{2,N}$
2	7	3.1748622903786039	0.734469546787185866	----------	----------
3	12	3.0768641905315211	0.511490960893766009	----------	----------
4	18	3.0725166917148683	0.499719619856999405	----------	----------
5	25	3.0724980065120133	0.499999902120348536	8.8164063517596622	0.4954596938484847968
6	33	3.0724980042445946	0.500000000098284071	8.8127995287711051	0.4991471015647478523
7	42	3.0724980042458199	0.499999999999926717	8.8131460358460523	0.4997653746760795187
8	52	3.0724980042458197	0.500000000000000001	8.8131097616625635	0.4999534119259680143
9	**53**	**3.0724980042458197**		**8.813114939**	

Tab. 2: Estimates of the critical Reynolds number $R_{1,N}^{(d)}$, $R_{2,N}^{(d)}$ and the critical exponent α_N for the skin friction function β by using High-order Differential Approximant. The last row shows the estimates obtained by using the Drazin-Tourigny approximant [6].

d	N	$R_{1,N}^{(d)}$	$\alpha_{1,N}$	$R_{2,N}^{(d)}$	$\alpha_{2,N}$
2	7	3.169913601171531	0.1179160833837563	----------	----------
3	12	3.078390933009397	0.4328071188188094	----------	----------
4	18	3.072506610273949	0.4997190813662425	8.942239101069277	0.4060409189553583854
5	25	3.072498003441932	0.5000000089906489	8.441094619719760	2.7332819731928286414
6	33	3.072498004254962	0.4999999990682636	8.810061064410313	0.5076020616853571302
7	42	3.072498004245820	0.4999999999987227	8.813263038742537	0.4991927215986543196
8	52	3.072498004245819	0.4999999999999999	8.813083811310784	0.5003197469645002604
9	**53**	**3.0724980042458197**		**8.813114939**	

The partial sums of the series are used to reconstruct the other solutions of the problem. The series has a real singularity at $R = R_1$ and this singularity corresponds to a turning point i.e. a value of R where the number of solutions changes abruptly. It seems that $R_{1,N}^{(d)}$ approximates R_1 very well as d increases. A farther turning point at $R = R_2$ is also computed . The bifurcation diagrams for the approximate solutions are shown in Figure 2 and 3. One can go through Rouf [18] to compare the figures for different values of d .

As can be seen in the figures, Drazin-Tourigny approximant succeeds in continuing the secondary singularity behavior beyond the circle of convergence of the series. The dominating singularity is of the form

$$\beta \text{ or } F''(0) \sim A(R - R_1)^{\alpha} \quad as \quad R \to R_1 ,$$

where A is a constant, with the critical exponent $\alpha \approx 1/2$. It is interesting to notice the absence of real solutions for $R_1 < R < R_2$, and that $\beta \to 0$ as $R \to 2.828847....,$ that is, reversal of the flow occurs at the wall.

Table 1 and 2 shows that the accuracy of the approximations $R_{1,N}^{(d)}$ and $R_{2,N}^{(d)}$ increases very rapidly with the increase of d .

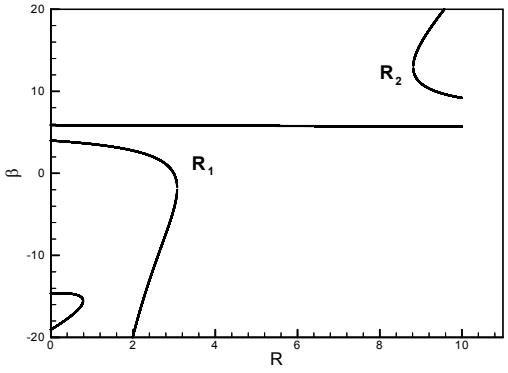

Fig. 2. The bifurcation diagram in the (β, R) plane near the first and second turning points R_1 and R_2 for the problem using Drazin-Tourigny approximant with $d = 8$. Other curves are spurious.

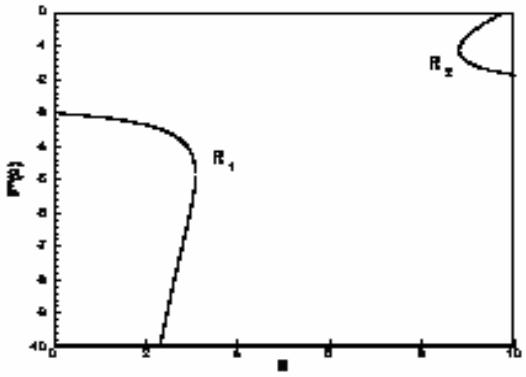

Fig. 3. The bifurcation diagram in the $(F''(0), R)$ plane near the first and second turning points R_1 and R_2 for the problem using Drazin-Tourigny approximant with $d = 8$. Other curves are spurious.

4. CONCLUSIONS

This paper investigated the dominating singularity behavior of the flow in a porous pipe with decelerating wall by using High-order differential approximant and compared the result with other methods.

It is observed that High-order differential approximant is very competitive, but for the approximation of bifurcation diagram Drazin-Tourigny approximant is essential. Very accurate approximation of the first bifurcation point R_1 and surprisingly a good estimate of the second turning point R_2 have been produced. Furthermore, not only the critical point but also the critical exponent have been produced as shown in Table 1and 2. We provide a basis for guidance about

what method of summing power series should be chosen for many problems in fluid dynamics in order to show the critical behaviour of the flow.

5. REFERENCES

[1] Bender, C., Orszag, S. A., Advanced Mathematical Methods for Scientists and Engineers, McGraw-Hill, New York,1978.

[2] Guttmann A.J., Asymptotic Analysis of Power Series Expansions, Academic Press, New York, 1989.

[3] Hunter D.L., Baker G.A., Methods of Series Analysis III: Integral Approximant Methods, *Phys. Rev*. B 19 (1979), pp 3808-3821.

[4] Baker, G. A .Jr., Graves-Morris, P., Pade′ Approximants, Second edition, Cambridge University Press, Cambridge, 1996.

[5] Tourigny Y., Drazin P. G., The Dynamics of Pade′ Approximation, Nonlinearity, 15 (3) (2002), pp. 787-806.

[6] Drazin, P.G., Tourigny, Y., Numerically Study of Bifurcation by Analytic Continuation of a Function defined by a Power Series*, SIAM J. Appl. Math*., v. 56 (1996), pp.1-18.

[7] Khan, M.A.H., High-order Differential Approximants, *J. of Comp. & Appl. Maths,* v.149 (2002), pp. 457-468.

[8] Berman, A. S., Laminar Flow in Channels with Porous Walls, *J. Appl. Phys*, v 24 (1953), pp. 1232-1235.

[9] Brady, J. F., Flow Development in a Porous Channel and Tube, *Phys. Fluids*, v.27 (1984), pp.1061-1067.

[10] Zaturska, M. B., Banks W. H. H., Flow in a Pipe driven by Suction at an Accelerating Wall, Acta Mechanica, v.110 (1995), pp. 111-121.

[11] Brady, J. F., Acrivos, J., Steady Flow in a Channel or Tube with an Accelerating Surface Velocity. An Exact Solution to the Navier-Stokes Equations with Reverse Flow, *Fluid Mech*, v. 112 (1981), pp. 127-150.

[12] Terrill R. M., Thomas P. W., Laminar Flow through a Uniformly Porous Pipe, *Appl. Sci. Res*, v.21 (1969), pp. 37-67.

[13] Makinde, O.D., Unsteady Incompressible Flow in a Porous Channel, Proc. Appl. Indust. Maths., Conf. Rom., Oradea, 1994, pp. 47-58,.

[14] Makinde, O. D., Extending the Utility of Perturbation Series in problems of Laminar Flow in a Porous Pipe and a Diverging Channel . *J. Austral. Math. Soc. Ser.*, B v. 41(1999), pp. 118-128.

[15] Makinde, O. D., Computer extension and Bifurcation study by Analytic Continuation of the Porous Tube Flow problem, *J. Math. Phys. Sci.*, v.30 (1996), pp.1-24.

[16] Van Dyke M., Analysis and Improvement of Perturbation Series, *Quart. J. Mech. Appl. Math,.* v. 27 (1974), pp. 423-449.

[17] Domb, C., Sykes, M. F., On the Susceptibility of a Ferromagnetic above the Curie Point, Proc. R. Soc. London, Ser A, 1957, v. 240, pp 214-228.

[18] Rouf R. A., Study of Dominating Singularity Behavior of Series by Computer Based Approximation Techniques, M. Phil. thesis, Bangladesh University of Engineering and Technology, BUET, Bangladesh, 2007.

Proceedings of the 4th BSME-ASME International Conference on Thermal Engineering
27-29 December, 2008, Dhaka, Bangladesh

CONTRACTION OF LIQUID SHEET IN A STILL GAS MEDIUM

Mohammad Ali*1, A. Umemura*2 and Md. Quamrul Islam*1

*1 Department of Mechanical Engineering, BUET, Dhaka, Bangladesh
*2 Department of Aerospace Engineering, Nagoya University, Nagoya, Japan
email: mali@me.buet.ac.bd

ABSTRACT

A numerical has been performed on the contraction of liquid sheet in a still quiescent gas medium to provide insights into the dynamics of capillary wave created during contraction. The problem composed of the Navier-Stokes system is associated with initial and boundary conditions that govern the time evolution of the capillary wave and the pressure and velocity fields within it. The algorithm is capable of capturing the capillary wave and therefore it is used to study the characteristic phenomena of the liquid sheet during its contraction. Results show that the capillary wave is radiated from the tip of the liquid sheet caused by surface tension. The amplitude of the tip wave is much larger than any other waves and the asymptotic approach of the wave peaks can be observed during the propagation of waves. The tip wave contains the highest pressure and gradually the peak values of both high and low pressures decreases with the propagation of waves. Fluid velocity is motivated by both pressure due to surface tension and recirculation in peak and trough of the wave.

KEYWORDS: *Capillary wave, Liquid sheet, Surface tension, Jet atomization VOF method.*

1. INTRODUCTION

There are many industrial processes where liquid spray is widely used in the system and an important factor for producing quality products. The purpose of liquid breaking in a spray is to increase the liquid surface area for increasing the subsequent heat and mass transfer. The spatial distribution, or dispersion of the droplets, is important in many combustion systems because it affects the mixing of fuel with oxidizer, which influences the flame length. Therefore to understand the mechanism of atomization is very important for its efficient application and to improve the design of practical combustion devices. Before occurring atomization, a wave of very small amplitude is formed on the liquid surface, which is called capillary wave. The detailed knowledge on the characteristics of capillary wave is required to understand the insight mechanisms for the disintegration of liquid. However, it is a difficult task to capture the capillary wave in numerical simulation. A suitable numerical algorithm is required to solve the problem. Several methods were proposed and in use for the simulation of such flow problems. These methods are discussed in reference [1-3]. Gueyffier et al. [1] described a numerical scheme for interface calculations. The author used the volume of fluid interface tracking method and a piecewise linear interface calculation in the scheme. The method of interface tracking with the connection of volume fraction and interface position was described in detail. A new model called continuum surface force (CSF) for surface tension effects on fluid motion was developed by Brackbill et al. [2]. The model interpreted the surface tension as a continuous, three-dimensional effect across an interface, rather than as a boundary value condition on the interface. Welch et al. [3] used a VOF based interface tracking method in conjunction with a mass transfer model and used in simulation of horizontal film boiling problem. The method utilized local discrete material volume and velocity data to track liquid interfaces. All the above researchers used VOF method for two-phase flow problems with the conjunction of some other models and techniques. Therefore, it can be concluded that the VOF method is one of the most popular schemes for tracking interfaces and hence implemented in present algorithm.

In liquid jet atomization capillary instability and disintegration of liquid are important and interesting phenomena to the fluid dynamists. An earlier account of the work is summarized by Rayleigh [4] who

performed a delightful discussion on jet instability and published both theoretical and experimental results on capillary instability phenomena. During the contraction of liquid jet or cylindrical liquid drop the capillary waves are radiated on the fluid interfaces. These waves are caused by surface tension and generated at the tip of liquid jet. In an experiment Goedde and Yuen [5] examined the capillary instability of vertical liquid jets of different viscosities and measured the growth rates of waves for disturbances of various wavelengths. The author discussed about the drop formation and ligament detachment and showed that some non-linear effects became very pronounced especially at small wave number and dominated the growth processes. In another investigation Donnelly and Glaberson [6] performed some experiments and discussed the effects of viscosity on the capillary instability and growth rate. Also several other investigations [7, 8] can be found in the literature which described general features on end pinching of elongated liquid drops, their deformation and breakup. No capillary wave was observed at the tip of the elongated liquid drop with the conditions they considered. Obviously, the phenomenon of capillary wave is a complicated one and difficulties are there to capture this wave in the resolution.

From the above discussion, it is revealed that the study of the capillary wave created on the liquid surface has been given a little attention in the literature, which has been addressed in the present study. To achieve the goal, a three-dimensional numerical code is developed and validated with experimental data. The code is then used for numerical simulation to understand the phenomena of capillary waves radiated from the tip of the liquid sheet in an otherwise quiescent fluid.

2. NUMERICAL FORMULATION

The flow field is governed by time dependent three-dimensional Navier-Stokes equations with surface tension force. Body forces are neglected. These equations can be expressed as

$$\frac{\partial \vec{U}}{\partial t}+\frac{\partial \vec{P}}{\partial x}+\frac{\partial \vec{Q}}{\partial y}+\frac{\partial \vec{R}}{\partial z}=\frac{\partial \vec{P}_v}{\partial x}+\frac{\partial \vec{Q}_v}{\partial y}+\frac{\partial \vec{R}_v}{\partial z}+\vec{F}_{sv} \tag{1}$$

$$U=\begin{pmatrix}\rho\\ \rho u\\ \rho v\\ \rho w\end{pmatrix},\quad P=\begin{pmatrix}\rho u\\ \rho u^2+p\\ \rho uv\\ \rho uw\end{pmatrix},\quad Q=\begin{pmatrix}\rho v\\ \rho uv\\ \rho v^2+p\\ \rho vw\end{pmatrix},\quad R=\begin{pmatrix}\rho w\\ \rho uw\\ \rho vw\\ \rho w^2+p\end{pmatrix}$$

$$P_v=\begin{pmatrix}0\\ \tau_{xx}\\ \tau_{xy}\\ \tau_{zx}\end{pmatrix},\quad Q_v=\begin{pmatrix}0\\ \tau_{xy}\\ \tau_{yy}\\ \tau_{yz}\end{pmatrix}.\quad R_v=\begin{pmatrix}0\\ \tau_{zx}\\ \tau_{yz}\\ \tau_{zz}\end{pmatrix}\quad F_{sv}=\begin{pmatrix}0\\ \sigma\kappa f n_x\\ \sigma\kappa f n_y\\ \sigma\kappa f n_z\end{pmatrix}$$

The following terms are expressed as

$$\tau_{xx}=\lambda\left(\frac{\partial u}{\partial x}+\frac{\partial v}{\partial y}+\frac{\partial w}{\partial z}\right)+2\mu\left(\frac{\partial u}{\partial x}\right),\qquad \tau_{yy}=\lambda\left(\frac{\partial u}{\partial x}+\frac{\partial v}{\partial y}+\frac{\partial w}{\partial z}\right)+2\mu\left(\frac{\partial v}{\partial y}\right),\qquad ,$$

$$\tau_{zz}=\lambda\left(\frac{\partial u}{\partial x}+\frac{\partial v}{\partial y}+\frac{\partial w}{\partial z}\right)+2\mu\left(\frac{\partial w}{\partial z}\right),$$

$$\tau_{xy}=\mu\left(\frac{\partial u}{\partial y}+\frac{\partial v}{\partial x}\right),\quad \tau_{yz}=\mu\left(\frac{\partial w}{\partial y}+\frac{\partial v}{\partial z}\right),\quad \tau_{zx}=\mu\left(\frac{\partial w}{\partial x}+\frac{\partial u}{\partial z}\right),\quad \lambda=-\frac{2}{3}\mu.$$

Where, u, v, w are velocities in the flow field, ρ the density, p the pressure, μthe viscosity, F_{sv} the surface tension force, σ the surface tension, κ the curvature of surface, n the unit normal to the surface and f is a function for continuous change of the color variable (here density) across the thickness of fluid interface.

3. PROBLEM STATEMENT

The contraction of a two-dimensional liquid sheet in a still gas medium is considered to understand the phenomena of capillary wave radiated from the tips of the liquid sheet. The schematic of the liquid sheet is shown in Fig.1. Sulfur hexafluoride (SF_6) of critical temperature, 318.7 K and critical pressure, 3.76 MPa is used as liquid and gaseous nitrogen is used as immiscible, viscous fluid with pressure of 7.0 MPa.. The half-thickness of the liquid sheet is 1.5×10^{-4} m and denoted as 'a' shown in Fig.1. The length of the sheet is made dimensionless by the ratio of the actual length to half-thickness i.e. L/a, and accordingly the non-dimensional length of the liquid sheet is 80. High length to half-thickness ratio is considered to keep the capillary waves away from the effects of boundary conditions imposed at the end of symmetry. The width of the sheet is long enough to solve the problem as two-dimensional. The thickness of calculation domain is 12.67 times larger than the half thickness of the liquid sheet. At the beginning of calculation, the velocities of both liquid and gas are considered as zero. The above numerical parameters are used for present calculation because some experimental results on liquid atomization problem are available in the work of Umemura and Wakashima [9] using the same parameters. The grid size for simulation is 2.0×10^{-5} m and the calculation is performed on regular and uniform grids for both of liquid and gas. The grid system 620x95 is considered for this calculation along the horizontal and vertical directions, respectively. Solid boundary conditions for Navier-Stokes simulation are imposed on three sides of the domain except symmetric end for velocity and pressure. Zero velocity and zero gradient of pressure are considered for symmetric end.

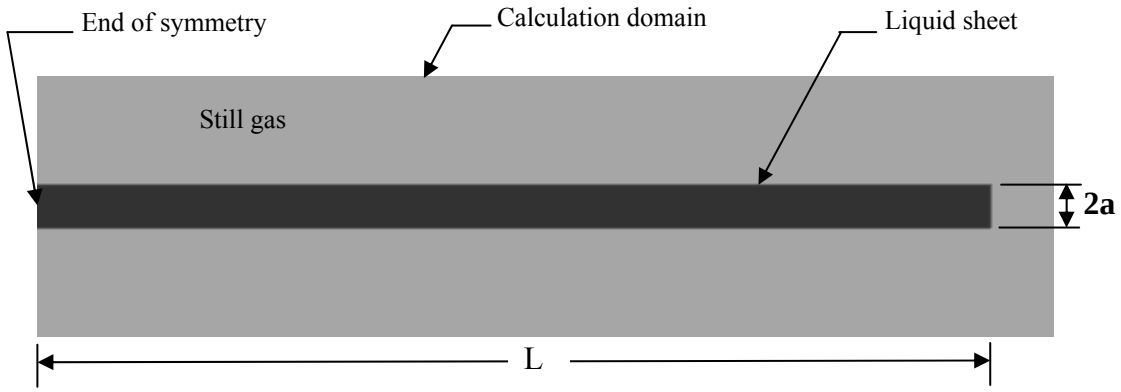

Fig.1 Schematic of the calculation domain for contraction of liquid sheet; a = half-thickness of liquid sheet

4. RESULTS AND DISCUSSION

Figure 2 shows the time evolution history of capillary waves during the contraction of liquid sheet. The times reported have been made dimensionless with respect to the timescale, $t_c = \sqrt{\frac{\rho_l a^3}{\sigma}}$, where ρ_l = the density of liquid, a = the half-thickness of the unperturbed liquid sheet, and σ = the surface tension. Initially the tip of the liquid sheet is rectangular in shape. Due to surface tension force, the deformation of the shape is initiated at the rectangular corner of the sheet tip. Initial deformation of the tip can be observed from Figs.2(a~b). Three corners are generated from two corners of the rectangular shape as shown in Fig.2(b) and the deformation continues. Gradually, the tip of the liquid sheet becomes round with a neck to connect the head with the body of sheet. Due to surface tension, capillary waves propagate on the rest of the liquid surface. Here the amplitude of the wave is calculated as the distance from the unperturbed liquid surface to the peak of the wave and is made dimensionless as dividing it by "a". The wave length is calculated by the distance of two consecutive wave necks. The peak and neck of the wave are shown in Fig.3. After the formation of round tip, the first wave can be observed at dimensionless time, 11.12 with dimensionless amplitude of 0.25 and the wavelength of 5.6 besides the tip wave. At this time, the round shape of the liquid tip (the tip wave) transforms into a wavy shape with amplitude of 2.0 and wavelength of 6.3. The wave propagates along the liquid surface to the midsection of the liquid creating

waves of shorter wavelength with the distance away from the tip. The waves are stocking in nature and for time being they increase their wavelengths occupying more liquid.

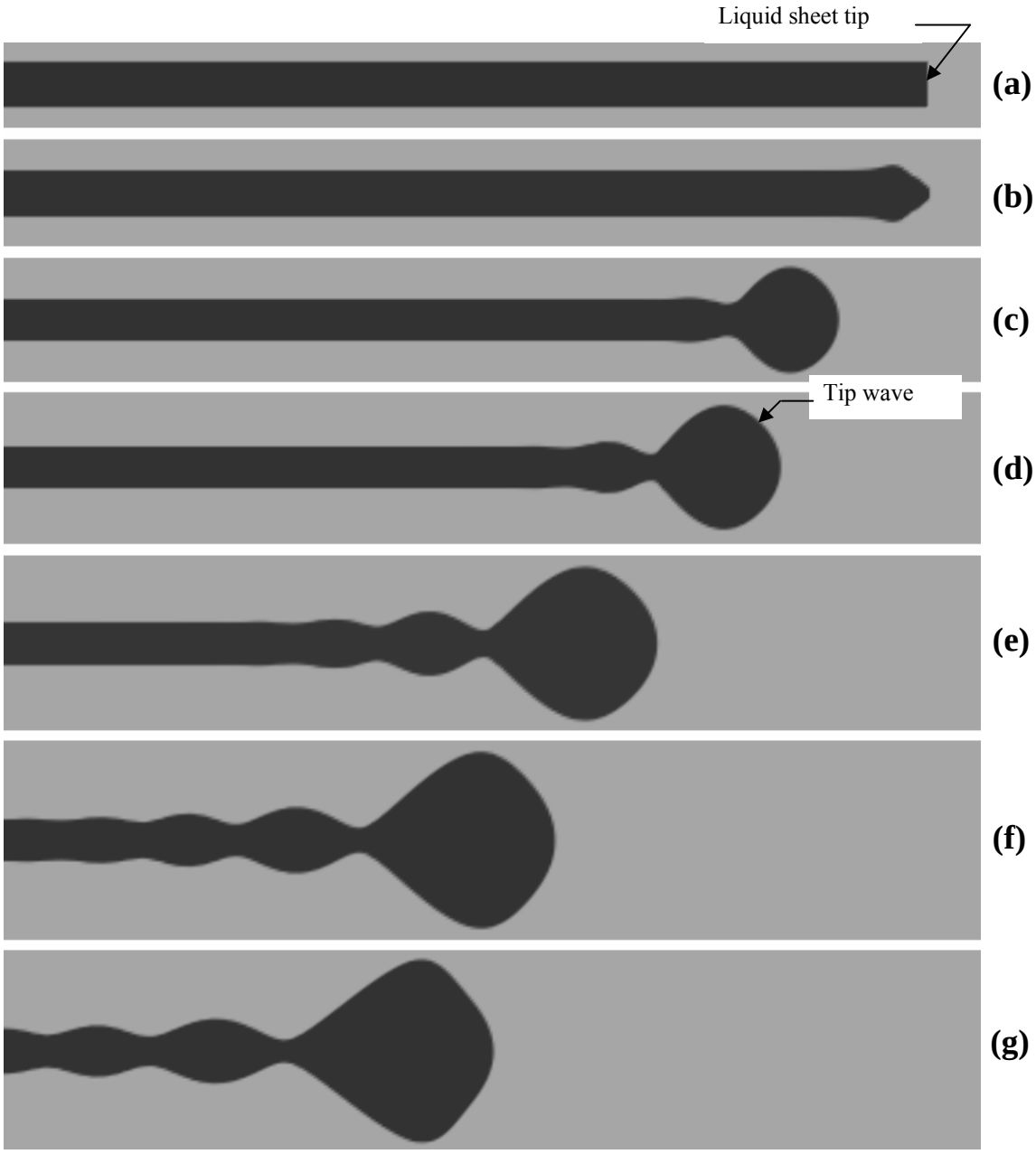

Fig.2 Evolution of capillary waves during contraction of liquid sheet; Dimensionless time, (a) t = 0.0, (b) t = 0.32, (c) t = 2.54, (d) t = 4.0, (e) t = 7.0, (f) t = 10.0, and (g) t = 13.0.

Figures 2(e~g) are of same interval of time showing the number of waves propagated on the liquid interfaces. By investigation it can be understood that the frequency of wave generation is not constant. The propagation time of the following waves is shorter than the predecessor which is the characteristics of capillary wave. It can be pointed out that Fig. 2(g) occupies four waves besides large tip wave. Due to space constraint, Fig. 2(g) covers only two and a half waves showing the distance of liquid tip position from its original position at time, t = 0. All the waves radiated at time, t = 36.18 can be found in Fig.3. For easy understanding about the waves, the narrower and wider passages of the waves are denoted as “neck” and “peak”, respectively as shown in Fig.3. The position of different necks from left boundary of calculation domain is mentioned in this figure. It is noted that the non-dimensional length of liquid sheet at time, t = 0 is 80. At t = 36.18, after contraction, the length of the sheet becomes 55.87 and within this time 5 complete waves are formed with different wave amplitudes. The peaks of the generating waves are asymptotic approach, i.e. the amplitude of the wave peak decreases asymptotically and within the time, t=

36.18 the dimensionless amplitude of the tip wave is 4.7 and that of the following four waves are 1.65, 1.3, 1.16 and 1.06, respectively.

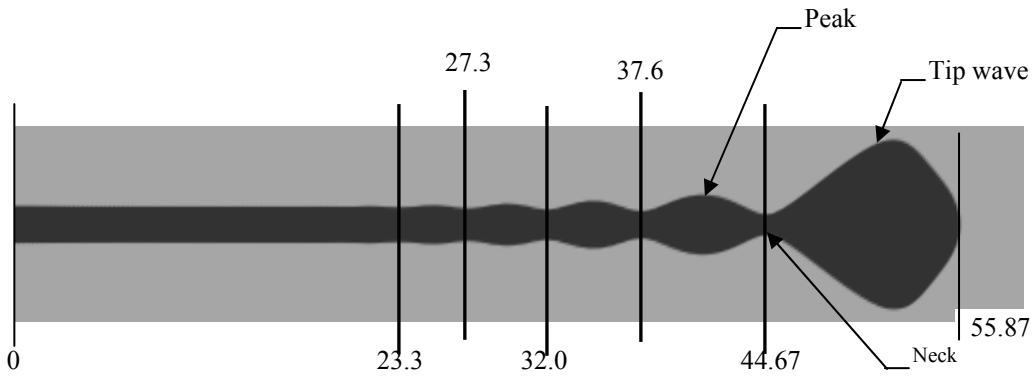

Fig.3 Non-dimensional position of capillary waves at time, t =36.18

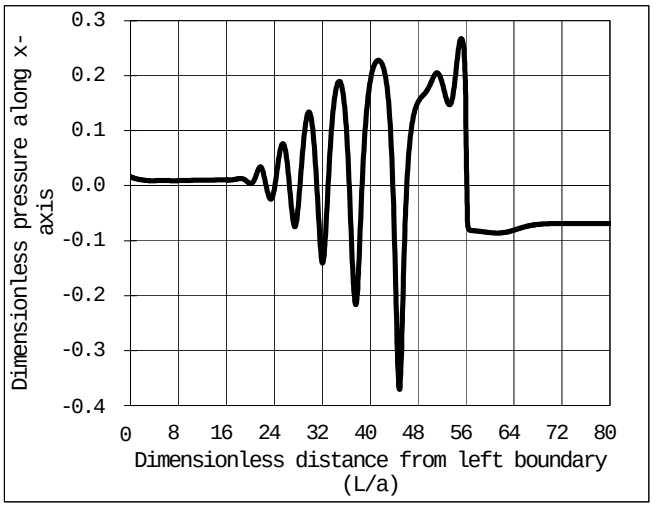

Fig.4 Dimensionless pressure distribution along the horizontal axis of the liquid sheet at time, t = 36.18

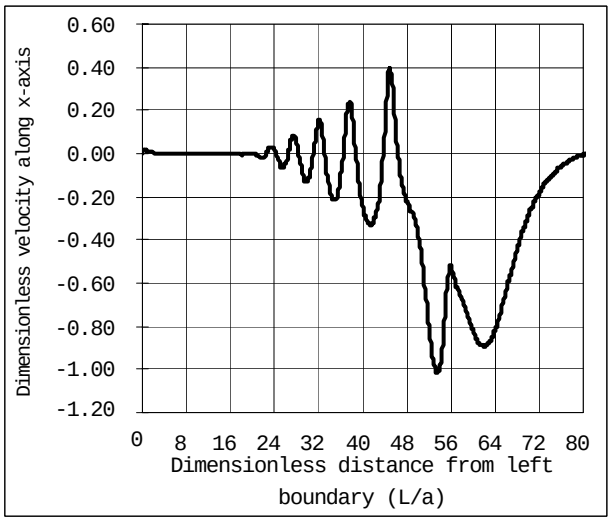

Fig.5 Dimensionless horizontal velocity distribution along the horizontal axis of the liquid sheet at time, t = 36.18

Figure 4 shows the variation of non-dimensional pressure along the horizontal axis (x-axis) of the liquid sheet. In this study x-axis indicates the axis which lies on the mid-section of the unperturbed sheet thickness. The pressure is made dimensionless by σ/a. The pressure at different position of capillary waves can be understood from this figure. From Fig.4 it can be understood that the pressure is high at the peaks and low at the necks. The wave at the tip shows the highest pressure and gradually the peak values of both high and low pressures decrease in the waves away from the tip wave. Two effects of surface tension on pressure can be observed, which can be explained by considering the Fig.4. At the necks, the direction of surface tension force is toward the outside of the liquid, which causes low pressure. At the peaks, the surface tension force is activated toward inside of the liquid which causes high pressure. Figure 5 shows the distribution of dimensionless horizontal velocity (velocity towards right or left) on x-axis of the liquid sheet. Dividing the actual velocity by square root of$\sigma/(\rho_l\ a)$, the horizontal velocity is made dimensionless. The velocity towards right is considered as positive and that towards left is considered as negative. From Fig.5 it can be found that the velocity increases at both of peaks and necks, but in opposite direction, which means that the peak value of positive direction occurs at the necks and that of negative direction occurs at the peaks of the waves. The highest peak velocity towards negative direction occurs in tip wave, which is caused by the surface tension force and the effect of liquid sheet contraction. The local

increase of the liquid velocity observed immediately near the tip expresses an effect of tip bulb oscillation. Thus, the actual contraction speed of liquid sheet tip should be identified with the minimum value, which is equal to unity in dimensionless speed.

However, from the above results the phenomena of the formation of capillary wave and its propagation can be understood during the contraction of liquid sheet in a still, quiescent and viscous gas medium. It can be found that within dimensionless time, t=36.18 five complete capillary waves are generated on the liquid surface. Within this time, the amplitude of the tip wave becomes so large that the diameter of the tip swell becomes 9.87 times larger than the half-thickness of the unperturbed liquid sheet and no liquid disintegration can be observed. Therefore, from this investigation two observations can be summarized: (1) The surface tension, activated on the liquid, forms capillary waves on the liquid surface, and (2) Only the surface tension can not disintegrate the liquid sheet. However the surface tension and the capillary waves play an important role to occur the disintegration of liquid sheet, which will be discussed in the next investigation.

5. CONCLUSIONS

A numerical investigation is performed to study the characteristic phenomena of capillary wave on the surface of liquid sheet. It is found that the capillary wave is formed by surface tension force initiated at the tip of the sheet. The rectangular shape of tip is transformed into a triangular shape and the capillary waves are formed with a bulbous end. The capillary wave propagates with an asymptotic approach along the height of wave peaks from the longitudinal axis of the sheet. The formation of following waves takes shorter interval of time than that of its former wave and also the wavelength of the propagating waves becomes shorter than that of the previous one. Pressure along the longitudinal axis depends on the surface tension and radius of curvature at the peak and trough of the waves. The peak of both low and high pressures occurs at the position of troughs and peaks, respectively. Reverse trend on the distribution of horizontal velocity along the longitudinal direction can be found, which shows that the peak value of horizontal velocity in positive direction occurs at the troughs and that in negative direction occurs at the peaks of the wave. Both the peak values of pressure and velocity decrease with the decrease of wave amplitude by increasing the radius of curvature and passage of liquid flow to satisfy the conservation law of mass. The long time calculation shows that only surface tension can not disintegrate the liquid sheet.

6. REFERENCES

[1] Gueyffier, D., Li, J., Nadim, A., Scardovelli, R. and Zaleski, S. Volume-of-Fluid Interface Tracking with Smoothed Surface Stress Methods for Three-Dimensional Flows, *J. Computational Physics,* 152 (1999), pp. 423-456.

[2] Brackbill, J. U. Kothe, D. B. and Zemach, C. A Continuum Method for Modeling Surface Tension, *J. Computational Physics,* 100 (1991), pp. 335-354.

[3] Welch, S. W. J. and Wilson, J. A Volume of Fluid Based Method for Fluid Flows with Phase Change, *J. Computational Physics,* 160 (2000), pp. 662-682.

[4] Rayleigh, L. On the Capillary Phenomena of Jets, Proceedings of the Royal Society of London, 29 (1879), pp. 71-97.

[5] Goedde, E. F. and Yuen, M. C. Experiments on Liquid Jet Instability, *J. Fluid Mech.*, 40, part 3 (1970), pp. 495-511.

[6] Donnelly, R. J. and Glaberson, W. Experiments on the Capillary instability of a liquid Jet, Proceedings of the Royal Society of London, Series A, 290 (1966), pp. 547-556.

[7] Stone, H. A., Bently, B. J. and Leal, L. G. An Experimental Study of Transient Effects in the Breakup of Viscous Drop, *J. Fluid Mech.*, 173 (1986), pp. 131-158.

[8] Stone, H. A. and Leal, L. G. Relaxation and Breakup of an Initially Extended Drop in an Otherwise Quiescent Fluid, *J. Fluid Mech.*, 198 (1989), pp. 399-427.

[9] Umemura, A. and Wakashima, Y. Atomization Regimes of a Round Liquid Jet with Near-Critical Mixing Surface at High Pressure, Proceedings of the Combustion Institute, 29 (2002), pp. 633-640.

Proceedings of the 4th BSME-ASME International Conference on Thermal Engineering
27-29 December, 2008, Dhaka, Bangladesh

MIXING CHARACTERISTICS IN TWO-DIMENSIONAL NON-PARALLEL STREAMS

Mohammad Ali*[1], S. Islam*[1], G. Saha*[2] and A K M Sadrul Islam*[3]

*[1] Department of Mechanical Engineering, BUET, Dhaka, Bangladesh
*[2] Department of Mathematics, Dhaka University, Bangladesh
*[3] Department of Mechanical and Chemical Engineering, IUT, Gazipur, Bangladesh
email: mali@me.buet.ac.bd

ABSTRACT

A numerical investigation has been performed to study the mixing characteristics of two non-parallel streams of hydrogen and air, behavior of the flow field on mixing, and flame holding capability of a supersonic combustor. The merging angles of two non-parallel streams are varied from 10˚ ~ 50˚. The flow fields are investigated by solving Two-Dimensional Navier-Stokes equations. An explicit Harten-Yee Non-MUSCL Modified-Flux-Type TVD (Total Variational Diminishing) scheme has been used to solve the system of equations, and a zero-equation algebraic turbulence model proposed by Baldwin and Lomax has been used to calculate the eddy viscosity coefficient. To delineate the purely fluid dynamic effects, the flow has been treated as non-reacting. It has been seen that recirculations and penetration of hydrogen play an important role to enhance mixing. The area of recirculation decreases with the increase of merging angle but mixing efficiency increases. The recirculation regions and several shocks such as expansion shock, recompression shock and reattachment shock in the flow field are evident.

KEYWORDS: *Mixing, Merging angles, Non-parallel streams, Flame holding, Supersonic combustor.*

1. INTRODUCTION

Mixing process plays a vital role in flow field of many engineering applications e.g. combustion chambers, pre-mixers for gas turbine combustors, chemical lasers, propulsion systems and flow reactors. In supersonic combustor, the flow speeds are very high and mixing of injectant with mainstream is difficult due to their short residence time. A considerable number of researches have been carried out on mixing and combustion of fuel with supersonic air stream for the last three decades. In recent development of efficient Supersonic Combustion ramjet (Scramjet) engines and advanced airspace propulsion system, there is renewed interest in the study of turbulent mixing layers. The turbulent mixing layer, which forms at the interface between two uniform streams of different velocity, develops through two successively distinct regions. Unfortunately, the growth rate of mixing layer in two supersonic streams is considerably smaller than that of two subsonic streams. Brown and Roshko [1] showed that the spreading rate of supersonic mixing layer decreased drastically with increasing of free stream Mach number. Though a considerable number of researches have been carried out on mixing and combustion of fuel with supersonic air stream, still it faces many unsolved problems. The main problems that arise in this regard concern mixing of reactants, ignition, flame holding and completion of combustion. To overcome these problems more investigations are required on supersonic mixing phenomena.

Several studies have been performed to analyze the mixing, combustion characteristics and mixing efficiency in supersonic or subsonic flows. Azim and Islam [2] showed that the mixing layers decreased in growth with increasing velocity ratio and mixing layers from non-parallel merging streams (18°) were found to have higher growth in the near-field than those from parallel merging streams. Recirculation formed behind the base or step can enhance mixing and flame holding capability. Ali et al. [3-4] and Ahmed et al. [5] studied the mixing mechanisms and

investigated mixing and combustion characteristics for several flow configurations. On the analysis of mixing the author observed that the backward-facing step in finite flow configuration plays an important role to enhance mixing and penetration in both upstream and downstream of injector. There exist several methods of fuel injection in the supersonic air stream. Perpendicular injection causes rapid fuel-air mixing whereas parallel injection is used when slow process is desired, especially at lower speed of space vehicles. In parallel injection, mixing occurred due to molecular diffusion at the interface of two flows [6-7]. The mixing layer from non-parallel merging streams has higher growth than that from parallel merging streams.

Hydrogen is well known as the most suitable fuel for propulsion systems. Because of the high speed of the air stream, a reasonable length is needed for the combustor. So it is difficult to perform the experimental study under the supersonic combustion because of high cost. Therefore, the numerical research is quite important. There is no available information about the effect of air-hydrogen non-parallel streams behind a base which is shown in this paper.

2. MATHEMATICAL MODELING

The unsteady, two-dimensional full Navier-Stokes and species continuity equations have been solved to analyse the mixing flow field of hydrogen and air. These equations can be expressed by

$$\frac{\partial \mathbf{U}}{\partial t} + \frac{\partial \mathbf{F}}{\partial x} + \frac{\partial \mathbf{G}}{\partial y} = \frac{\partial \mathbf{F}_v}{\partial x} + \frac{\partial \mathbf{G}_v}{\partial y}$$

where, $\mathbf{U} = [\rho,\rho u,\rho v,E,\rho Y_i]^T$, $\mathbf{F} = [\rho u,\rho u^2+p,\rho uv,(E+p)u,\rho Y_i u]^T$, $\mathbf{G} = [\rho v,\rho uv,\rho v^2+p,(E+p)v,\rho Y_i v]^T$,

$\mathbf{F}_V = [0,\sigma_x,\tau_{xy},\sigma_x u + \tau_{yx} v + q_x,\dot{m}_x]^T$, and $\mathbf{G}_V = [0,\tau_{yx},\sigma_y,\tau_{xy} u + \sigma_y v + q_y,\dot{m}_y]^T$.

The details of equations and the calculation of its different parameters are shown by Ali [3]. The fluid dynamics is solved using an explicit Harten-Yee Non-MUSCL Modified-flux-type TVD scheme proposed by Yee [8]. The thickness base creates recirculation and turbulence in the flow field. These recirculations, shocks, and expansion of both streams lead us to use a turbulence model. Therefore, to calculate eddy viscosity we selected zero-equation turbulence model proposed by Baldwin and Lomax [9].

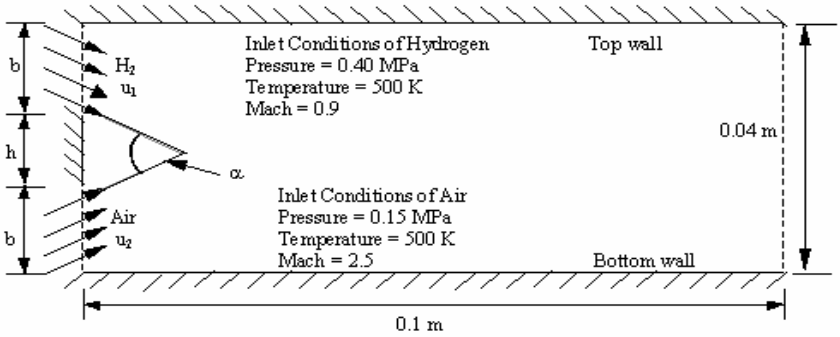

Fig.1 Schematic with numerical parameters (Merging angle, $\alpha=10^0, 20^0, 30^0, 40^0$ & 50^0; Base height, h = 0.01 m and Inlet width, b = 0.015 m)

3. RESULTS AND DISCUSSION

The present work is a part of investigation conducted by Islam [10]. The geometric configuration of the calculation domain and the inlet condition of two non-parallel streams are shown in Fig.1. Air having Mach number 2.5 enters into the domain through the lower part of the left boundary and hydrogen having Mach number 0.9 enters through the upper part of the left boundary. The flow domain is assumed open to the right. A Navier-Stokes analysis imposes that the normal and tangential velocity components are zero on the walls. The walls are assumed to be thermally adiabatic. For non-catalytic walls, the normal derivative of species mass fraction also vanishes, and consequently the gradient of total density becomes zero. The pressure is determined from the equation of state. The

temperature, pressure and density at inflow boundary are assumed steady. Uniform velocities are used at inflow boundary. At outflow boundary, zero gradients of all variables are assumed. The merging angle, α is varied from 10˚ ~ 50˚ defined as Case 1 (α = 10˚), Case 2 (α = 20˚), Case 3 (α = 30˚), Case 4 (α = 40˚) and Case 5 (α = 50˚). Some features of this kind of flow field are shown in Fig. 2. It predicts the expansion at the separation points, formation of a recirculation regions bounded by two shear-layer mixing regions, recompression and reattachment shock, and boundary layer as well as shear layer.

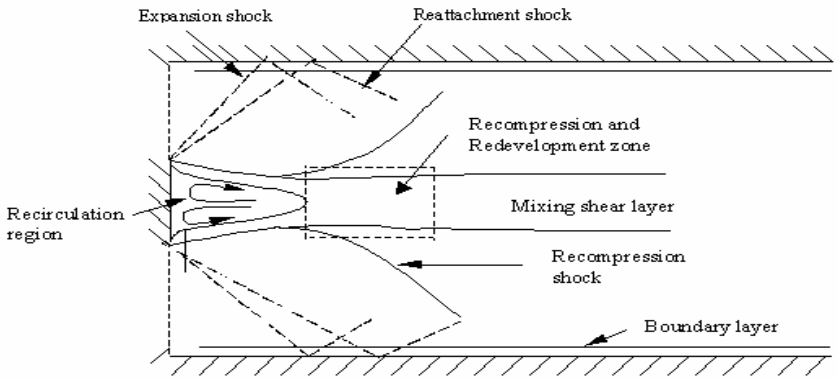

Fig. 2 Flow field features behind a thickness base.

Figure 3(a-e) shows the velocity vectors of the flow field, where the flows expand sharply around the base corner and produce a separation region behind the base. Both hydrogen and air streams move to each other and strike behind base at about 0.02 m from the bottom wall. After striking, hydrogen deflects upward and air deflects downward sharply. Again they strike the upper and lower walls and then reflect. There is a pair of recirculation region behind the base. The upper recirculation rotates clockwise while the lower recirculation rotates counter clockwise. The flows expand sharply around the base and the interaction of both shear layers occurs in the low velocity regions. Due to interaction between two streams, the velocity of the streams is slowed down and both hydrogen and air enter in recirculation regions and hydrogen mixes with air by diffusion and convection in recirculation. So recirculation plays a vital role on the mixing. The shear layer mixing regions spread with longitudinal distance after impingement of the streams and recovery of the wake deficit begins. The distance of impingement point from the left wall decreases with the increase of merging angle, which indicates smaller recirculation zones.

Figure 4(a~e) shows mole fraction contours of hydrogen in the flow field. The concentration ratio shows the growth of mixing layer. It can be seen from Figs.4(a~e) that the mixing layers grow along the flow direction. Penetration and mixing of hydrogen with air can occur by means of (i) strong interaction occurred in the low velocity regions of both shear layers, (ii) turbulence and convection due to recirculation and velocity of the flow, and (iii) molecular diffusion. For all cases (1~5), mole fraction contours show that the mixing layer is relatively narrow in width at interaction region. The width of the mixing layer is defined as the thickness of 5% to 100% concentration of hydrogen. At far downstream the thickness of mixing layer increases with the increase of merging angles. As the flow in lower part is air and in upper part is hydrogen, the significant density gradient exists at the interface of two streams and hydrogen mixes with air in one interface. In this work, there is a pair of recirculations behind the base discussed earlier. Out of these two, the upper one contains high concentration of hydrogen (mole fraction is about 0.85~0.95) due to the convection and expanded flow of hydrogen. On the other hand, in lower recirculation region, hydrogen mixes with air by convection and diffusion processes. This region contains better proportion of hydrogen, which is capable of burning. Longer recirculation zone containing stoichiometric mixture strength results in a longer residence time of flow and leads to a more stable flame. Therefore, flame holding capability is better for case1 than others. However, the larger reciculation region does not mean higher mixing efficiency. Figure 5 shows the mixing efficiency at the outflow boundary. It can be found that mixing efficiency increases with increasing merging angle up to 40^0 and then decreases sharply.

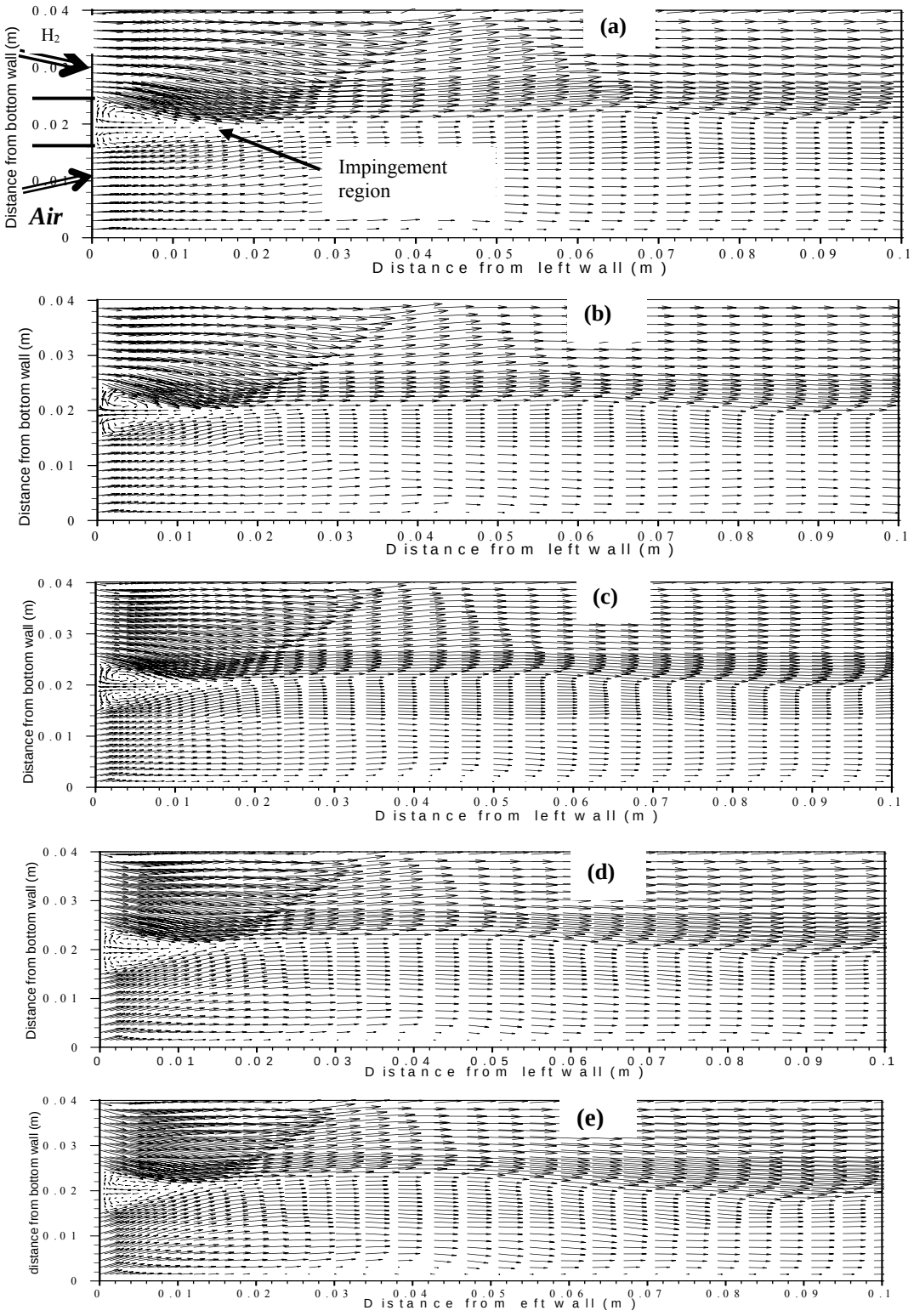

Fig. 3 Velocity vector field of two streams; (a) Case 1, (b) Case 2, (c) Case 3, (d) Case 4 and (e) Case 5

The pressure at different region such as the recirculation, recompression, redevelopment and reattachment process can be clearly seen by the profile of static pressure along a centerline extending downstream from the vertical center of the base as shown in Fig. 6. The static pressure is non-dimensionalized by the inlet pressure of air and the streamwise distance is non-dimensionalized by the value of base height. Figure 6 indicates the low pressure in the recirculating region just behind the base and strong pressure rise during the recompression and

impingement processes. Far away from the left wall, the pressure is low and shows wavy nature with small amplitude.

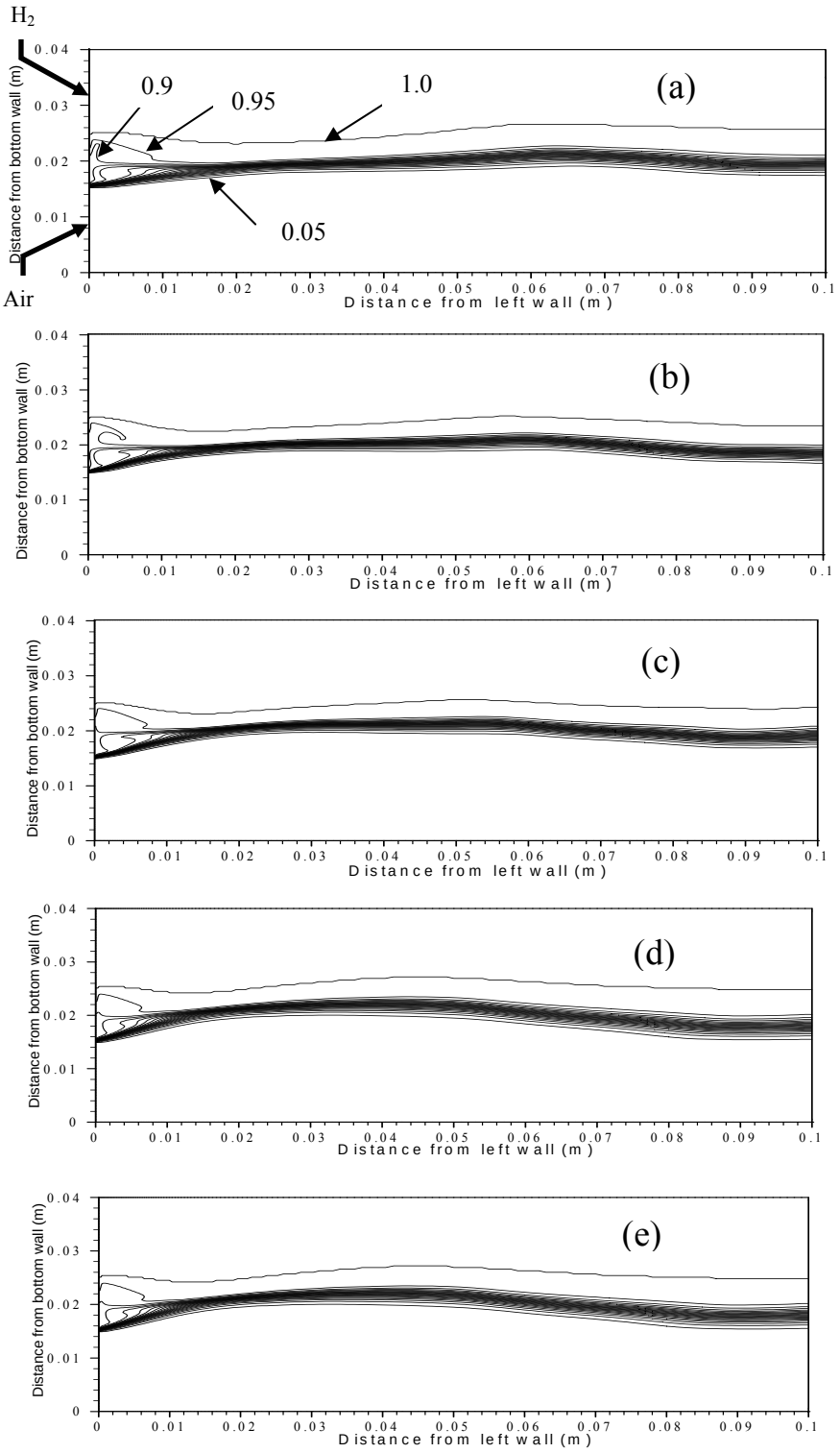

Fig.4 Mole fraction contour of hydrogen, φ (0.05,1.0,0.05); (a) Case 1, (b) Case 2, (c) Case 3, (d) Case 4 and (e) Case 5.

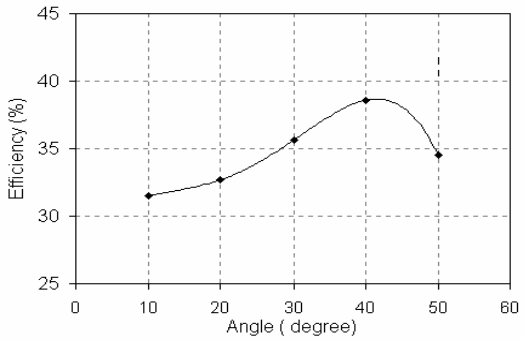

Fig. 5 Variation of mixing efficiency with merging angle.

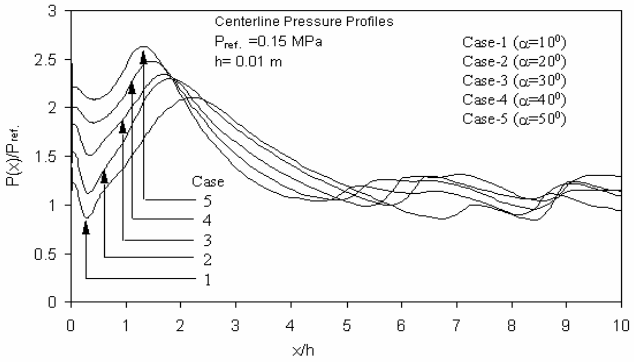

Fig. 6 Centerline pressure of the flow field

4. CONCLUSIONS

This study has been performed to investigate characteristics of mixing and physics of fluid dynamics in two non-parallel streams by varying merging angle. It is found that interaction between air and hydrogen becomes stronger with the increase of merging angle but the area of recirculation region decreases. The increasing rate of mixing efficiency behind the base is high and then it is very slow. For 40^0 merging angle, the mixing efficiency is high but the flame holding capability is comparatively low. For high merging angle (50^0), both the mixing efficiency and flame holding capability are low. Out of two recirculations, the lower recirculation region contains better proportion of hydrogen and air. The flows expand sharply around the base and interactions occur between flows and recirculations. Consequently, high mixing occurs due to convection and diffusion behind the base.

5. ACKNOWLEDGEMENT

The authors are grateful to Bangladesh University of Engineering and Technology (BUET), Dhaka, Bangladesh to provide computation facilities this research and other financial support for this research.

6. REFERENCES

[1] Brown GL and Roshko A, On Density Effects and Large Structure in Turbulent Mixing Layer. *J. Fluid Mechanics*, 64 (4) (1974), pp. 775-816.

[2] Azim, M. A., and Sadrul Islam A. K. M., Plane Mixing Layers From Parallel and Non-Parallel Merging of Two Streams, *Experiments in fluids,* 34 (2003), pp. 220-226.

[3] Ali, M, Fujiwara, T and Leblanc, J. E., The Effects of Backward-Facing Step on Mixing and Flame Holding in Supersonic Combustor, *J. of Energy, Heat and Mass Transfer*, 23(2001), pp. 319-338.

[4] Ali, M, Fujiwara, T and Pervez, A., A numerical study on the physics of mixing in two-dimensional supersonic stream, *Indian Journal of Engineering and Materials Sciences*, 9 (2002), pp. 115-127.

[5] Ahmed, S, Ali, M and Sadrul Islam, AKM., The Effect of Injection Angle on Mixing and Flame Holding in Supersonic Combustor, *Int. J. of Thermal and Fluid Sciences*, 11 (1) (2002), pp. 80-91.

[6] Umeda, Y., and Fujiwara, T., Physics of Methane Combustion in Mixing Shear Layer, *Trans. Japan Soc. Aero. Space Sci.*, 38(121) (1995), pp. 265-281.

[7] Gerlinger, P., Algermissen, J., and Bruggemann, D., Numerical Simulation of Mixing for Turbulent Slot Injection, *AIAA Journal*, 34 (1) (1996), pp. 73-78.

[8] Yee HC, A Class of High-Resolution Explicit and Implicit Shock Capturing Methods, NASA TM - 101088, 1989.

[9] Baldwin BS and Lomax H, Thin Layer Approximation and Algebraic Model for Separated Turbulent Flows, *AIAA Paper 78-257*, 1978.

[10] Islam, T. M. S., Flow Field Behind A Finite-Thickness Base in Two Non-Parallel Streams. M. Sc. Engg. Thesis, Bangladesh University of Engineering and Technology, 2005, Dhaka, Bangladesh.

Proceedings of the 4th BSME-ASME International Conference on Thermal Engineering
27-29 December, 2008, Dhaka, Bangladesh

AERODYNAMICS OF TIME TRIAL BICYCLE HELMETS

Firoz Alam, Andrew Knight and Aleksandar Subic

School of Aerospace, Mechanical and Manufacturing Engineering, RMIT University, Melbourne, AUSTRALIA

E-mail: firoz.alam@rmit.edu.au

ABSTRACT

The aerodynamic efficiency becomes essential design criterion for time trial bicycle helmets as time differences of seconds can make the winner. Although numerous manufacturers market time trial helmets, the aerodynamic performances of these helmets are not well known. Additionally, no comparative study of aerodynamic performance of various time trial helmets has been reported in the open literature. Therefore the primary objectives of this research were to study the aerodynamic performance of two time trial helmets that currently comply with the Australian safety standards and are used in time trial racing in Australia. The helmets were tested on a mannequin in the time trial head positions over a range of yaw angles and wind speeds. The results indicated that there was a significant variation in aerodynamic performances of these two helmets. However, their performances varied depending on yaw and pitch angles.

Keywords: *Time trial helmets, aerodynamic drag, yaw angle, pitch angle*

1. INTRODUCTION

In bicycle racing, aerodynamics play a vital role as every second can make the difference between the winners and losers. At around 30 km/h speed, the aerodynamic resistance (drag) constitutes almost 80 percent of total resistance (remaining 20% is rolling resistance) [2, 3]. Out of total aerodynamic drag, the rider position counts approximately 65 to 80 percent depending on body position, helmet and clothing. The remaining drag is coming from bicycle frames, wheels (mainly front wheels) and other components and adds on [6]. Although, the percentage of aerodynamic drag from the helmet is approximately 2 to 8 percent depending on the aerodynamic shape of the helmets at around 30 km/h cruising speeds, the use of an aerodynamically efficient helmet can play an important role by making an advantage be at racing or recreational riding.

It is no doubt that selecting appropriate helmets and maintaining correct body position, a cyclist can reduce aerodynamic drag significantly and the conserved energy can be put into the pedalling at appropriate stages of the racing. Some years ago, the renowned cyclist Greg Lemond trailed French rider Laurent Fignon by 50 seconds prior to the final stage of a 24.5 km individual time trial racing event in 1989. Although the 50 seconds gap is negligible as Lemond required riding each kilometre distance by only 2 seconds faster than his competitor Fignon. Nevertheless, Lemond using an aerodynamically efficient helmet and aerodynamically efficient normal bicycle was able to defeat Laurent Fignon by 58 seconds and subsequently won the Tour by just 8 seconds. It was later revealed that the aerodynamic

drag on Fignon's ponytail alone was enough to slow him down by the critical 8 seconds by which he lost the race. Since long, the aerodynamics played an important role in time trial and road racing competitions around the world.

Although several studies by Alam et al. [2, 3] and Bruhwiler [6] were conducted to measure the aerodynamic drag and temperature measurement techniques for recreational bicycle helmets, little study was conducted on aerodynamics of Time Trial bicycle racing helmets. Although over dozen manufactures market various time trial helmets for the cyclists around the world, most time trial helmets do not comply with the minimum safety standards for head protection as their main purposes are to provide smooth airflow around the cyclist head thus reducing aerodynamic drag. Only a small number of time trial helmets does comply the helmet safety standards. The aerodynamic performances of these commercially available helmets are unknown as limited information is available in the public domain. Additionally, no comparative study of aerodynamic performance of various time trial helmets has been reported in the open literature. Therefore, the primary objectives of this research work as a part of a larger project were to study the aerodynamic performance of two time trial helmets that currently comply with the Australian safety standards and are widely used in time trial bicycle racing in Australia.

2. DESCRIPTION OF HELMETS AND EXPERIMENTAL FACILITIES

As mentioned earlier, currently only two time trial helmets that are commercially available in Australia comply with the Australian helmet safety standards. They are Limar Speed Demon and Crono05 (details will be given later). Limar is an Italy based leading bicycle helmet manufacturer in the world. Other main competitors are LG, Giro and Lazer. The Australian Standards for bicycle helmet safety are one of the toughest in the world. While all competitions held in Australia require the use of helmets, some require that the helmet only comply with UCI (*Union Cycliste Internationale*- cycling's international governing body) regulations, while others specify that the helmet must meet Australian Standards. Participants looking for any small advantage over the competition at elite level in Australia, therefore, require an aerodynamic time trial helmet that meets Australian Standards.

2.1 Time Trial Helmets

2.1.1 Limar Crono05

The Crono05 (Figure 1) is a time trial helmet, targeted at track cyclists. The Crono05 is 33cm long with a mass of 330g and is made of expanded polystyrene foam using in-mould construction techniques.

Internal channels incorporated into the construction of the helmet provide minimal cooling, as there are no-front facing ventilation holes. The channels allow airflow around the bottom edge of the helmet to five vents placed at the rear of the head. The absence of forward facing ventilation improves aerodynamics. The helmet is manufactured in only one size, and Limar's adjustable Super System 2 ensures that the helmet fits all head shapes. The short compact shape is more suited to the changing of body positions which generally occurs at the end of races.

Figure1: Limar Crono05 time trail helmet (Left to Right: front, side, rear & top view)

2.1. 2 Limar Speed Demon

The Speed Demon in Figure 2 features an aerodynamically expanded design, targeting road time trial cyclists and tri athletes (i.e. longer race distances). The Speed Demon is 38.5cm long, weighs 340g and is constructed from expanded polystyrene foam using in-mould construction techniques.

Figure 2: Limar Speed Demon time trail helmet (Left to Right: front, side, rear & top view)

The Speed Demon contains 15 air vents, of which 12 are forward facing. Six of these vents are located on flexible ear coverings, and were used to improve the user's hearing during the cycling as well as provide cooling ventilation. The Speed Demon uses the same Super System 2 fitting as the Crono05.

While these two helmets to be tested are very similar in their basic shape, size and weight (because the same company manufactures them), there are a number of key differences which are likely to demonstrate aerodynamic differences between the two. The Speed Demon is significantly longer than the Crono05 (Figure 3), and uses flexible flaps to improve flow around the ears and side of the head and neck. The Speed Demon is 38.5 cm long while the crono05 is 5.5 cm shorter at 33 cm.

The added length of the Speed Demon was to improve aerodynamics as the shape offers a longer surface for pressure recovery. The longer tail also should bridge the gap at the back of the neck better, further improving the performance of the helmet compared with the shorter, more compact Crono05.

Ventilation is another area of key difference between the helmets. The Crono05 has no forward facing ventilation holes, which should be beneficial to aerodynamic performance.

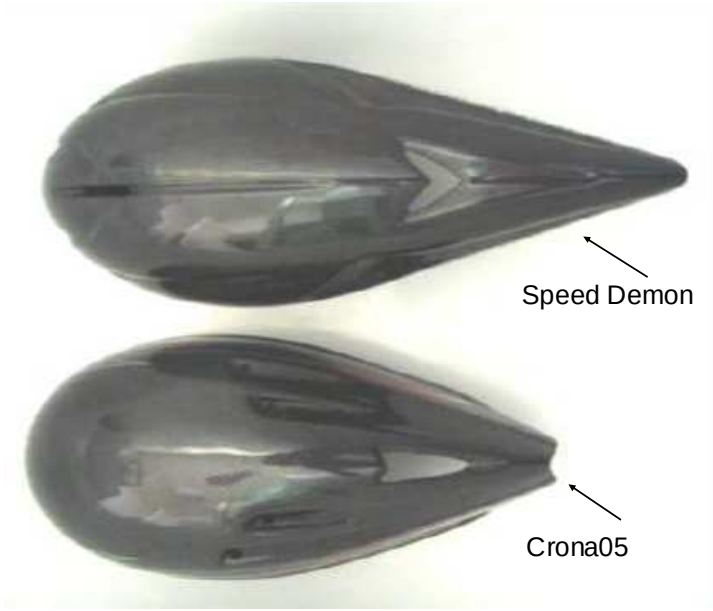

Figure 3: A plan view of Speed Demon and Crona05 helmets

2.2 RMIT Industrial Wind Tunnel and Force Sensor

Aerodynamic forces were measured in RMIT Industrial Wind Tunnel using a six component force sensor type JR3. A plan view of the wind tunnel and JR3 force sensor is shown in Figure 4. The force sensor measures forces and moments in all six degrees of freedom and resolves the forces and moments into the orthogonal aerodynamic co-ordinate system. The unit was rigidly connected to the tunnel turntable so that yaw angle changes could be made without affecting results. Data acquisition was recorded using ten second "snaps." Computer software samples the forces at a frequency of 2000 Hz ensuring electrical interference is minimised. Multiple snaps were collected at each acquisition point and the results averaged, thus further minimising possible errors in the data.

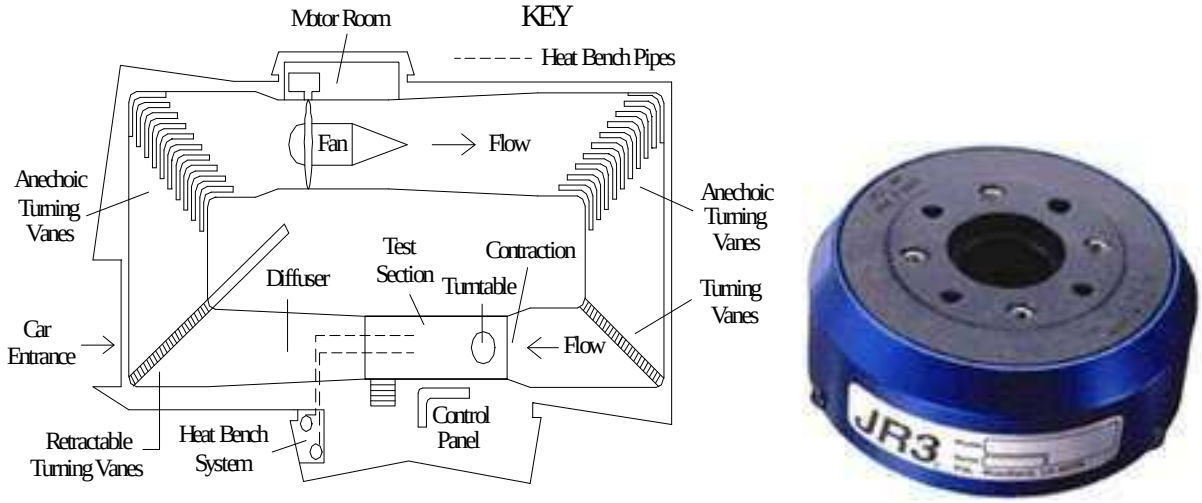

a) Plan view of RMIT Industrial Wind Tunnel

b) JR3 1000N force sensor

Figure 4: A plan view of RMIT Industrial Wind Tunnel and a JR3 1000N force sensor [1]

2.3 Experimental Set Up

A purpose made mannequin was designed and manufactured to simulate the body position and size of a representative road cyclist (see Figure 5). The mannequin body was made by polystyrene foam. Body measurements were taken of male cyclists and the averaged results were used to shape the model.

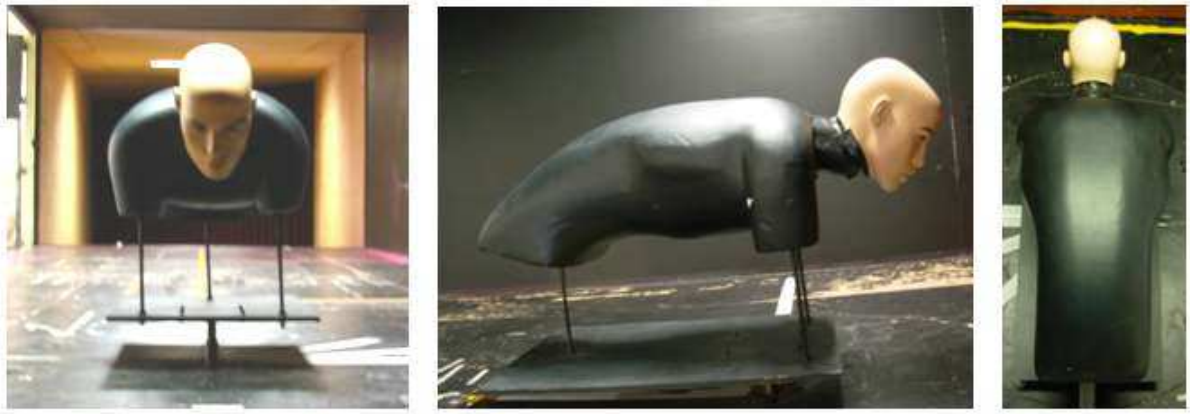

Figure 5: Mannequin mounted in RMIT Industrial Wind Tunnel (Left to Right: Front, Side & Top View)

As depicted in Figure 5, the mannequin was connected to the force sensor via a "sting." The sting is a single metal rod which transfers the generated aerodynamic forces from the mannequin to the force sensor. An adjustable neck has been incorporated into the mannequin to allow for variation in head pitch (head position). Time trial helmets are sensitive to pitch due to their elongated shape, and as such it is important to have the ability to test the effects of pitch on aerodynamics.

3. EXPERIMENTAL PROCEDURE

Each helmet was tested at a range of speeds, yaw angles, and pitch inclines. Testing speeds and angles were based upon the average speeds from both track and road cycling races at the *2008 Beijing Olympic Games*. Speeds of 68 km/h were reached on the track, while the average speed of the winning rider in the Men's road time trial, Fabian Cancellara of Switzerland, was 45.92 km/h. The course at the Olympic Games was not a typical course, so speeds were compared with those of the *2008 Tour de France* and the *2004 Athens Olympic Games*. The winning average speed at the 2004 Olympics in Athens was 50.06 km/h while the winning average speed in the final time trial at the *2008 Tour de France* was 49.82 km/h. Australia has an average wind speed of ~3m/s or 11 km/h (Alam, 2008). This speed equates to a maximum yaw angle of 15.67° at 40 km/h. This maximum reduces as cyclist speed increases and at 70 km/h the max yaw angle is 8.88°. Head pitch, and therefore, the helmet pitch, was varied to reflect different postures of bike riders. A pitch of 40° from vertical assumed to be the "normal" position and this point was assigned the zero pitch point for testing. The helmets were tested at three different pitch angles (0°, 15° and 30°) as shown in Figure 6. Prior studies showed that Time Trial helmets, relatively insensitive to pitch angles up to +20° but become increasingly sensitive once this pitch is surpassed [4].

Each helmet was tested at speeds ranging from 40 km/h to 70km/h with an increment of 10 km/h. At each speed increment the test apparatus (mannequin and helmet) was rotated between yaw angles of ±20° in an increment of 5° to simulate the crosswind effects. The head

pitch was altered between 0°, +15° and +30° in increments from the initial 40° position as shown in Figure 6. These test conditions best simulate the types of speeds and wind directions experienced by a cyclist during a race in the real world. This set of tests yields 108 data collection points per helmet.

Figure 6: Pitch inclinations used during testing. (Left to Right: 0° [Initial], 15° & 30°)

3.1 Flow Visualisation

Flow visualisation around the helmets and mannequin was conducted using smoke trail and wool tuft. Smoke stream testing was conducted at 10 km/h wind speed as the speed of high velocity flows dissipates the smoke too quickly and streamlines cannot be observed. The other flow visualisation technique used during testing was wool tufts attached to the surface of the helmets. Wool tufts are a useful visualisation technique as flow patterns can be observed at high speeds. Wool tufts offer a more dynamic visualisation technique and flow patterns and separation points can more easily be depicted. Figure 7 shows smoke and wool tuft flow visualisation around the helmets.

a) Flow visualisation with smoke b) Flow visualisation with wool tuft

Figure 7: Airflow visualisation around the helmet

4. RESULTS AND DISCUSSIONS

The aerodynamic drag (force) acting on the cyclist is dependant on the yaw angle of the relative wind direction. Figure 8 indicates how drag force changes in relation to yaw angle (Ψ°). Drag force decreases with increasing yaw angle. This decrease is due to decreasing frontal area of the mannequin. Drag force decreases rapidly between 0° to 5° due to the significant reduction in model frontal area. The neck/shoulder area is therefore key to drag reduction, as at 0° yaw, this area is unavailable to the flow due to head position, but with

greater yaw angle, this area becomes increasingly important. Figure 8 also demonstrates how each test run of the helmet influences the flow in comparison with baseline measurements (naked head and torso). It can be seen that the naked head and torso is extremely sensitive to yaw angle. All helmets reduce drag at 0° yaw. This is because at 0°, the pressure recovery of the helmet tail reduces the wake region and delays flow separation. Thus, the drag force decreases. Generally, helmet increases drag force at high yaw angles (Ψ>12°) due to increased frontal area facing the wind. The absence of a helmet allows the fluid to flow around the neck, between the head and shoulders, but the helmet tail fills this gap and redirects flow at high yaw angles. The distinct pressure recovery benefits at low yaw angles (Ψ<7°) make drag force to increase at high yaw angle as flow direction is more likely to be at small yaw angles. The time trail helmets are sensitive to pitch angle variation. In racing, the pitch angle changes are common as rider body position changes are likely and to cause some forms of pitch alteration. Riders commonly pitch their head down at the end of race due to exhaustion, thinking that it will decrease the frontal area, therefore the drag. The results presented here show this is untrue, especially when wearing an elongated time trail helmet.

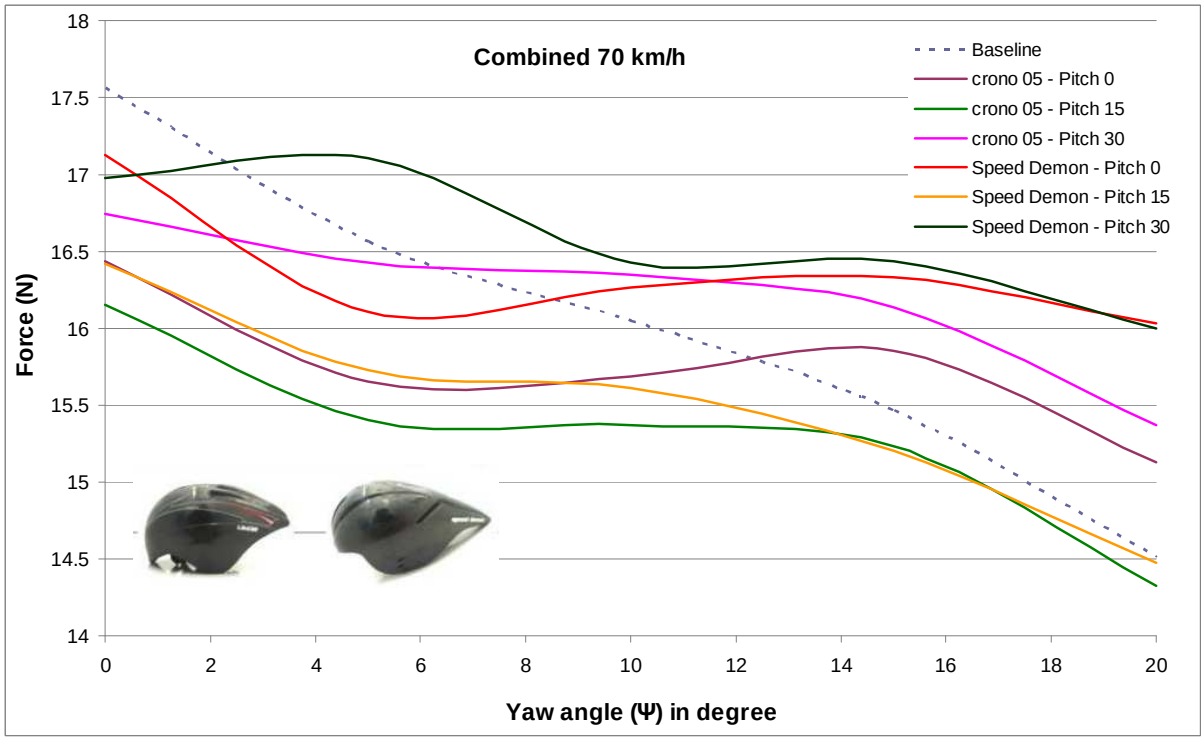

Figure 9: Aerodynamic force variation with yaw and pitch angles at 70 km/h

The percentage of aerodynamic drag (force) reduction for each test over baseline measurements is shown in Table 1. The table shows that all helmets provide savings at 0°, with the average saving being a force reduction of 4.8%. Conversely, all helmet tests increase drag forces at maximum yaw angle with an average increase of 5.88%.

Due to its compact design, the Crono05 provided the biggest overall savings. For optimal performance, the best pitch inclination (head position) was found to be 55° from vertical (15° setting). These savings were particularly evident at high yaw angles, meaning this should be the helmet of choice in windy conditions, especially if prevailing crosswinds are expected. The absence of forward facing ventilation holes is another contributing factor to the benefits of the Crono05.

The second biggest savings came from the Speed Demon, also at 15° test inclination. These two tests were the only ones to provide overall savings. This demonstrates the importance of generating parallel flow over the torso region. This result also exhibits the necessity of testing helmets as part of a system, as "head-on-stick" tests would produce noticeably different results.

Table 1: Percentage of aerodynamic force reduction over baseline

All Tests							
	crono05			Speed Demon			
Ψ°	0°	15°	30°	0°	15°	30°	Average
0	-4.92%	-7.18%	-4.89%	-1.81%	-6.55%	-3.45%	-4.80%
5	-2.20%	-4.03%	1.38%	-0.57%	-3.17%	4.79%	-0.63%
10	0.86%	-1.83%	3.98%	3.77%	-0.84%	2.75%	1.45%
15	5.23%	0.82%	5.22%	7.80%	-0.71%	4.63%	3.83%
20	7.54%	0.69%	7.55%	12.83%	0.28%	6.40%	5.88%
Average	1.30%	-2.31%	2.65%	4.41%	-2.20%	3.02%	

5. CONCLUSIONS

The following conclusions are made from work presented here:

Both helmets, under all test conditions, provided aerodynamic savings at 0° yaw angles. This proves that in still air conditions, or enclosed venues (velodromes), all helmets will reduce overall aerodynamics drag resulting in improved performance.

Optimal pitch settings were able to generate aerodynamic savings in excess of 7% over baseline measurements

The optimal helmet for use in all conditions was found to be the Crono05 at a pitch inclination of 15°. This helmet and head position produced an average 2.31% reduction of the aerodynamic drag force.

The least favourable performing helmet was found to be the Speed Demon at either 0° (an increase of 4.41%) or 30° (an increase of 3.02%) head pitch (head position).

Flow visualisation illustrated that flow separation was likely to occur in close proximity to ventilation holes. Wool tufts illustrated the high flow turbidity occurring along the helmet edges and tail section. Wool tufts also demonstrated the movement of flow separation lines at high Yaw angles.

6. RECOMMENDATION FOR FUTURE WORK

Future research could focus on the following:

As the tail of time trial helmets is highly sensitive to head pitch, the design of a flexible tail could be investigated. The flexible tail should be rigid enough to resist flow angularity, but

flexible enough to bend under aerodynamic forces. A flexible tail may also improve crash safety. A snap-off tail could also be investigated to improve crash safety.

The effects of hair length on both aerodynamic and thermal performance of a helmet can be investigated. The optimisation (aerodynamically and thermally) of vent placement for road/recreational helmets is another possible avenue of investigation.

The affects of visors on aerodynamic performance of time trial helmets could also be investigated. The international version of the Speed Demon helmet used in this project comes with an incorporated visor, and the possible aerodynamic benefits of such arrangement could be explored. The forward facing vents on the Speed Demon could be covered and compared with results of the crono05 to substantiate the claimed benefits of longer helmet

REFERENCES

[1] Alam, F., Subic, A., Watkins, S., Naser, J. and Rasul, M. G., An Experimental and Computational Study of Aerodynamic Properties of Rugby Balls, *WSEAS Transactions on Fluid Mechanics*, Vol. 3 (3), pp 279-286, 2008

[2] Alam, F., Subic, S., Akbarzadeh, A. and Watkins, S., "Effects of Venting Geometry on Thermal Comfort and Aerodynamic Efficiency of Bicycle Helmets", in *The Impact of Technology on Sport II* (edited by F. K. Fuss, A. Subic and S. Ujihashi), pp 773-780, ISBN 978-0-415-45695-1, Taylor & Francis, London, 2007.

[3] Alam, F., Subic, A. and Watkins, S., "A Study of Aerodynamic Drag and Thermal Efficiency of a Series of Bicycle Helmets", *Proc. of the 6th International Conference on Engineering of Sports*, ISEA, 11-14 July, 2006, Munich, Germany

[4] Booth, A., 'Aerodynamic Efficiency and Thermal Performance of Bicycle Helmets,' Final Year Project, RMIT University, Melbourne, Australia, 2007

[5] Brühwiler, P. A., Buyan, M., Huber, R., Bogerd, C. P., Sznitman, J., Graf, S. F. and Rosgent, T., 'Heat transfer variations of bicycle helmets,' Journal of Sports Sciences, Vol 24 (9), pp 999-1011, 2006

[6] Kyle, C & Bourke, E. 'Improving the racing bicycle', Mechanical Engineering, Vol. 106 (9), pp 34-35, 1984

Proceedings of the 4th BSME-ASME International Conference on Thermal Engineering
27-29 December, 2008, Dhaka, Bangladesh

CONJUGATE CONDUCTION-CONVECTION ANALYSIS OF FINNED TUBE ANNULUS IN LONGITUDINAL LAMINAR FLOW

Muhammad Sohail[1], Syed Muhammad Fakhir Hasani[2*],
[1]Department of Materials and Metallurgical Engineering
[2]Department of Mechanical Engineering
N.E.D. University of Engineering and Technology
Karachi-75270, Pakistan
msohailhanif@yahoo.com
[*]fhasani@neduet.edu.pk

ABSTRACT

Numerical investigation of double pipe heat exchanger with circumferential fins in longitudinal laminar flow is carried out to study the effect of fin pitch-to-height (P/H) ratio on heat transfer and fluid flow characteristics at various Reynolds numbers, using water as working fluid. Systematic analysis is carried out by changing geometric and flow parameters. Geometric parameters include varying the pitch-to-height ratio from 0.55 to 26.4 while for the flow parameters Reynolds number is varied from 200 to 1400. Results obtained are compared with finless tube of same inner and outer diameters. It is found that fins produce a remarkable local increase in heat transfer at fin walls but due to flow recirculation caused by the fins heat transfer decreases from tube walls and therefore addition of fins does not always guarantee heat transfer enhancement. Net heat transfer increases of twenty five percent and pressure drop increases of eighty percent are observed. At low pitch to height ratios fin tip has a larger contribution of about sixty percent of total heat transfer.

Key words: Computational Fluid Dynamics (CFD), Heat Transfer, Finned Tube, Annulus

1. INTRODUCTION

The heat transfer performance of double pipe heat exchangers can be improved by incorporating extended surfaces to the outer surface of inner pipe. A large variety of geometries are available that are used as extended surfaces for example longitudinal fins, spiral fins, wavy tubes, etc. The literature dealing with circumferential finned tube in longitudinal flow is limited. In 1950, Kundsen and Katz [1] published their results for heat transfer and pressure drop in finned tube annuli with water as flowing fluid. Obremeier and Schaiber [2] and Obremeier and Henne [3] experimentally investigated heat transfer and fluid flow characteristics of tube with circumferential fins in longitudinal flow and they suggested that the geometry may be useful for high performance heat exchangers. Geiger and Mandal [4] experimentally investigated the heat transfer and friction factors of high Prandtl number fluids using fins of both conductive and non-conductive materials with Reynolds numbers less than 500. They found that fins of conductive nature were more efficient than non-conductive ones. Agrawal and Sengupta [5] studied the effect of geometric and flow parameters on heat transfer and pressure drop in laminar flow with Reynolds number values of less than 1000 by considering periodically fully developed flow in inter-fin space. They suggested that the use of finned tube could only be justified for high Prantdl number fluids. In the present study heat transfer and pressure drop of external circumferential finned tubes is investigated numerically by taking into account both thermally developing and periodically fully developed longitudinal flow conditions.

2. PROBLEM GEOMETRY.

The problem geometry is adapted from the experimental work of Obremeier and Henne [3]. The geometry is shown in Fig. 1. It resembles a double pipe heat exchanger in which a finned tube of copper

is placed in a pipe of larger diameter. In the finned tube only the middle portion of length ‘L’ contains fins of constant thickness and height (hereafter this finned portion will be termed ‘Test Section’) while the rest of the tube is finless at both ends. In the test section, successive fins of constant thickness and height are added to the outer side of inner tube. The distance between fins was changed systematically to study the effect of fin pitch to height ratio.

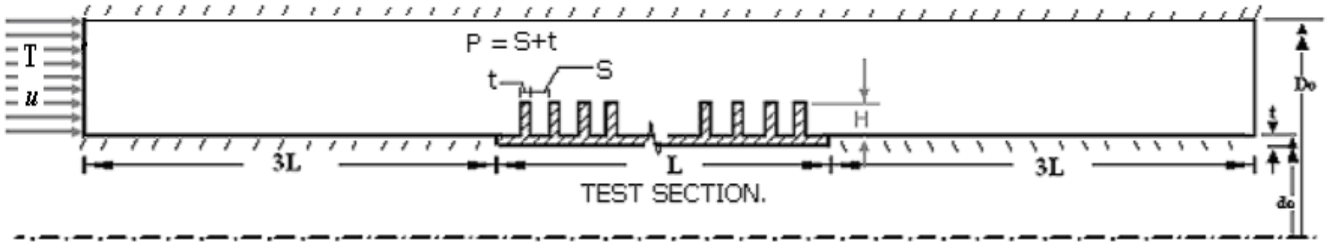

Figure 1 Problem Geometry.

The shaded region of Fig. 1 represents the solid zone of finned tube’s test section. The inner wall of the zone is subjected to constant temperature of 350 K while the side walls of the tube are approximated to be adiabatic. Outer walls of the finned test section are directly subjected to fluid stream to study the convection phenomenon, the boundary condition used is known as conjugate boundary condition or coupled boundary condition in FLUENT [6] terminology. The remaining horizontal walls are adiabatic and all walls that are in contact with fluid stream are subjected to no-slip hydrodynamic boundary conditions. The fluid considered is water at 300K with constant properties. The flow is considered to be incompressible, steady and laminar while the effects of body forces, buoyant forces and viscous dissipation are neglected. The governing equations were discretized using QUICK scheme to create a system of algebraic equations which were then solved using Tri Diagonal Matrix Algorithm. SIMPLE algorithm is used for coupling of pressure and velocity.

3. RESULTS AND DISCUSSION

The axial velocity field for annular region is shown in Fig. 2. Fins act as obstruction and separate the flow from fin tip and cause recirculation. The number of recirculating eddies and their shape depends on both Pitch-to-Height ratios and Reynolds number.

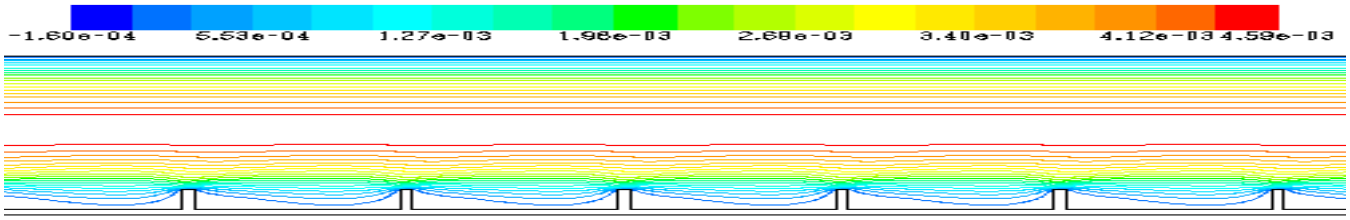

Figure 2. Axial Velocity Contours, P/H 4.4, Re 800

For smallest pitch-to-height ratio of 0.55, three recirculating eddies are observed in the inter-fin space. The first recirculation eddy is generated from the fin tip and recirculates in the direction of bulk fluid velocity. The second eddy recirculates in direction opposite to first while the last eddy that is nearest to the base and the smallest in size moves in the same direction as the first one. The eddy recirculation is shown in Fig. 3.

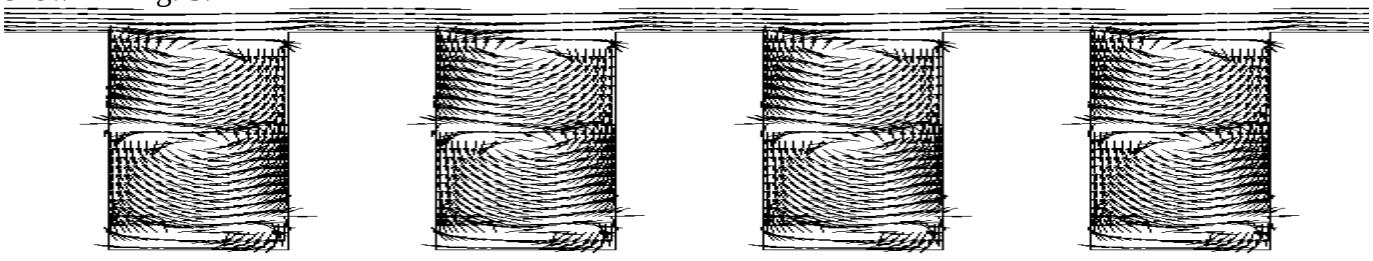

Figure 3. Flow Recirculation Vectors, P/H 0.55, Re 800

When the P/H ratio is increased to 1.1 and 2.2 the entire interfin space is occupied by a single recirculating eddy. The situation remains same for P/H ratio of 4.4 when Reynolds numbers are high. At a Reynolds number of 200, the flow is found to reattach behind the fin at a distance of 0.6 times the interfin space. The flow reattaches for all other P/H ratios at all values of Reynolds number studied. The reattachment length increases as Reynolds number increases. At low Reynolds numbers two distinct recirculating regions can be seen, one behind the first and the other in front of the second fin as shown in Fig. 4(a) but for higher Reynolds number values, as can be seen in Fig. 4(b) and Fig. 4(c) where the flow does not reattach, there is just one big recirculation region between the interfin space. In all cases of flow reattachment another small recirculating eddy is observed at the downstream end of the inter-fin space.

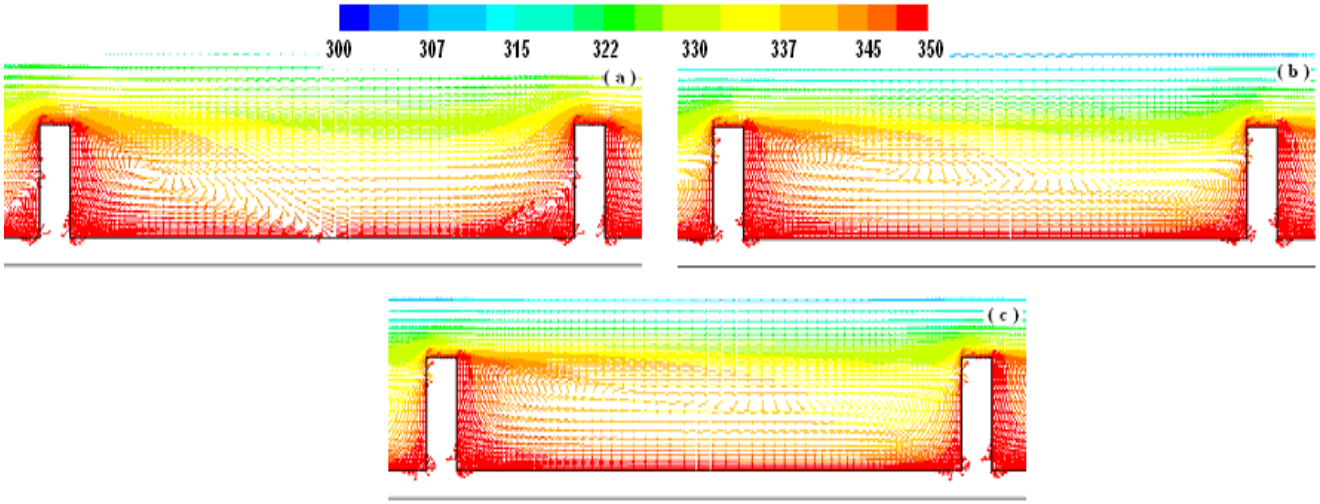

Figure 4 Flow Recirculation, P/H 8.8; (a) Re 200 (b) Re 800 (c) 1400. Colored by Temperature (K)

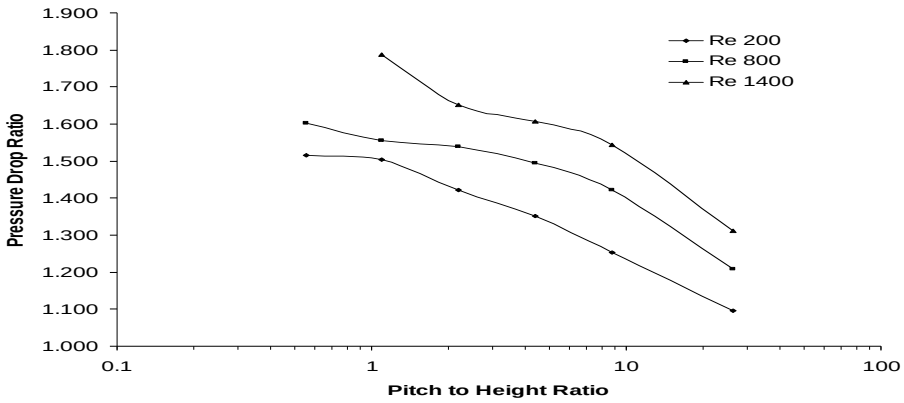

Figure 5 Pressure Drop Ratios

Fig 5 shows the pressure drop ratios of finned tube with respect to finless tube. As expected, for all the pitch to height ratios studied pressure drop increases when compared to finless tube and a maximum of about eighty percent increase in pressure drop value is observed for a pitch to height ratio of 1.1 at a Reynolds number of 1400. As a general trend, increase in Reynolds number increases the pressure drop while increase in pitch to height ratio decreases it.

Fig. 6 shows the temperature distribution in the test section for a P/H ratio of 4.4 and a Re value of 800. The test section as described earlier consisted of a solid finned region and an unfinned fluid region between two fins. It can be seen that the heat flux does not penetrate deep into the annulus and only a small portion is affected by temperature gradients. The temperature gradients are prominent only in the interfin spaces occupied by flowing fluid while the solid finned region attained approximately the same temperature as applied at the constant temperature boundary. In the fluid the isotherms near fin-tips are more closely spaced indicating that maximum heat flux leaves from this portion of the fin. Isotherms with larger spacing are observed towards the fin side walls that are not in direct contact with the incoming fluid stream, this is because the recirculating eddies have small velocities in the region thus transferring the heat by fluid conduction only. Isotherms near the upstream side of fins are largely spaced around fin

base and come closer near the tip, therefore, heat transfer increases gradually from fin-base towards fin-tip.

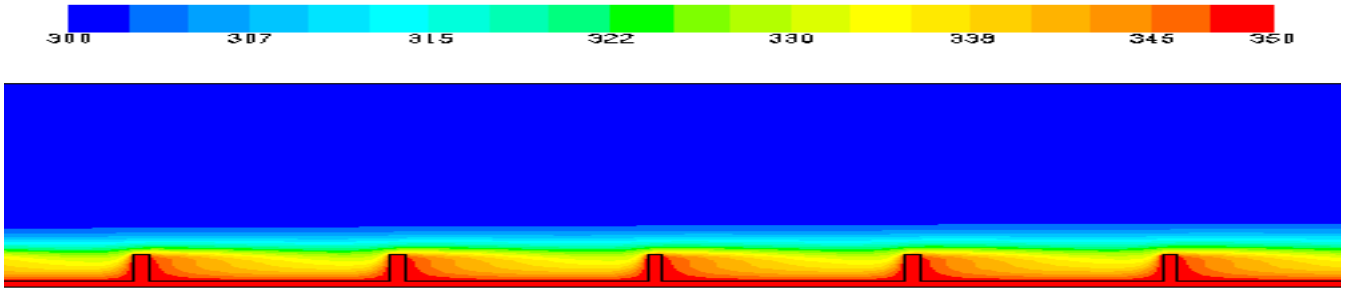

Figure 6 Temperature Contours, Re 800, P/H 4.4 (K)

Fig 7 shows that fins with small P/H ratios are more effective than fins with large P/H ratios and as this ratio is increased the effectiveness of fins decrease and fin heat flux values fall below that of the reference tube. Increasing the Reynolds number increases the effectiveness of fins and shifts the transition point, the point where effect of fin diminishes, towards higher P/H ratios. Decreasing the P/H ratio decreases the interfin space. Decreasing the fin spacing increases the heat transfer and maximum heat transfer is achieved at a P/H ratio of 0.55 which corresponds to minimum inter fin space considered in this study. These results contradict those published by Agrawal and Sengupta [5], who studied the problem of finned tube annulus numerically and claimed that closely spaced fins decreases the heat transfer.

This contradiction may be explained by looking at the Fig 8 which shows that when fin-spacing is small the major source of heat transfer are fin tips which may contribute to about fifty percent of total heat transfer. The contribution from base tube is almost negligible at these small P/H ratios while upstream and downstream faces of fin become secondary surfaces for heat transfer. In the heat transfer literature fin tip heat transfer is often neglected which would produce erroneous results if applied to the present case. Fig 8 also shows the fractions of total heat transfer from different parts of the fin i.e the tip, the upstream face, the downstream face and the base tube. It shows that for small P/H ratios of 0.55 and 1.1 maximum heat is transferred from fin tip and its contribution may be as high as about sixty percent of total heat transfer. Therefore, increasing fin thickness will result in higher total heat transfer rates from tip. Upstream face is the second most important contributor in total heat flux for P/H ratios less than 3. For a short range between P/H ratios of 2.2 and 3, the contribution from tip and upstream side are almost of the same order. For P/H ratios of 3 or higher the contribution from tube base wall supersedes all other fin surfaces followed by the upstream wall which remains second best contributor after base tube wall.

The present observations of increased heat transfer in closely spaced fins is also supported by the experimental work of Geiger & Mandal [4] who concluded in their study of annulus with circumferential fins that closely spaced fins transferred more heat than fins with larger spacing as a result of increased heat transfer area and better fluid mixing due to vortex formation.

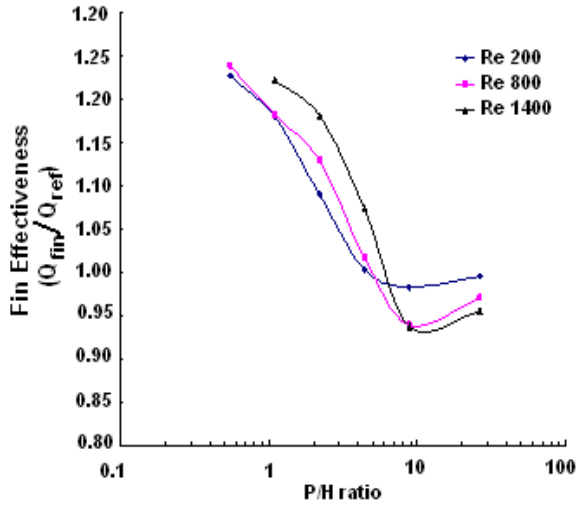

Figure 7 Fin Effectiveness vs Reynolds Number.

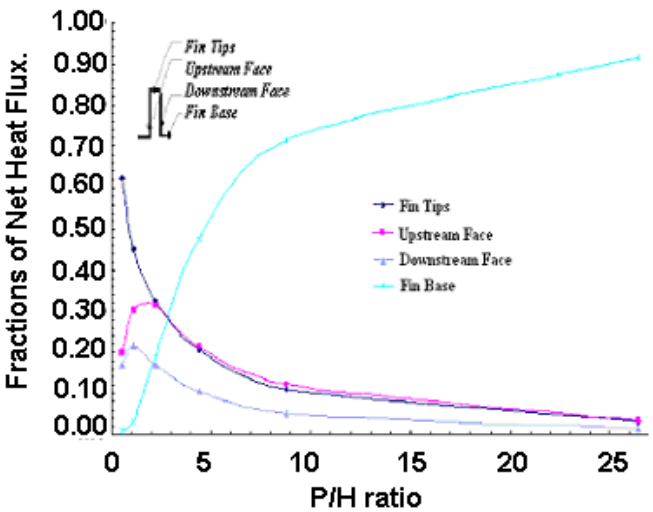

Figure 8 Fractions of Net Heat Fluxes

It is obvious from Fig 6 that the heat transfer in the inter fin space is periodic in nature. This repetition can also be observed by looking at the heat flux distribution at the wall where constant temperature boundary condition is applied. In Fig. 9 variation of dimensionless heat fluxes at constant temperature walls are superimposed on the geometry to show the peaks that are observed at the finned portion of the tube wall. Apart from the high peaks above the fins there is also variation of heat fluxes in the inter fin space. For a fixed P/H ratio, increase in Reynolds number increases heat flux from the fins and also the heat flux patterns change in the region where the fluid stream hit the fin face. This variation of heat flux is different for each P/H ratio.

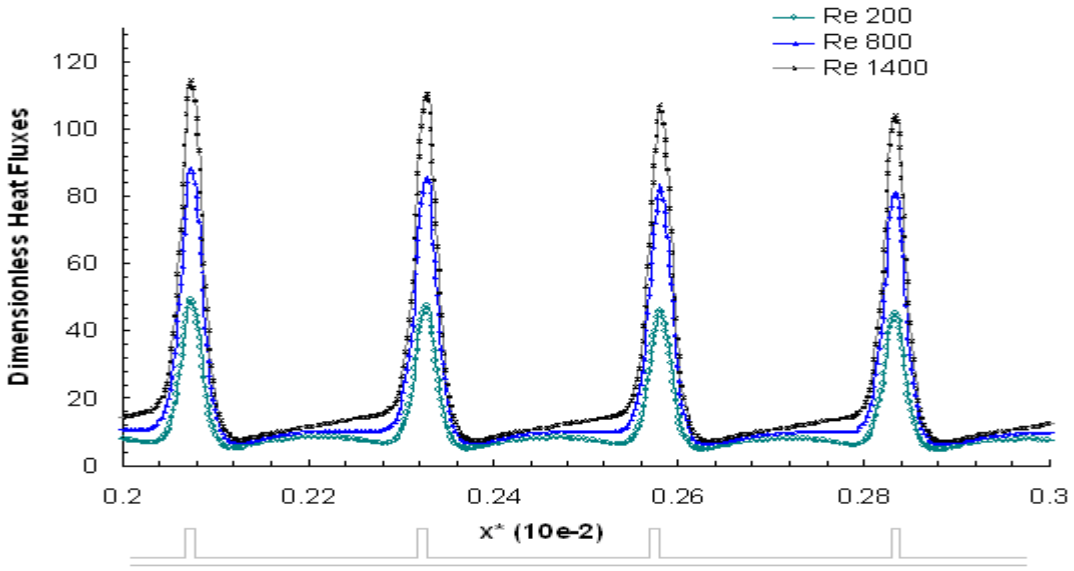

Figure 9 Heat Flux Variation at Constant Temperature Wall (P/H 4.4)

In Fig 10 a comparison is made between heat flux variation at constant temperature walls of reference tube and finned tubes for various P/H ratios. It may be noted that the geometry with a P/H ratio of 0.55 is the only geometry for which the local heat flux remained above the value of the reference tube. For other (higher) P/H ratios the local heat flux may go below the reference tube values in the un-finned portion of the tube wall as can be seen from the figure.

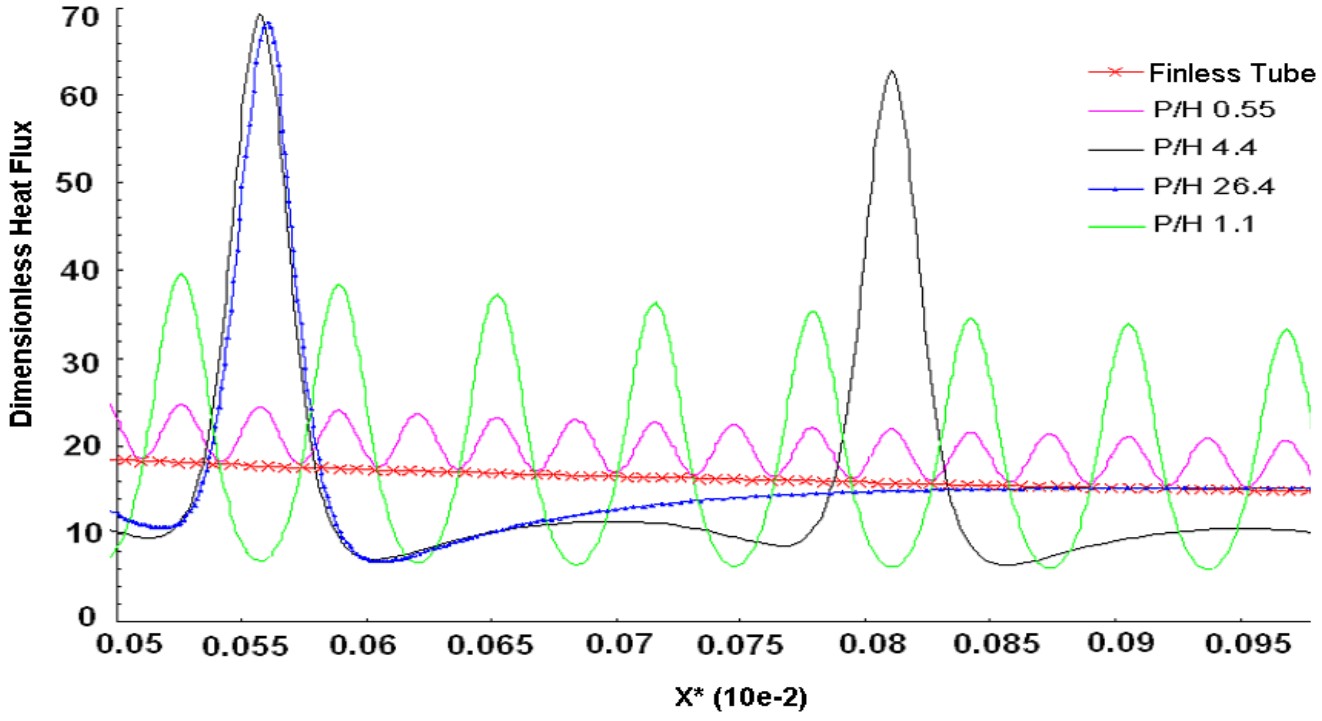

Figure 10 Comparison of Finless and Finned local Heat Fluxes Variation.

4. CONCLUSIONS

Addition of fins does not always guarantee heat transfer enhancement whereas increase in pressure drop is obvious for all cases. Decreasing the P/H ratio increases heat transfer. Very large P/H ratios can even result in heat transfer less than the finless tube.

Increasing the Reynolds number increases the heat transfer for P/H ratios more than one but for those P/H ratios less than one increasing Reynolds number decreases the effectiveness.

5. NOMENCLATURE

$\phi_{x,T}$ Dimensionless Heat Flux

$$\phi_{x,T} = \frac{q_x'' D_h}{k_f (T_{s,constant} - T_{m,0})}$$

q_x'' Local Heat Flux [W/m^2]

$$q_x'' = k_f \left(\frac{\partial T}{\partial n} \right)_{wall}$$

ε_f Fin Effectiveness

$$\varepsilon_f = \frac{Q_{fin}}{Q_{reff}}$$

x^* Dimensionless Axial Coordinates

$$x^* = \frac{x / D_h}{\mathrm{Re}\,\mathrm{Pr}}$$

D_h Hydraulic Diameter,[D_o- d_o] [m]

D_o Inner Diameter of Outer Tube of Finned Tube Heat Exchanger [m]

d_o Outer Diameter of Inner Tube [m]

Q_{ref} Heat Transfer from Reference Tube, [W]

Q_{fin} Heat Transfer from Finned Tube [W]

Re Reynolds Number for Finned Tube Annulus

$$\mathrm{Re} = \frac{\rho . u . D_h}{\mu}$$

k_f Thermal Conductivity of fluid, [W.m^{-2}]

ρ Density of Fluid, [Kg.m^{-3}]

x Axial Coordinates [m]

μ Dynamic Viscosity [Kgm^{-1}.s^{-1}]

u Mean Velocity [m.s^{-1}]

6. ACKNOWLEDGEMENTS

The support provided by NED University of Engineering & Technology and Higher Education Commission of Pakistan for this work is highly appreciated.

7. REFERENCES

[1] Kundsen, J.G and Katz, D. L, Heat Transfer and Pressure Drop in Annuli., *Chem. Engng. Progress*, 56(1950), pp. 490-500.

[2] Obremeier , E and Schaiber, A. Experimental Investigation of Heat Transfer From Transverse Finned Tubes With Longitudinal Flow, Proceedings, Sixth International Heat Transfer Conference, Hemisphere, Washington, D.C, 1978, pp. 607-611.

[3] Obremeier, E. and Henne, R.A, Performance Analysis of Augmented Heat Transfer Surfaces, Theoretical and Experimental Results for Tubes with Circumferential Fins in Longitudinal Flow, Proceedings, First International Conference on Aerospace Heat Exchanger Technology, Palo Alto, C.A, USA, February 1993, pp. 329-345.

[4] Geiger, G.E and Mandal, S.K, Heat Transfer and Friction Factor of High Prantdl Number Laminar Flow through an Annulus with Circumferential Fins, Proceedings, Sixth International Heat Transfer Conference, Hemisphere, Washington D.C, 1978, pp. 613-617

[5] Agrawal , A.K, and Sengupta, S, Laminar flow and Heat Transfer in Finned Tube Annulus, *Int. J. Heat and Fluid Flow*,11 (1990), 3, pp. 54-59.

[6] Fluent V 6.1, User Manual, Fluent Inc.

Proceedings of the 4th BSME-ASME International Conference on Thermal Engineering
27-29 December, 2008, Dhaka, Bangladesh

FORCES ON AND FLOW AROUND TWIN CYLINDRICAL STRUCTURES

Md. Mahbub Alam[1] and Tasnuva Tabashhum Choudhury[2]
Department of Mechanical Engineering
[1]The Hong Kong Polytechnic University, Hung Hom, Kowloon, Hong Kong
[2]Rajshahi University of Engineering and Technology, Rajshahi, Bangladesh
Emails: mmalam@polyu.edu.hk

ABSTRACT

This paper presents the results of an experimental investigation of Strouhal number (St) and time-mean and fluctuating forces on two identical circular cylinders at stagger angle $\alpha = 0^{\circ} \sim 180^{\circ}$ and gap spacing ratio T/D = 0.1 ~ 5, where T is the gap width between the cylinders, and D is the diameter of a cylinder. While forces were measured using a load cell, St was from spectral analysis of fluctuating pressures measured on the side surfaces of the cylinders. Flow visualization test was also conducted to observe flow structures around the cylinders. Based on forces, St and flow structures, nineteen distinct flow categories in the range of α and T/D investigated are observed, including three kinds of tristable flow and five kinds of bistable flow. The two cylinders experience maximum drag when arranged in side-by-side ($\alpha = \pm 90^{\circ}$) with T/D = 2.2 ~ 2.6 and at $\alpha = \pm(45^{\circ} \sim 90^{\circ})$, T/D = 1.1~1.2. Lift becomes maximum (repulsive) at $\alpha = \pm 135^{\circ}$, T/D = 0.1 on the upstream cylinder and minimum (attractive) at $\alpha = \pm 10^{\circ}$, T/D = 0.8 ~ 1.1 on the downstream cylinder. Fluctuating forces on the downstream cylinder are extensively high in two island-like regions $\alpha = \pm(10^{\circ} \sim 30^{\circ})$, T/D = 2.5~5 where the inner shear layer of the downstream cylinder sheds vortices in synchronization with the convective inner vortices from the upstream cylinder, generating a coupled vortex. A detail mutual discussion on forces, St and flow structures is made in this paper.

Keywords: *Twin cylinders, Forces, Flow structures, Flow region.*

1. INTRODUCTION

Most structures on land and in the ocean are in multiple forms, e.g., chimney stacks, tube bundles in heat exchangers, overhead power-line bundles, bridge piers, stays, masts, chemical-reaction towers, offshore platforms and adjacent skyscrapers. The alternate shedding of vortices in the near wake leads to fluctuating forces on the structures and may cause structural vibrations, acoustic noise, or resonance, which in some cases can trigger failure. The study of aerodynamics of two closely separated structures is of both fundamental and practical significance. Fluid forces, Strouhal numbers (*St*) and flow structures are the major factors considered in the design of multiple slender structures subjected to cross flow. Two cylinders are considered as the basic model of multiple structures. Apparently, the flow around two cylinder is apparently more complicated than that around a single one,

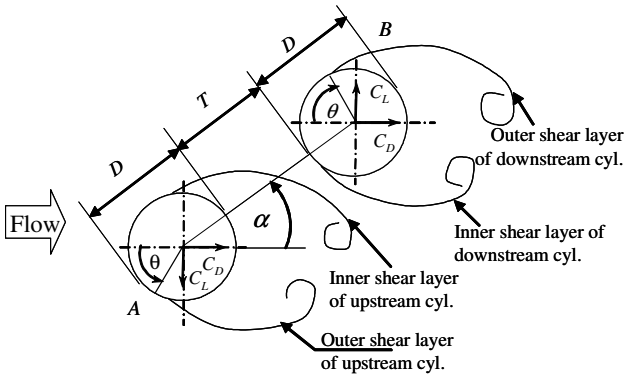

Fig. 1. Notation of staggered configuration.

depending on stagger angle (α) and *T/D* (see Fig. 1 for definitions of symbols).

Based on the interference effect between the two cylinders, Zdravkovich [1] divided the whole region of possible arrangements of two cylinders into four; (i) the proximity interference region, where the flow around one cylinder affects the other; (ii) wake interference region, the near-wake flow of the upstream cylinder is unaffected by the downstream one; however, the downstream one is significantly affected by the upstream cylinder; (iii) the proximity and wake interference region includes the combination of the proximity and wake interferences; (iv) the no interference region, where the wake of one cylinder does not affect the other. This classification is useful from the engineering design point of view, though providing little information on the flow structure around the cylinders.

Time-averaged drag and lift forces acting on two staggered cylinders have been examined in literatures (e.g., [2, 3]). However, data in the literatures are mostly concerned with the downstream cylinder. Though the fluctuating lift and drag forces acting on structures are a major cause of the fatigue failure of the structures and are used for predicting flow-induced responses, a review of literatures indicated that the information on fluctuating lift and drag forces on either cylinder is very limited, and many aspects of the flow structure around two staggered cylinders have yet to be explored. The objectives of this study were to (i) measure steady and fluctuating fluid forces and *St* (ii) elucidate the flow structure around and behind the cylinders, and (iii) classify force region on *T/D*-α plane. Measurements were conducted at α = 0° ~ 180°, *T/D* = 0.1 ~ 5.0. The linkage between force and flow structure and the interactions between the cylinders are discussed in details.

2. EXPERIMENTAL DETAILS

Experiments were conducted at the fluid mechanics laboratory of Kitami Institute of Technology, Japan. Measurements were done in a low-speed, closed-circuit wind tunnel with a test section of 1.20 m in height, 0.30 m in wide, and 2.2 m in length. The Reynolds number (*Re*) based on the diameter of a single cylinder was 5.52×10^4 and the turbulent intensity was 0.5%. Fluid forces were measured using two load cells installed inside a circular cylinder of diameter *D* =49 mm (see Alam et al. [4] for details of the load cell). *St* was estimated from spectral analysis of fluctuating pressure measured on side surfaces of the cylinders. Experiments were performed for α = 0°, 10°, 25°, 45°, 60°, 75°, 90°, 105°, 120°, 135°, 155°, 170°, and 180°, for the spacing ratio of *T/D* =0.1 ~ 5. Flow visualization was carried out in a water channel with a 250 mm × 350 mm working section and 1.5 m long. In the flow visualization test, two circular cylinders with identical diameter of 20 mm were used. *Re* in water channel experiment was 350.

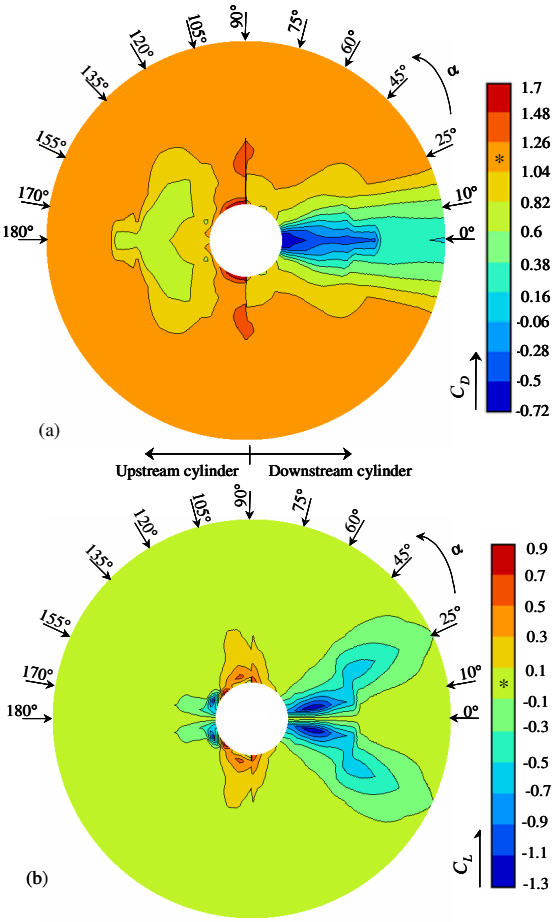

Fig. 2. Contour maps of (a) C_D and (b) C_L. Points marked by '*' denote values of coefficients of an isolated cylinder.

3. RESULTS AND DISCUSSION

3.1. Fluid forces and *St*

Time-averaged drag coefficient (C_D), time-averaged lift coefficient, (C_L), fluctuating drag coefficient (C_{Df}), fluctuating lift coefficient (C_{Lf}) and *St* are plotted in a *T/D*-α plane, and then the contour maps are drawn, as shown in Figs. 2-4. In the scale bars, the color or the range marked by black '*' indicates the

value of a single isolated cylinder. For the purpose of simplicity, the result can be described with reference to Fig. 1, in which the cylinder *A* is tentatively assumed to be fixed, and thus the two parameters *T/D* and α suffice to determine the arrangement of the two cylinders. It may be noted that the cylinder *B* is the downstream cylinder for $-90^\circ<\alpha<90^\circ$ and it becomes the upstream cylinder for $90<\alpha<-90^\circ$, i.e., the left and right sides of a contour map show the values of coefficient of the upstream and downstream cylinders, respectively. At the peripheries of the inner and outer circles, the values of *T/D* are 0 and *T/D*=5.0, respectively. Note that the values of C_D, C_{Df}, C_{Lf} and *St* of a single cylinder are 1.12, 0.14, 0.48 and 0.186, respectively. Repulsive and attractive C_L are considered as positive and negative, respectively (Fig. 1).

The contour maps show that fluid force coefficients of the downstream cylinder briskly change with change in *T/D* and α; however, the upstream cylinder retains its single cylinder values for *T/D*>3.0 for any value of α. This signifies that the interference effect of the upstream cylinder on the downstream cylinder is much strong but the opposite is rather weak. From Fig. 2(a), it is seen that the upstream cylinder experiences somewhat lower C_D at $\alpha = -120^\circ$~120°, *T/D*<3.0 roughly than a single isolated cylinder. The downstream cylinder experiences highly negative C_D at $\alpha = -10^\circ$~10°, *T/D*<3.0, with a maximum negative value of -0.72 when it is in contact with the upstream cylinder at $\alpha=0^\circ$. Maximum C_D acts on the two cylinders when they are arranged in side-by-side arrangement with *T/D*=1.2~2.0 in which an enhanced antiphase vortex shedding occurs from the cylinders. A significantly higher C_D acts on the upstream cylinder at $\pm90^\circ<\alpha<\pm120^\circ$, *T/D*<0.2. Highly negative C_L acts on the upstream cylinder at $\alpha=\pm140^\circ$~$\pm170^\circ$, *T/D*=0.25~0.45 and on the downstream cylinder at $\alpha=\pm5^\circ$~$\pm15^\circ$, *T/D*=0.4~1.7 (Fig. 2b). Significantly higher magnitudes of C_{Lf} and C_{Df} act on the downstream cylinder at $\alpha = -35^\circ$~35°, *T/D*>2.5 (Fig. 3). C_{Lf} and C_{Df} on the upstream cylinder become extremely small for $\alpha = -120^\circ$~120°, *T/D*<3.0 roughly and on both cylinders in the vicinity of side-by-side arrangement at small *T/D*. In the first region, they become very small because formation of fully developed Karman vortex behind the upstream cylinder is retarded by the presence of the downstream cylinder [4]. In the second region, the gap flow between the cylinders acts as a base bleed, propelling the rolling positions of the outer shear layers downstream, causing

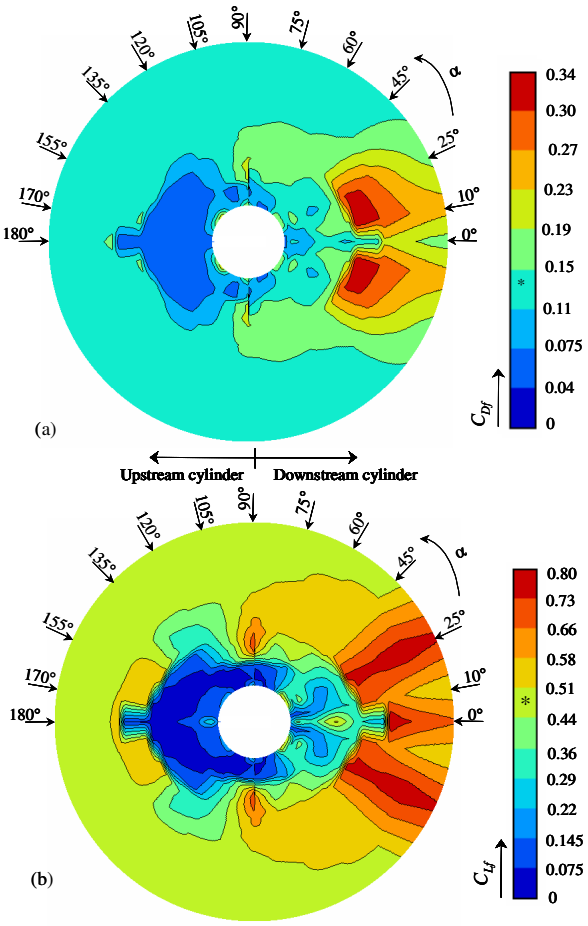

Fig. 3. Contour maps of (a) C_{Df} and (b) C_L. Points marked by '*' denote values of coefficients of an isolated cylinder.

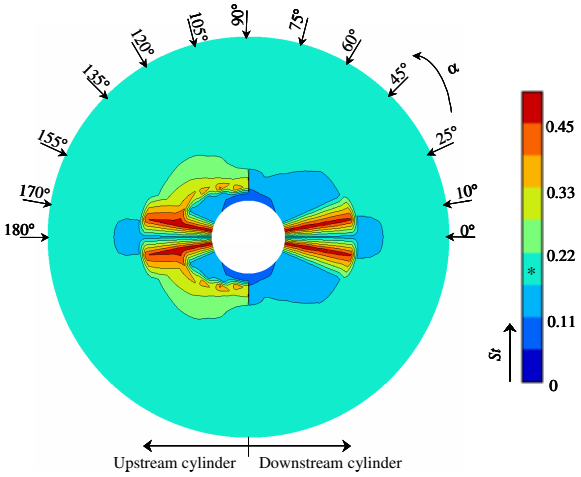

Fig. 4. Contour maps of *St*. Point marked by '*' denotes *St* value of a isolated cylinder.

small C_{Lf} and C_{Df}.

A scrupulous observation on *St* map (Fig. 4) unveils that *St* has a strong relationship with C_D and/or C_L, but not strongly with C_{Lf} or C_{Df}: *St* is inversely related with C_D and/or C_L. Where C_D or C_L is large in magnitude, *St* is lower and vice versa.

3.2. Classification of force region and flow structures

On the basis of magnitude and trend of C_D, C_L, C_{Df}, C_{Lf}, and *St*, and of characteristics of flow patterns, the whole region can be divided into nineteen small regions as illustrated in Fig. 5.

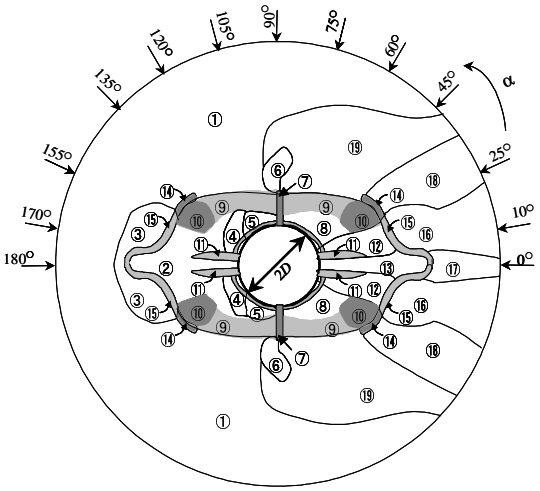

Fig. 5. Sketch specifying various regions. The regions marked by shadows are multistable flow regions

①: No interference region. C_D, C_L, C_{Df}, C_{Lf}, and *St* are almost the same as those of a single isolated cylinder.

②: Upstream-cylinder vortex suppressed region. Reduced C_D, zero C_L, very low C_{Df} and C_{Lf}; because the downstream cylinder impedes Karman vortex shedding from the upstream cylinder (Fig. 6a).

③: Upstream-cylinder excited flow region. Somewhat increased C_{Df} and C_{Lf}; due to appearance of fully developed and somewhat excited flow over and behind the upstream cylinder. The excitation of the flow is induced from the synchronized excited flow around the downstream cylinder (Fig. 6b).

④: Highly biased gap flow region. Attractive (negative) C_L on the upstream cylinder, low *St*. Highly biased gap flow along the periphery of the upstream cylinder causes attractive C_L (Fig. 6c). The two cylinders behave like a single body causing a low *St* of both cylinders. This region includes a bistable flow region marked by a shadow. Intermittent formation and burst of separation bubble on the inside surface of the upstream cylinder cause such a bistable flow being responsible for a large difference in C_L on the upstream cylinder.

⑤: Perfectly single-body region. Very high C_D, repulsive (positive) C_L and low *St*. The two cylinders act as a single bluff body, resulting in a high C_D and low *St* (Fig. 6d). Shift of stagnation point toward the gap side and a lower pressure gradient on the gap-side surface of the upstream cylinder originates the repulsive C_L. The lower gradient of pressure occurs due to retardation of flow on the gap-side surface by the front surface of the downstream cylinder. This region also incorporates a bistable flow region marked by a shadow. A turbulent reattachment and detachment of the inner shear layer of the upstream cylinder initiates the bistable flow.

⑥: Antiphase vortex shedding region. Very high C_D, repulsive C_L, high C_{Df} and C_{Lf}; an antiphase shedding fortifies the Karman vortices behind the two cylinders (Fig. 6e).

⑦: Tristable flip-flopping flow region. Three modes of the flow associated with narrow wake (high *St*), wide wake (low *St*) and symmetric wake (intermediate *St*) are generated and switch from one to another (Fig. 6f) [5].

⑧: Single-body-like region. Reduced C_D, C_{Df} and C_{Lf} and a single *St* in either wake (Fig. 6g).

⑨: Frequency-locked bistable flow region. Reduced C_D, C_{Df} and C_{Lf} and two and one *St* values for the upstream and downstream cylinders, respectively. It is a bistable flow region where shedding frequency of the upstream cylinder at times locks-in to that of the downstream cylinder (Fig. 6h).

⑩: Frequency-locked tristable flow region. Curtailed C_D, C_{Df} and C_{Lf} and two *St* values for the upstream and downstream cylinders. Three modes of flow with regard to vortex shedding frequencies appear intermittently. They are: (i) the flow with a high and low *St*

for the upstream and downstream cylinders, respectively, (ii) the flow with a high *St* for both cylinders: lock-in of the downstream wake to the upstream one, and (iii) the flow with a low *St* for both cylinders: lock-in of the upstream wake to the downstream one (see [6] for details).

⑪: Bubble-burst bistable flow region. The bistable flow results from intermittent formation and burst of a separation bubble formed on the inside surface of the downstream cylinder (Fig. 6i). The mode, in which separation bubble persists, results in a highly negative C_L on the downstream cylinder.

⑫: Separation-bubble flow region. Highly attractive C_L, resulting from a separation bubble (Fig. 6j).

⑬: Fully submerged flow region. Zero C_L and highly negative C_D. The downstream cylinder is fully submerged in the wake of the upstream cylinder (Fig. 6k).

⑭: Vortex-triggered tristable flow region. The convective vortices from the upstream cylinder trigger the vortex shedding from the downstream cylinder. The modes of flow are: (i) the flow with the higher and lower *St* for the upstream and downstream cylinders, respectively, (ii) the flow with the higher *St* for both cylinders, and (iii) the flow with synchronized *St* approximately equal to that of a single cylinder. This is actually a transition region in which fully developed flow behind the upstream cylinder starts to be formed [6].

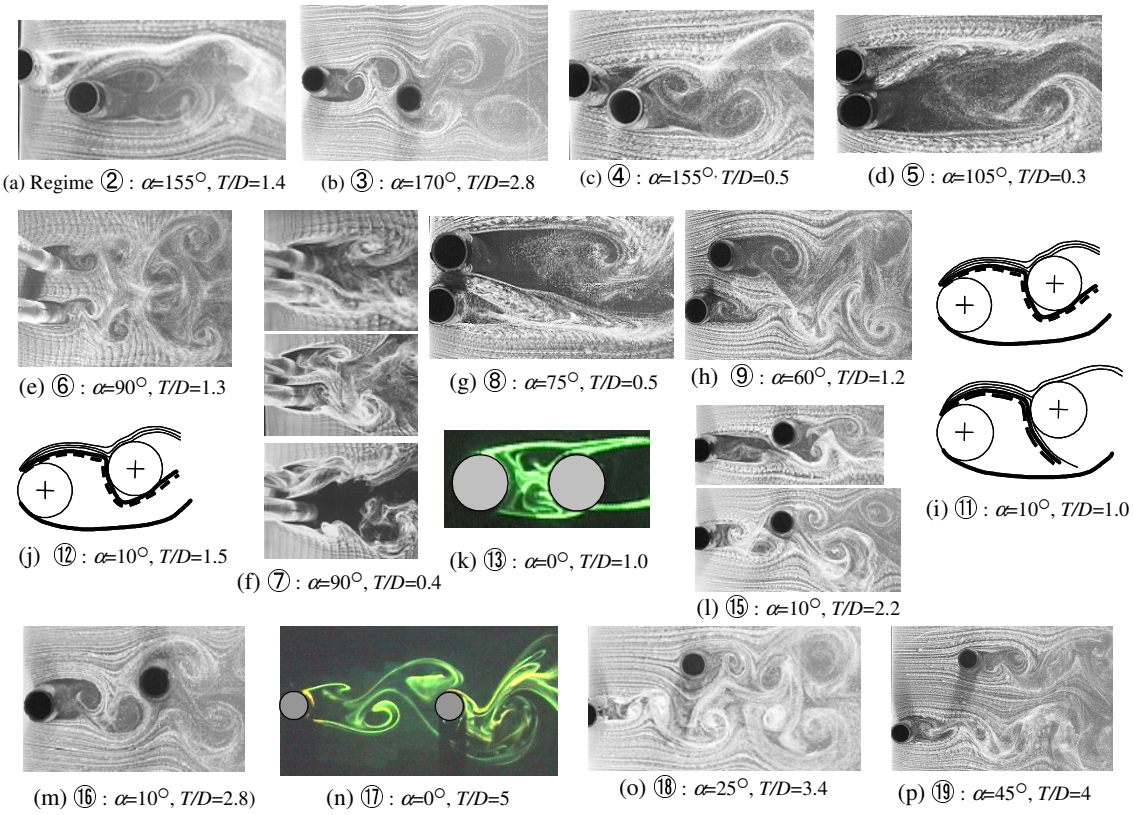

Fig. 6. Representative flow structures at different regions except at ①, ⑩ and ⑭.

⑮: Shear-layer-triggered bistable flow region. Two flow patterns appear alternately. For $\alpha=0^\circ$, i.e., in tandem arrangement, shear layers separating from the upstream cylinder reattach steadily onto the downstream cylinder or strongly roll-up behind the upstream cylinder, and for $0^\circ<\alpha<25^\circ$, only the inner shear layer of the upstream cylinder reattaches onto the front surface of the downstream cylinder or strongly rolls-up before it (Fig. 6l).

⑯: Vortex-triggered synchronized shedding region: very high C_{Df}; in this region, the inner shear layer of the upstream cylinder rolls just before the front surface of the downstream cylinder (Fig. 6m), causing a higher fluctuation of pressure on the front surface, hence a

higher C_{Df} on the downstream cylinder.

⑰: Co-shedding flow region. Very high C_{Lf}, engendered by buffeting of upstream-cylinder vortices convective on the side-surface of the downstream cylinder (Fig. 6n) [7].

⑱: Synchronize coupled-vortex region. Extremely high C_{Lf} and attractive C_L. The inner shear layer of the downstream cylinder sheds vortices in synchronization with the convective inner vortices from the upstream cylinder, generating a coupled vortex, resulting in a higher fluctuating pressure on the inner side surface of the downstream cylinder, hence the cylinder experiences a higher C_{Lf} (Fig. 6o).

⑲: Small interference region: somewhat high C_{Df} and C_{Lf}; the downstream cylinder is outside the wake of the upstream cylinder, hence interference effect is trivial (Fig. 6p).

4. CONCLUSIONS

(i) In C_{Df} and C_{Lf} contour maps, there exist two island-like regions where the values of C_{Df} and C_{Lf} for the downstream cylinder are extensively high.

(ii) Maximum C_D acts on the cylinders in the region of $\alpha = \pm 90^\circ$, T/D = 2.2 ~ 2.6 where vortex shedding from the cylinders occurs in antiphase mode and in the region of $\alpha = \pm$ (45°~90°), T/D=1.1~1.2 where the pair of the cylinders behave as a single body with regard to vortex shedding frequency.

(iii) C_L becomes maximum repulsive at $\alpha = \pm 135^\circ$, T/D = 0.1 on the upstream cylinder and becomes maximum attractive at $\alpha = \pm 10^\circ$, T/D = 0.8 ~ 1.1 on the downstream cylinder.

(iv) Three kinds of tristable flow and five kinds of bistable flow have been observed, appearing at different regions, having different characteristics. The 1st kind of tristable flow happens at region ⑦, side-by-side arrangement, and the 2nd and 3rd kinds of tristable flow at regions ⑩ and ⑭, respectively. The 1st kind of the bistable flow which appears for $\alpha = 0^\circ$, T/D=3.0, region ⑮, is due to existence of symmetric reattachment and detachment of the shear layers. The 2nd kind of bistable flow is due to intermittent reattachment and detachment of only the inner shear layer of the upstream cylinder, $\alpha < 20^\circ$, region ⑮. The third kind of bistable flow results from formation and burst of a separation bubble appearing on the inside surface of the downstream cylinder, region ⑪. The fourth kind of bistable flow is due to formation and burst of a separation bubble on the inside surface of the upstream cylinder or due to turbulent reattachment and detachment of the inner shear layer on the rear surface of the upstream cylinder, region ⑧. The fifth kind of bistable flow is associated with intermittent lock-in and release of the upstream cylinder frequency with that of the downstream cylinder, region ⑨.

RFERENCES

[1] Zdravkovich, M.M., The Effects of Interference between Circular Cylinders in Cross Flow, *Journal of Fluids and Structures* 1 (1987), pp. 239-261.

[2] Zdravkovich, M.M., Pridden, D.L., Interference between Two Circular Cylinders; Series of Unexpected Discontinuities, *Journal of Industrial Aerodynamics* 2 (1977), pp. 255-270.

[3] Price, S.J., Paidoussis, M.P., The Aerodynamic Forces acting on Groups of Two and Three Circular Cylinders when Subject to a Cross-Flow, *Journal of Wind Engineering and Industrial Aerodynamics* 17 (1984), pp. 329-347.

[4] Alam, M.M., Sakamoto, H., Zhou, Y., Determination of Flow Configurations and Fluid Forces acting on Two Staggered Cylinders of Equal Diameter in Cross-Flow, *Journal of Fluids and Structures* 21 (2005), pp. 363-394.

[5] Alam, M.M., Moriya, M., Sakamoto, H., Aerodynamic Characteristics of Two side-by-side Circular Cylinders and Application of Wavelet Analysis on the Switching Phenomenon, *Journal Fluids and Structures* 18 (2003), pp. 325-346.

[6] Alam, M.M., Sakamoto, H., Investigation of Strouhal Frequencies of Two Staggered Bluff Bodies and Detection of Multistable Flow by Wavelets, *Journal Fluids and Structures* 20 (2005), pp. 425-449.

[7] Alam, M.M., Moriya, M., Takai, K., Sakamoto, H., Fluctuating Fluid Forces acting on Two Circular Cylinders in a Tandem Arrangement at a Subcritical Reynolds Number, *Journal of Wind Engineering and Industrial Aerodynamics* 91 (2003), pp. 139-154.

Proceedings of the 4th BSME-ASME International Conference on Thermal Engineering
27-29 December, 20086, Dhaka, Bangladesh

FLOW CHARACTERISTICS IN THE TEST SECTION OF A WIND TUNNEL

A. Motin, M. A. T. Ali

Department of Mechanical Engineering
Bangladesh University of Engineering and Technology (BUET)
Dhaka-1000, Bangladesh
E-mail: motinme@gmail.com

ABSTRACT

The characteristics of wind velocity and the flow variation i.e. the non uniformity of flow in the test section of a wind tunnel is described in this paper. To conduct this investigation the velocity profiles on the bottom plane of the test section are measured at different speeds by using pitot-static tube which is interfaced with computer through pressure transducer. The experimental data are utilized to quantify the flow uniformity, velocity gradient along the stream wise direction of the test section and the magnitude of velocity variation at different speeds setting. This experiment is performed in the test section of 300x300 mm wind tunnel facility in the Department of Mechanical Engineering of BUET.

KEYWORDS: *Wind tunnel; Flow uniformity; Velocity gradient; Data acquisition.*

1. INTRODUCTION

In the field of experimental research in fluid mechanics the wind tunnel is an important tool to provide significant information of flow characteristics in different flow situations. But it has certain limitations due to the growth of boundary layer and pressure variation in the stream wise direction and these are absent in the free flow condition [3]. When air enters in the inlet section of the wind tunnel, the friction is developed in the wall of the wind tunnel. As a result a boundary layer is developed near the walls. Due to boundary layer development, the free stream pressure variation is created along the stream wise direction of the test section. When a body is tested in the wind tunnel, actual phenomenon of the flow properties around the body can not be attained due to the free stream pressure variation in the developing zone. Several researchers worked on the wind tunnel and they mostly tried to minimize the growth of boundary layer by various methods for controlling these [1], [2], and [6]. To ascertain the amount of uncertainty in the experimental result of this wind tunnel the extent of pressure variation in test section is investigated.

2. EXPERIMENTAL PROCEDURE AND EQUIPMENT

The experiment was carried out in the 300x300 mm open circuit wind tunnel facility in the department of mechanical engineering, BUET at different speed range. The flow in the wind tunnel is produced by two 482 mm axial flow Wood Aerofoil (UK) fans. The test section is 1.22 m long with a maximum air speed of 80 km/hr (22 m/s). The schematic diagram of the wind tunnel is shown in figure 1. The fans are placed at the tail end side of the

wind tunnel and flow is discharged through a silencer and flow regulating butterfly valve. Out of two fans, speed of one fan can be controlled by motor speed controller. Thus the flow is controlled both by controlling the butterfly valve and/or by controlling the fan motor speed. The fan with its discharge unit is separated from the entry unit by a damper to minimize the propagation of vibration generated in the fan, to the upstream side of the wind tunnel. In the upstream side of the damper there are air filter box, flow nozzle, flow nets, entry section, test section, delivery section and diffuser. To determine the flow characteristics in the test section of the wind tunnel, velocity profiles are determined at several points in the stream wise directions. The measurements are taken with a 3mm Pitot-static tube (United Sensor, USA) traversed by a programmable positioning device paired with the data acquisition system designed for this experiment.

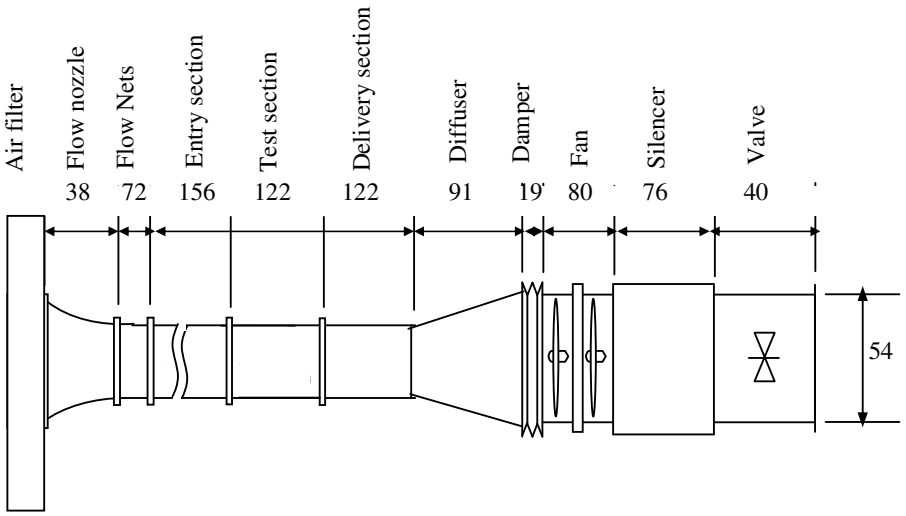

Fig.1: Schematic of wind tunnel (dimensions are in cm)

3. CALIBRATION

In this case, a micromanometer (FC014-Micromanometer, Furness Controls, U.K.) is used for the calibration of the transducer. For the purpose of calibration of the transducer the Pitot-static tube is connected both to the micromanometer and the pressure transducer in parallel. The output of the transducer is connected to the computer through the data acquisition system [4] and [7]. The Pitot-static tube is then placed in a uniform flow field of the calibration nozzle. Pressure signals for different flows are simultaneously taken both from the micromanometer and the computer. Velocity is calculated from the pressure signal recorded in the micromanometer by the equation (1) given below [5]:

$$U=\sqrt{2gh\left(\frac{\rho}{\rho_{air}}-1\right)}. \qquad (1)$$

The velocities thus obtained are plotted against the corresponding voltage signal record in the computer. The experimental points are then fitted with 2nd order polynomial in MS Excel which is shown in figure 2. The equation is found as

$$U = -4.1141x^2 + 18.929x + 4.3258 \quad (2)$$

To check the accuracy and repeatability of the measuring system the similar measurements in the calibration nozzle are taken several times and are found the variation within $\pm 3\%$. Considering the variation of the flow condition in the laboratory, this variation is taken to be acceptable.

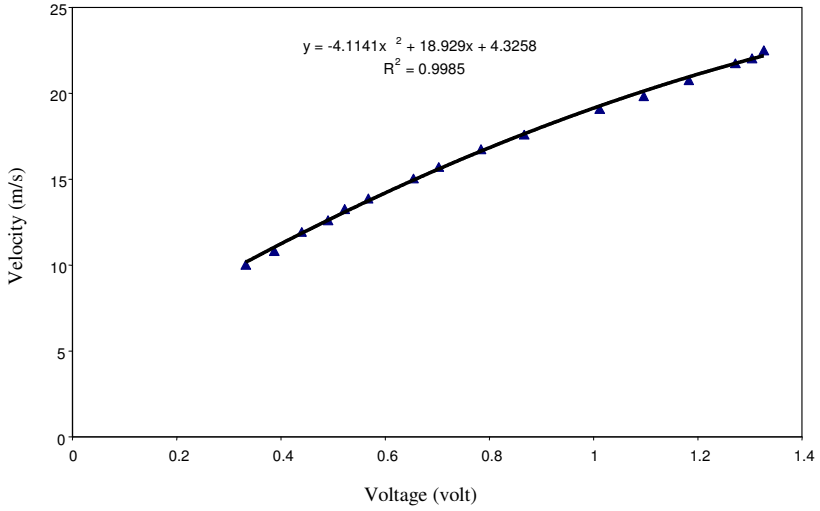

Fig. 2: Velocity versus voltage curve from different calibration data

4. RESULTS AND DISCUSSION

The free stream velocities at the centre of the open circuit wind tunnel test section are measured by the present device. The ratio of the r.m.s. value of the velocity variation to the free stream speed, $(\Delta U)_{rms}/U_\infty$ is determined at the centre of the tunnel. The results are shown in figure 3. It shows that, the variation of mean velocity decreases as the total sampling time increases. Figure 4 indicate that a minimum of about 8 second sampling time is required to achieve an acceptable data point that gives a relatively steady state average value ($(\Delta U)_{rms}/U_\infty \leq 0.02$). In figure 4, it is seen that, the variation of the average value of the mean velocity decreases with the increase of the number of samples, and this variation comes within the acceptable range ($(\Delta U)_{rms}/U_\infty < 0.75$) beyond the number of samples fifteen.

Figure 5 shows the velocity profile on the bottom plane at the entry of the test section of wind tunnel. It is seen from the figure 5 that a boundary layer is formed (δ=4 cm) at the entry of the test section due to flow developing in the entry section of the wind tunnel. The variation of U_∞ for different velocities from its mean value is shown in fig. 6. The mean velocity presented here is an average taken over 10 records, each taken one second apart. Each record consists of 15 samples taken 50 ms apart. Figure 6 shows the standard deviation **σ,** from the mean velocity over the 10 records. It is expressed as a percentage of the corresponding mean velocity. It shows that the wind tunnel speeds lies between 8 and 21.5 m/s is of in the useful range, where $\sigma < 1.6\%$.

The free stream velocity is not constant throughout the length of the test section, but increases slowly in the downstream direction. This is because the development of boundary layer along the walls of the test section. The boundary layer growth effectively reduces the cross-sectional area for the flow. This reduction in area causes the free stream flow to accelerate in the downstream direction. This indicates that the test section in the wind tunnel is in the developing zone of the flow. The result is shown in figure 7 along with velocities estimated from the static pressure measured along the wind tunnel. The measurements covered approximately 15 streams wise locations 10 mm apart. The standard deviation of local free stream velocity from the mean is typically about 1% over the test section, as illustrated in figure 8 (σ% represents the standard deviation of velocities in a cross section.).

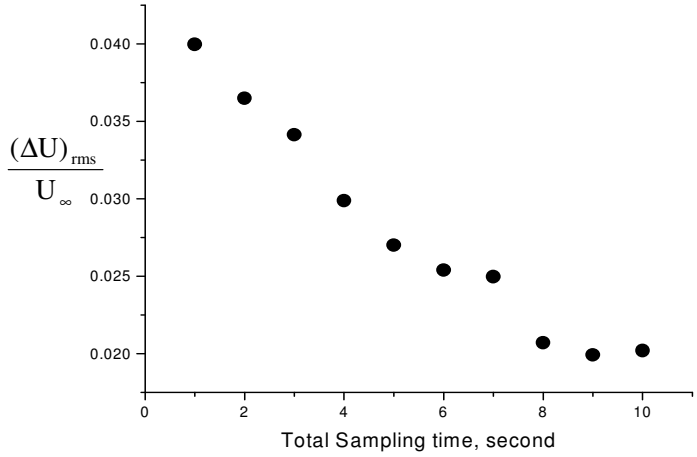

Fig. 3: Effect of sampling time on average data

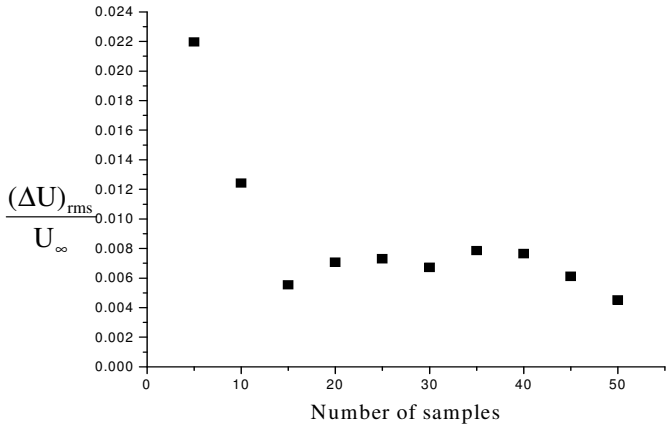

Fig. 4: Effect of number of samples taken on average data

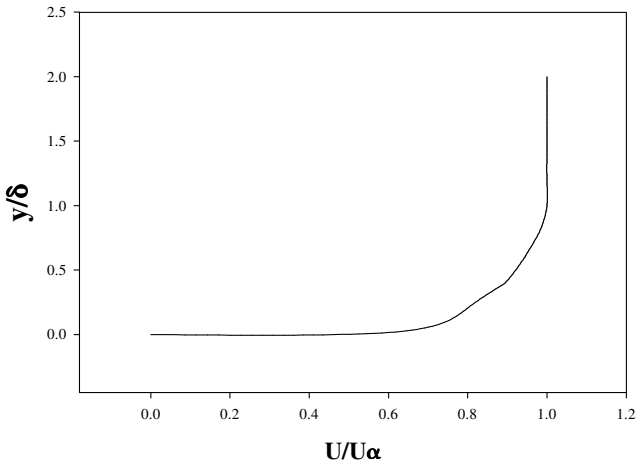

Fig. 5: Velocity profile on the bottom plane at the entry of the test section

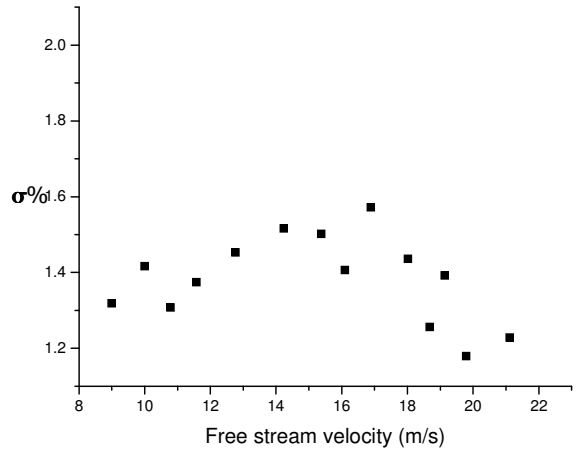

Fig. 6: Velocity variation level at different speed setting

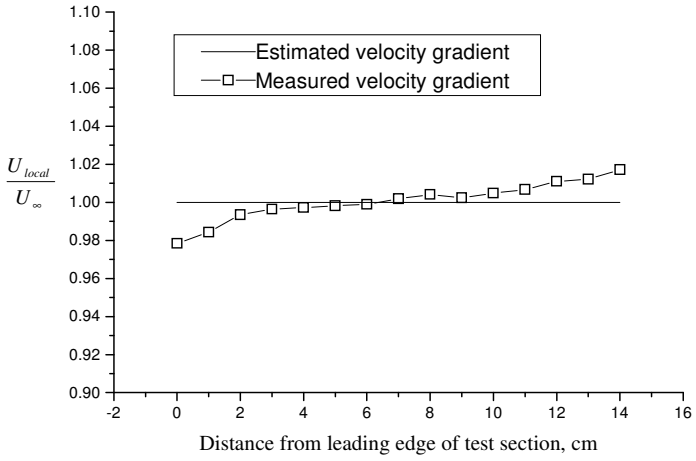

Fig. 7: Velocity gradient along tunnel centre line

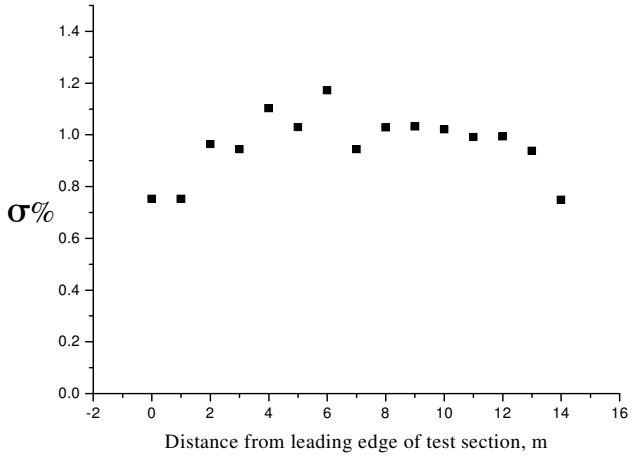

Figure 8: Variation in flow uniformity along tunnel centre line

5. CONCLUSION

It can be concluded that in the test section of the wind tunnel the free stream velocity along the stream wise direction is not constant. Free stream flow is accelerated in the downstream direction. The reduction of flow area due to boundary layer formation is observed in the downstream direction. Although some limitations are present in the test section, wind tunnel can provide significant information of flow characteristics.

6. REFERENCES

[1] M. Zabat, S. Frascaroli, F. Browand, Drag Measurements on a Platoon of Vehicles California PATH Research Paper, UCB-ITS-PRR-93-27

[2] G. L. Larose, B. Tanguay,"The New Boundary Layer Control System for NRC's 9m x 9m Wind Tunnel"National Research CouncilOttawa, ON Canada, AIAA-2001-0455

[3] H. Schlichting, K. Gersten, "Boundary Layer Theory", Springer, New York, 8th Revised and Enlarged Edition, Reprint-2003.

[4] J. P. Holman, 'Experimental Methods for Engineers', McGraw-Hill Inc., 6th Edition, 580

[5] V. L. Streeter, E.B. Wylie, 'Fluid Mechanics', McGraw-Hill, 1st SI Metric Edition, 337-340 (1983).

[6] T. E. Ferrell "Development of a New Boundary Layer Control Technique for Automotive Wind Tunnel Testing", Masters thesis, Submitted to the college of Engineering, Wichita State University, 2003

[7] M.S. Rahman, S.M.R. Hasan, M.A.I. Sarker, 'Pressure Monitoring by Computer Interface', Student project presentation, Bangladesh Society of Mechanical Engineers (BSME), 36-40 (2003).

Proceedings of the 4th BSME-ASME International Conference on Thermal Engineering
27-29 December, 2008, Dhaka, Bangladesh

ANALYSIS OF POTENTIAL FLOW AROUND 3-DIMENSIONAL HYDROFOILS

Md. Shahjada Tarafder, Goutam Kumar Saha & Sayeed Tanvir Mehedi
Department of Naval Architecture and Marine Engineering
Bangladesh University of Engineering and Technology
Dhaka-1000, Bangladesh
Email: shahjada68@yahoo.com, goutamkumar@name.buet.ac.bd

ABSTRACT

The paper deals with the computation of potential flow around the three-dimensional hydrofoil without the effect of free surface by the combined source and dipole panel method based on Dirichlet boundary condition. In order to solve the problem the Laplace equation is transformed into an integral equation in terms of a distribution of singular solutions (such as, sources and doublets) on the boundaries. After satisfying the boundary conditions the integral equation can be written into a matrix form and this matrix is solved by Gaussian Elimination procedure. The Kutta condition is applied at the trailing edge of the lifting body to generate required circulation which is constant across the wake surface. The verification of the numerical modeling is made using the NACA 0012 hydrofoil and the validity of the computer scheme is checked by comparing the numerical result with the analytical one of van de Vooren hydrofoil.

Key words: Potential Flow, Hydrofoil, Kutta condition, Van De Vooren hydrofoil

1. INTRODUCTION

The practical importance of hydrodynamic analysis of hydrofoils moving under a free surface is very well-known. Thin-foil approximation and the Neumann boundary condition were generally used. Giesing and Smith (1967) distributed the Kelvin wave source on the hydrofoil surface, which satisfies the linearized free surface condition, and they obtained an integral equation for the source strength by applying the kinematic Neumann body boundary condition. Yeung and Bouger (1979) used a hybrid integral equation method based on Green's theorem. They satisfied the linearized free surface condition and the exact body boundary condition. Wu and Eatock Taylor (1995) compared the finite element method with the boundary element method for the nonlinear time stepping solution of 2-D hydrofoils. Bal (1999) described a potential-based panel method for the hydrodynamic analysis of 2-D hydrofoils moving under a free surface with constant speed without consideration of the cavitation phenomenon. Bal (2005) addressed steady cavitating flows around swept and V-type hydrofoils under a free surface by using an iterative numerical method. The purpose of the paper to develop the numerical scheme for the analysis of the potential flow around the 3-D hydrofoil without the effect of free surface by combined source and doublet panel method based on the Dirichlet boundary condition. The verification of the numerical modeling is made using the NACA 0012 hydrofoil and the validity of the computer scheme is checked by comparing the numerical result with the analytical one of van de Vooren hydrofoil.

2. MATHEMATICAL MODELING OF THE POTENTIAL FLOW PROBLEM

Consider a hydrofoil fixed in a stream of uniform flow with a velocity Q_∞ as shown in Fig. 1. The depth of water from the mean line of the hydrofoil is h. A Cartesian co-ordinate system is

placed on the free surface and the components of the free stream velocity Q_∞ in the x-y-z frame of reference are U_∞, V_∞ and W_∞ respectively. The angle of attack α is defined as the angle between the free stream velocity and the x - axis

$$\alpha = \tan^{-1}\frac{W_\infty}{U_\infty}$$

It is assumed that the fluid surrounding the hydrofoil and the wake is inviscid, incompressible and the flow irrotational. The perturbation velocity potential ϕ is defined by $\Phi = \phi + \Phi_\infty$

where, $\Phi_\infty = U_\infty x + V_\infty y + W_\infty z$

Now the velocity field due to the hydrofoil can be obtained by solving the Laplace equation

$$\nabla^2\Phi = 0 \tag{1}$$

with the following boundary conditions:

(a) The velocity component normal to the solid boundaries of the hydrofoil must be zero and in a body-fixed frame of reference:

$$\nabla\Phi \cdot n = 0 \tag{2}$$

where n is an outward normal to the body surface.

(b) The disturbance induced by the hydrofoil will decay far from the body

$$\lim_{r\to\infty}\nabla\Phi = Q_\infty \tag{3}$$

which is automatically fulfilled by the singular solutions such as for the source, doublet or the vortex elements.

(c) A proper solution for the doublet distribution will have to fulfil the Kutta condition at the trailing edge of the lifting body such that the potential jump across the wake surface S_w is the same as the circulation and is constant in the streamwise direction on S_w.

$$\left[\Delta\Phi\right]_{on\,S_w} = \Phi - \Phi_i = \Gamma = \text{Constant}$$
$$= \Delta\Phi_{T.E.} \tag{4}$$

2.1 The General Solution Based on Green's Identity

Applying Green's Second identity the Laplace equation can be transformed into an integral equation as:

$$\Phi(P) = -\frac{1}{2\pi}\int_{S_B}\left[\ln r\,\nabla(\Phi-\Phi_i) - (\Phi-\Phi_i)\nabla\ln r\right]\cdot n\,dS + \frac{1}{2\pi}\int_{S_W}\Phi\, n\cdot\nabla\ln r\,dS + \Phi_\infty(p) \tag{5}$$

If the difference between the external and internal potentials or the difference between the normal derivative of the external and internal potentials is defined by

$$-\mu = \Phi - \Phi_i \tag{6}$$

$$-\sigma = \frac{\partial\Phi}{\partial n} - \frac{\partial\Phi_i}{\partial n} \tag{7}$$

the integral Eq. (5) can be written as

$$\Phi(P) = -\frac{1}{4\pi}\int_{S_B}\left[\sigma\frac{1}{r} - \mu\frac{\partial}{\partial n}\frac{1}{r}\right]dS + \frac{1}{4\pi}\int_{S_W}\left[\mu\frac{\partial}{\partial n}\frac{1}{r}\right]dS + \Phi_\infty(P) \tag{8}$$

The elements μ and σ in Eq. (6) and (7) are called doublet and source respectively and the minus sign is a result of the normal vector n pointing into S_B.

2.2 Panel Method Based on Dirichlet Boundary Condition

In Dirichlet problem, perturbation potential ϕ has to be specified everywhere on S_B and the zero flow normal to the surface $\nabla(\phi + \Phi_\infty) \cdot n = 0$ is to be specified in terms of the velocity potential as follows:

$$\Phi_i = (\phi + \Phi_\infty)_i = \text{const.} \tag{9}$$

By distributing the singularity elements on the surface and placing the point P(x, y) inside the surface S_B, the inner potential Φ_i in terms of the surface singularity distributions is obtained as

$$\Phi_i(x,y) = \frac{1}{2\pi}\int_{S_B}[\sigma\frac{1}{r} - \mu\frac{\partial}{\partial n}\frac{1}{r}]dS + \Phi_\infty \tag{10}$$

Again these integrals are singular when r→0, and near this point, their principal value must be evaluated. Now the boundary condition inside the body becomes

$$\Phi_i(x,y) = \frac{1}{2\pi}\int_{S_B}\left[\sigma\frac{1}{r} - \mu\frac{\partial}{\partial n}\frac{1}{r}\right]dS + \Phi_\infty = \text{const.} \tag{11}$$

Eq. (11) is the basis for methods utilizing the indirect boundary conditions. To construct a numerical solution the surface S is divided into N panels and the integration is performed for each panel such that

$$\frac{1}{2\pi}\sum_{j=1}^{N}\int_{\text{panel}}\sigma\frac{1}{r}\,dS - \sum_{j=1}^{N}\frac{1}{2\pi}\int_{\text{panel}}\mu\frac{\partial}{\partial n}(\frac{1}{r})dS + \Phi_\infty = \text{const.} \tag{12}$$

The integration is limited now to each individual panel element. In case of constant-strength singularity elements on each panel the influence of panel j at a point P is

$$-\frac{1}{2\pi}\int_{\text{panel}}\frac{\partial}{\partial n}(\frac{1}{r})dS\Big|_j \equiv C_j \tag{13}$$

In case of a doublet distribution and for a source distribution

$$\frac{1}{2\pi}\int_{\text{panel}}(\frac{1}{r})\,dS\Big|_j \equiv B_j \tag{14}$$

The influence integrals B_j and C_j will be calculated by using the formula as derived by Hess and Smith. Now the boundary condition inside the surface (at any point) becomes

$$\sum_{j=1}^{N}B_j\sigma_j + \sum_{j=1}^{N}C_j\mu_j + \Phi_\infty = \text{const.} \quad \text{for each collocation point} \tag{15}$$

Specifying this boundary condition on N collocation points allow N linear equations to be created. Since Eq. (15) is not unique, either the source or the doublet values must be specified. Here the inner potential Φ_i is selected to be equal to Φ_∞ and for this case source strength can be written as

$$\sigma_j = n \cdot Q_\infty \tag{16}$$

Since the value of the inner perturbation potential was set to Φ_∞, Eq. (15) is reduced to

$$\sum_{j=1}^{N}B_j\sigma_j + \sum_{j=1}^{N}C_j\mu_j = 0 \tag{17}$$

In addition to the Kutta condition, the above equation can be transformed into $N \times N$ matrix, which be solved by Gaussian Elimination Method.

2.3 Calculation of Pressures and Loads

Once the strength of the doublets μ_j is known, the potential outside the surface can be calculated. The internal perturbation potential Φ_i is constant and the external potential Φ_u is equal to the internal potential plus the local potential jump -μ across the solid surface.

$$\Phi_u = \Phi_i - \mu \tag{22}$$

The local external tangential velocity component above each collocation point can be calculated by differentiating the velocity potential along the tangential direction:

$$Q_t = \frac{\partial \Phi_u}{\partial l} \tag{23}$$

where l is a line along the surface. The simplest numerical interpretation of this formula is

$$Q_{tj} = \frac{\mu_j - \mu_{j+1}}{\Delta l_j} + Q_{t\infty} \tag{24}$$

where Δl_j is the distance between the two adjacent collocation points. This formulation is more accurate at the j-th panel second corner point and can be used to calculate the velocity at this point. The pressure coefficient can be computed by

$$C_{p_j} = 1 - \frac{Q_t^2}{Q_\infty^2} \tag{25}$$

3. RESULTS AND DISCUSSION

The combined source and doublet panel method has been applied first to NACA 0012 hydrofoil moving with a constant velocity in a direction perpendicular to its axis and at a fixed distance below the undisturbed free surface. The hydrofoil is of unit chord length and its span length is 10. In order to employ the three-dimensional panel method the hydrofoil is discretized by 18 chord wise panels and 5 span wise panels which are shown in Fig. 2. The pressure distributions on NACA 0012 hydrofoil at h/c = 0 are calculated for various angle of attack such as, $\alpha = 5^0$, 7.5^0 and 10^0 and the results are compared in Fig. 3

Discretizing the surface by 18×5, 26×5, and 36×5 panels respectively, the method has also been used in NACA 0012 hydrofoil at h/c = 0. The distributions of pressure are well predicted as shown in Fig. 4 and they are convergent to one another. The numerical solution presented here does not assume a symmetric solution. But it appears that the solution is symmetric about the x-axis and the number of unknowns can be reduced by M/2 by a minor modification in the process of influence co-efficient. The variations of drag and lift coefficients are given in Figs. 5 and 6 respectively.

In order to check the validity of the numerical results the method is applied to van de Vooren hydrofoil at various depths of water. The discretized view of the hydrofoil is shown in Fig. 7. A comparison of the present numerical result with the analytical one is drawn in Fig. 8 and the agreement in quite satisfactory. Fig. 9 shows the sensitivity of the pressure distribution on the discretization of the hydrofoil. The pressures on the hydrofoil at various depths of water such as $h/c = 0, 0.2$ and 0.4 respectively are plotted in Fig. 10 in which we can see that the effect of the depths of water is significant. The suction pressure on the upper surface of the foil is decreased at the leading edge whereas the positive pressure at the trailing edge is increased with the increase of the depth of water.

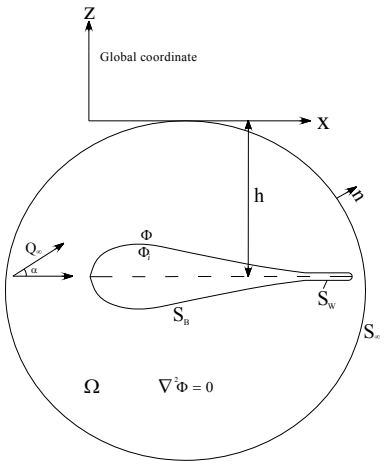

Fig. 1 Potential flows over a closed body

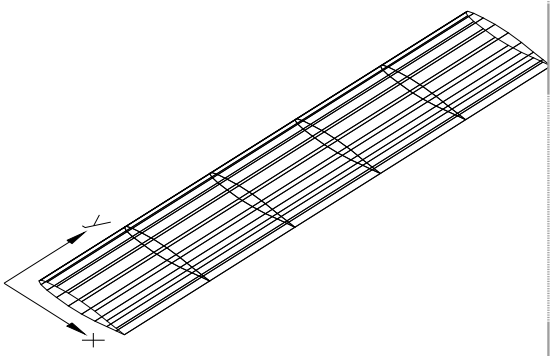

Fig. 2 Discretization of NACA-0012 hydrofoil by 18×5 panels

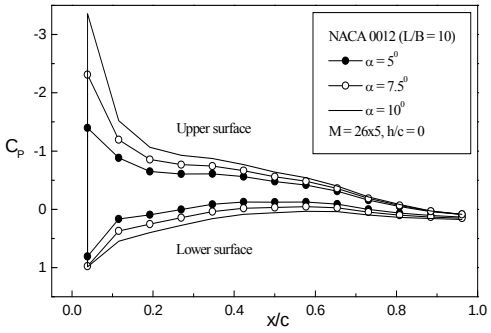

Fig. 3 Pressure distribution on NACA-0012 hydrofoil at y/c = 0

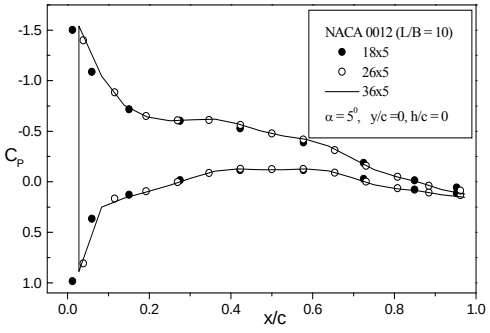

Fig. 4 Pressure distribution on NACA-0012 hydrofoil at y/c = 0.2

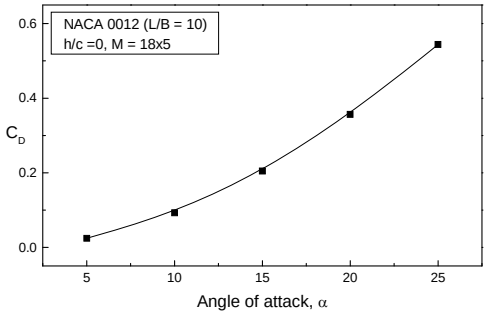

Fig. 5 Variation of drag coefficient with the angle of attack

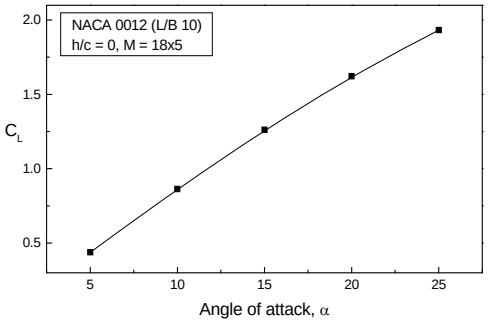

Fig. 6 Variation of lift coefficient with the angle of attack

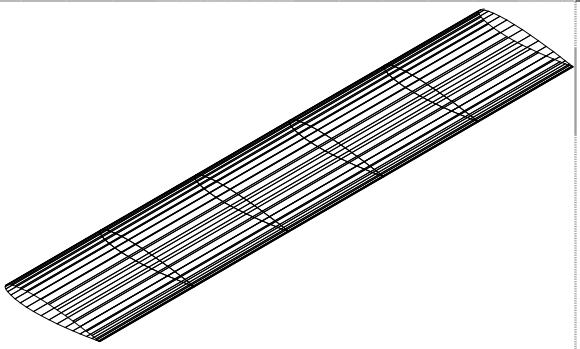

Fig. 7 Discretization of van de Vooren by 36×5 panels

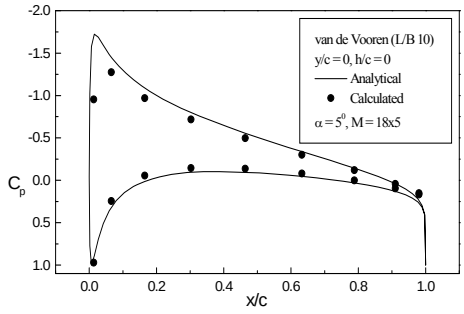

Fig. 8 Pressure distribution on van de Vooren hydrofoil

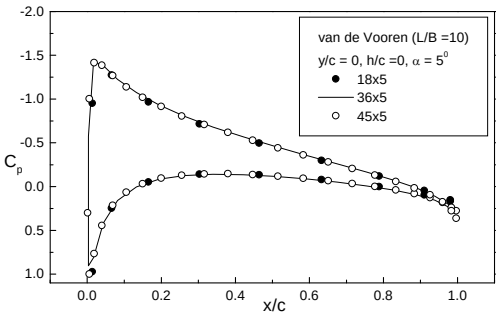

Fig. 9 Pressure distribution on van de Vooren hydrofoil

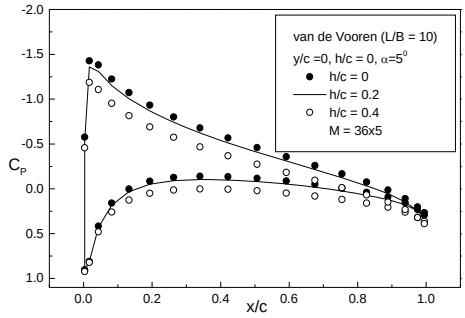

Fig. 10 Water depth effect on the pressure distribution of van de Vooren hydrofoil

4. CONCLUSIONS

This paper presents the combined source and doublet based boundary element methods for computing the potential flow around the hydrofoil moving with a uniform speed in an unbounded fluid. The following conclusions can be drawn from the present numerical study: (a) The present method could be a useful tool for analyzing the hydrofoil as well as ship like body and the agreement between the calculated and the analytical results is quite satisfactory. (b) The suction pressure on the upper surface of the foil is decreased at the leading edge whereas the positive pressure at the trailing edge is increased with the increase of the depth of water. (c) The calculated results depend to a certain extent on the discretization of the body. So similar panel arrangements is be used for checking the validity of the numerical results.

5. REFERENCES

[1] Abbott, I. H. & Von Doenhoff, A.E. (1959): Theory of Wing Sections, Dover Publications, New York, pp. 311-321.

[2] Bai, K.J. (1978): A localized finite-element method for two-dimensional steady potential flows with a free surface, *Journal of Ship Research*, Vol. 22, pp.216-230.

[3] Bal, S. (1999): A panel method for the potential flow around 2-D hydrofoil, *Transactions of Journal of Engineering and Environmental Science*, Vol. 23, pp.349-361.

[4] Bal, S. (2005): Lift and drag characteristics of cavitating swept and V-type hydrofoils, *International Journal of Maritime Engineering*, The Royal Institute of Naval Architects.
[5] Bristow, D. R. (1980): Development of panel methods for subsonic analysis and design, NASA CR 3234.
[6] Giesing, J.P. and Smith, A.M.O. (1967): Potential flow about two-dimensional hydrofoils, *Journal of Fluid Mechanics*, Vol. 28, pp.113-129.
[7] Hess, J. L., and Smith, A. M. O. (1962): Calculation of non-lifting potential flow about arbitrary three-dimensional bodies, Douglas-McDonnell Rep. No. E. S. 40622.
[8] Hess, J. L., and Smith, A. M. O. (1964): Calculation of non-lifting potential flow about arbitrary three- dimensional bodies, *Journal of Ship Research*, No.8, pp. 22-44.
[9] Hess, J. L., and Smith, A. M. O. (1967): Calculation of potential flow about arbitrary bodies, Progress in Aeronautical Sciences, Vol. 8, pp. 1-138.
[10] Wu, G.K. and Eatock Taylor, R. (1995): Time stepping solutions of the two dimensional nonlinear wave radiation problem, *International Journal of Ocean Engineering*, Vol.22, pp.785-798.
[11] Yeung, R.W. and Bouger, Y.C. (1979): A hybrid-integral equation method for steady two-dimensional ship waves, *International Journal of Numerical Methods in Engineering*, Vol.14, pp.317-336.